Vertically aligned α-MoO_3 Synthesis, Characterization and Applications

Dissertation submitted for the degree of
Doctor of Natural Sciences (Dr.rer.nat.)

by

Sohaila Zaghloul Noby

at the

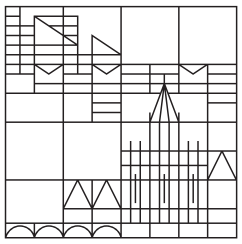

Universität Konstanz

Faculty of Mathematics and Natural Sciences
Department of Physics

Konstanz 2020

- The Date of the oral examination: 22.02.2021
- Dissertation has been reviewed and approved by:
  Prof. Paul Leiderer (Physics department, University of Konstanz)
  Prof. Lukas Schmidt-Mende (Physics department, University of Konstanz)
  Prof. Peter Nielaba (physics department, University of Konstanz)

Contents

List of Figures

List of Tables

Abstract

Advanced functionalized materials are highly desired for technological advancements spanning physics, chemistry, materials science and biology due to their unique electronic properties. One such example is molybdenum trioxide (MoO_3) nanostructures that offer high surface area in the form of sheet-like structures, well-oriented morphology, wide band gap, and tunable electronic properties. MoO_3 are widely used for different applications, for instance, in the field of energy storage and conversion, gas sensing, displays and memory devices. A key advantage these nanomaterials offer is their facile morphological and structural engineering, that is desired to tune the electronic properties of these nanomaterials to fit our needs.

The present study demonstrates a large scale growth of vertically aligned α-MoO_3 nanoblades on conducting and non-conducting substrates *via* a novel and reproducible procedure using a simple, low-cost hydrothermal technique. The synthesis method consists of two steps. In the first step, a thermally evaporated Cr/MoO_3 seed layer is formed on the substrates followed by the growth of dense, polycrystalline α-MoO_3 nanostructures in a highly acidic precursor solution in the second step. The influence of growth parameters, such as pH and concentration of the precursor solution, growth temperature and growth period on the growth mechanism and the morphology of the vertically aligned α-MoO_3 nanoblades has been thoroughly investigated.

As a transition metal oxide material, α-MoO_3 has various oxidation states, which can alter the electronic properties, for instance, electrical conductivity by several orders of magnitude. This can be achieved by manipulating intrinsic defects in the crystal e.g. oxygen vacancies, which has a direct impact on the oxidation states (hence the electrical conductivity). The primary objective of our study is to investigate the role of oxygen vacancies, which have been introduced into the crystal lattice *via* a thermal treatment under different oxidizing and reducing atmospheres (e.g. O_2, H_2, vacuum, and N_2). The positions of the oxygen vacancies and restitution of the oxygen ions in the MoO_3 crystal have been experimentally demonstrated primarily *via* electron paramagnetic resonance, high-resolution electron microscopy and other techniques. These phenomena have been understood and discussed *via* color center formation and polaron migrations models. The experimental characterizations show a consistent trend with previously reported theoretical studies and calculations.

The oxygen vacancies in the MoO_3 crystal structure are found to have no influence on the optical band gap. They, however, significantly impact the electrical conductivity by altering the MoO_3 properties from semi-insulating to conducting. Vertically aligned α-MoO_3 nanoblades showed n-type behavior for the reduced nanostructure and degenerated n-type behavior for the oxidized nanostructure. These findings, corroborate with the recently published reports based on density functional theory (DFT) calculations.

In terms of applications, the vertically aligned α-MoO_3 nanoblades are applied in a gas sensor device and in electrochemical supercapacitors. For gas sensors, the vertically aligned α-MoO_3

nanoblades showed a significant and fast response to CO gas detection. It is important to note that pre-patterned interdigitated electrode that are widely applied in literature for efficient gas sensing device cannot be applied to our α-MoO_3 nanoblades. This is because, the seed layer used to grow α-MoO_3 nanoblades is highly resistive, which reduces sensitivity of the sensor device. To overcome this challenge, a modified sensor device design, e.g. a top co-planar electrode configuration, is used to enhance the response speed. This sensor configuration can pave the way for new micro- and nano-devices with higher sensitivity and lower energy consumption than their counterparts employing a pre-patterned bottom substrate.

α-MoO_3 is known for its potential to outperform graphite materials in supercapacitor applications. The main challenge in achieving capacitance close to the theoretical value using α-MoO_3 is the low electrical conductivity. We, therefore, carbonized the vertically aligned α-MoO_3 nanoblades and applied them as a hybrid binder free negative electrode material in a supercapacitor device. The reduced vertically aligned α-MoO_3 nanoblades treated under vacuum conditions typically show a higher capacity and stability than their H_2 and N_2-treated counterparts.

Our study addresses important aspects regarding growth and defect control of vertically aligned α-MoO_3 nanostructures and their use in novel device configuration for gas sensing and supercapacitors. A thorough study on the optimal growth conditions and its influence on crystal structure and electronic properties is carried out and the implications on the device performance are demonstrated. Future investigations on the defect control of the α-MoO_3 to further tune the electronic properties and optimization of device designs is required to alleviate our understandings of these materials and their technological advancements.

Zusammenfassung

Die direkte Manipulation der Struktur und Morphologie von Nanomaterialien ist ein vielversprechender Ansatz, um die wachsende Nachfrage von technologisch fortschrittlichen Materialien erfüllen zu können. Ein Beispiel hierfür sind Molybdänoxid (MoO_3) Nanostrukturen, welche in Form von Nanoblättern eine große Oberfläche, eine ausgerichtete Morphologie, eine weite Bandlücke und anpassbare elektronische Eigenschaften aufweisen. Solche Nanostrukturen finden daher in vielen Bereichen, unter anderem der Energiespeicherung und-umwandlung, in der Gassensorik, der Katalyse oder in Bildschirmen und Speichergeräten Anwendung. Ein grundlegender Vorteil dieser Nanomaterialien ist ihre morphologische und strukturelle Anpasspbarkeit, die es ermöglicht, verschiedenen Ansprüchen an die elektronischen Eigenschaften gerecht zu werden

Hierfür wurde in der vorliegenden Studie ein neues Verfahren zur großflächigen, reproduzierbaren und schnellen Synthese von polykristallinen, dichten und vertikal ausgerichteten α-MoO_3 Nanostrukturen entwickelt. Die dabei verwendete hydrothermale Technik ist sowohl einfach als auch kostengünstig und kann auf verschiedenen Substraten, ob leitend oder nichtleitend, angewendet werden. Im Grunde besteht die Herstellungsmethode aus zwei Schritten: Zuerst wird eine Cr/-MoO_3 Wachstumsschicht thermisch aufgedampft, gefolgt von dem Wachstum der Nanostrukturen in einer stark sauren Präkursorlösung. Der Einfluss der Wachstumsparameter wie des pH-Wertes, der Präakursorkonzentration und der Wachstumstemperatur und Dauer auf den Wachstumsmechanismus und die Morphologie der vertikal ausgerichteten α-MoO_3-Nanoblätter wurde gründlich untersucht.

Als Übergangsmetalloxid weist α-MoO_3 mehrere Oxidationsstufen auf, welche die elektronischen . Eigenschaften wie die elektrische Leitfähigkeit um mehrere Größenordnungen verändern können. Dies kann durch Manipulation der intrinsischen Defekte wie Sauerstoffehlstellen, die einen direkten Einfluss auf die Oxidationssufe, also die elektrische Leitfähigkeit, haben, erreicht werden. Das Hauptziel unserer Studie ist es, die Rolle von Sauerstofffehlstellen zu untersuchen, welche durch eine thermale Behandlung in verschiedenen, üblicherweise oxidierenden oder reduzierenden Atmosphären (z.B. O_2, H_2, Vakuum und N_2), im Kristall erzeugt werden. Mithilfe von pa-ra-magne-tisch-er Elektronenresonanz, hochauflösender Elektronenmikroskopie und weiteren Techniken kann die Position von Sauerstofffehlstellenbildung und Restitution von Sauerstoffionen im Kristall bestimmt werden. Diese Phänomene werden mittels der Bildung von Farbzentren und des Polaronenmigrationsmodells diskutiert. Die Ergebnisse können dabei bereits veröffentlichte theoretische Berechnungen und Studien bestätigen.

Bei der Betrachtung der Auswirkung solcher Defekte in der Kristallstruktur auf die optischen Eigenschaften wurde beobachtet, dass diese keinen messbaren Einfluss auf die Bandlücke zeigen. Ein deutlicher Einfluss der Sauerstofffehlstellen auf die Leitfähigkeit des Materials ist hingegen zu erkennen. Das Material kann dabei von halbisolierend zu leitend verändert werden. Vertikal ausgerichtete α-MoO_3 Nanoblätter zeigen n-typisches Verhalten für die reduzierten- und degeneriertes

n-typisches Verhalten für die oxidierten Nanostrukturen. Diese Beobachtungen wurden vor kurzem durch dichtefunktionaltheoretische Berechnungen (DFT) bestätigt.

Vertikal ausgerichtete α-MoO_3 Nanoblätter werden im Rahmen dieser Arbeit sowohl in der Gassensorik zur Detektion von CO-Gas, als auch in Superkondensatoren angewendet. In Gassensoren weisen die vertikal ausgerichteten α-MoO_3 Nanoblätter eine deutliche und schnelle Antwort auf das CO-Gas auf. Es sei darauf hingewiesen, dass vorstrukturierte, interdigitierende Elektroden, wie sie in der Literatur üblicherweise in Gassensoren angewendet werden, hier nicht verwendet werden können. Der Grund hierfür ist, dass die dem Wachstum der α-MoO_3-Nanoblätter zugrundeliegende Schicht einen hohen Widerstand aufweist, was die Sensibilität der Sensoren deutlich beeinträchtigt. Um dieser Herausforderung zu begegnen wird ein modifiziertes Sensorendesign, bestehend aus koplanaren Elektroden, verwendet, das die Antwortgeschwindigkeit erhöht. Diese Konfiguration könnte den Weg für neue Mikro- und Nanotechnologien mit höherer Sensibilität und niedrigerem Energieverbrauch eröffnen.

Theoretisch sollte α-MoO_3 in Kondensatoren eine noch höhere Kapazität als Graphit-Materialien ermöglichen. Jedoch kann dieser theoretische Wert nur schwer erreicht werden, da α-MoO_3 eine geringere elektrische Leitfähigkeit aufweist. Aus diesem Grund wurden reduzierte vertikal ausgerichtete α-MoO_3 Nanoblätter nach dem hydrothermalen Wachstum zusätzlich karbonisiert, um als ein hybrides bindemittelfreies negatives Elektrodenmaterial in Superkondensatoren zu fungieren. Allgemein zeigten die reduzierten vertikal ausgerichteten α-MoO_3 Nanoblätter, die unter Vakuumbedingungen behandelt wurden, eine höhere Kapazität und Stabilität als ihre unter H_2 und N_2 behandelten Pendants.

Basierend auf unserer Studie konnten wichtige Fragen bezüglich neuer Gerätekonfigurationen für vertikal ausgerichtete Nanostrukturen und der Defektkontrolle in ihnen diskutiert und erklärt werden. Eine ausführliche Studie der optimalen Wachtsumsbedingungen, ihres Einflusses auf die Kristallstruktur und elektronischen Eigenschaften wurden durchgeführt und die Implikationen für resultierende Anwendungen wurden demonstriert. Zukünftige Studien zur Kontrolle von Defekten, zur weiteren Modifikation von elektronischen Eigenschaften und zur Optimierung von Gerätedesigns sind notwendig, um unser Verständnis dieses Materials und seiner technologischen Anwendungen zu vervollständigen.

1. Introduction

1.1 Introduction

Metal oxides are considered as a vital class of materials owing to their wide range of properties, which can be fictionalized in various daily life purposes. The origin of their properties is attributed to their electronic configuration [11]. Their versatile properties can be altered by synthesis methods and structure modification. In addition to their simplicity of fabrication and their properties, they are considered as highly competitive to non-oxides semiconductors. Since, they offer a wide range of electronic, magnetic and optical properties.

Moreover, fabrication of metal oxides nanomaterials as 1D, 2D, and 3D nanostructure draws attention to more tremendous technological advances in the applied science. So we can see such fast development in synthesis and structural design has impact on device implementations [12].

1.2 Metal oxides and transition metal oxides

Transition metal oxides form from elements in d-block and one (O) or more elements (Se, S) as we can see in Fig. 1.1.

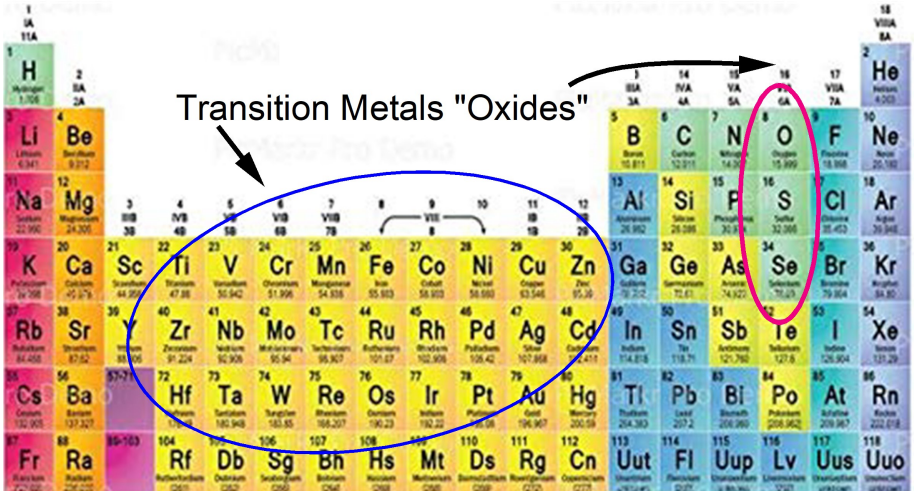

Figure 1.1: Transition metals (blue circle), and one atom at least from red circle as oxides "from [2]".

The nature of the bond between metals and oxygen can be varied between pure covalent bond (e.g. RuO_4) to pure ionic bond (e.g. NiO, CuO), to metallic bond [13]. Additionally, metal oxides exhibit a wide range of electrical categories from metallic to insulator materials as in e.g. RuO_2, $BaTiO_3$,

respectively. One of the main interesting characteristic is insulator-metal transitions, which can be seen in e.g. VO_2 [14] and $LaNiO_3$ [11].

Magnetic properties also show interesting behavior, as some of them have ferromagnetic properties (e.g. CrO_2) and others act as antiferromagnetic material as in e.g. NiO [13].

Moreover, the crystal structure of the metal oxides have polymorphic structures from cubic to triclinic symmetry. Their compositions can exist as binary oxides (e.g. rock salt structure), diodides (e.g. fluorite, rutile structure) and ternary oxides (e.g. perovskites, spinels, bronze structures). A wide range of non-stoichiometry (e.g. Nb, Vn, Fe, Ti, Mo) and defects (e.g. vacancies or doping) cause marked modification in their crystal structure and properties [14].

All of the previously mentioned advantages originate from their partially filled outer d-electrons. Wherein, their chemistry is significantly similar in horizontal rows (in the periodic table) besides basically the similarity in vertical columns (in the periodic table). Unlike p- and s-blocks, the elements have similarity in the chemical properties in a vertical manner. Each row of the transition metals electron configuration role differ and do not follow the aufbau principle (e.g. Cr: $4s^1\ 3d^5$, Cu: $4s^1\ 3d^{10}$, Nb: $5s^1\ 4d^4$). These anomalies can be attributed to extra stability because of the similarity in the energy of n s and $(n-1)$ d subshells [15].

A relative small effect or changes in the material can produce such anomalies electron configurations. That is the reason why most of the metal oxides have multiple oxidation states separated by a single electron, which makes the metal oxides paramagetic materials. In addition, electron-electron repulsion occurs within the increase of the number of electrons in the d-subshell (in further rows) and causes unexpected properties.

Contrary to the p-block as diamagnetic materials, two oxidation states are formed by separation of two electrons. Consequently, the relatively small increase in the ionization energies causes formation of metal ions with the same charge for many of the transition metals, which comes to the point of extensive horizontal similarity in chemical properties. Consecutively, the electronegativity increases in horizontal as well as in vertical manner, in line with increasing electrical and thermal conductivities [16].

1.3 Metal oxides nanomaterial applications

Nucleation of small clusters of molecules can be grown in mono-geneous or/and hetro-geneous manner. Obtaining such materials in different scales with a controlled and well established growth mechanism is the most important phenomena in material science and chemical-engineering branches [17]. Great developments have been achieved by researchers all over the world to fabricate different nanomaterials with different confinement regimes of the particle size as 3D (e.g. nanoparticles), 2D (e.g. nanoblades, flakes and plates), 1D (e.g. nanowires, tubes and rods).

The properties stated extensively in the literature make the nanophase desirable for most daily life applications. In order to synthesize the material in the nanoscale level with different morphologies, two approaches allow us to synthesize them as summarized in Fig. 1.2. Those various synthesis methodologies control very well the fictionalization of the metal oxides nanomaterials. This leads to highly advanced techniques and applications, which have been applied to metal oxide nanomaterials as we can see in Fig. 1.2.

Recently, the industry is focusing on developing sensor technology, portable long lasting batteries, 3^{rd} generation solar cells and antennas by applying such alloys and compounds based on metal oxide nanomaterials as they reveal semiconductor, metal and insulator character [3].

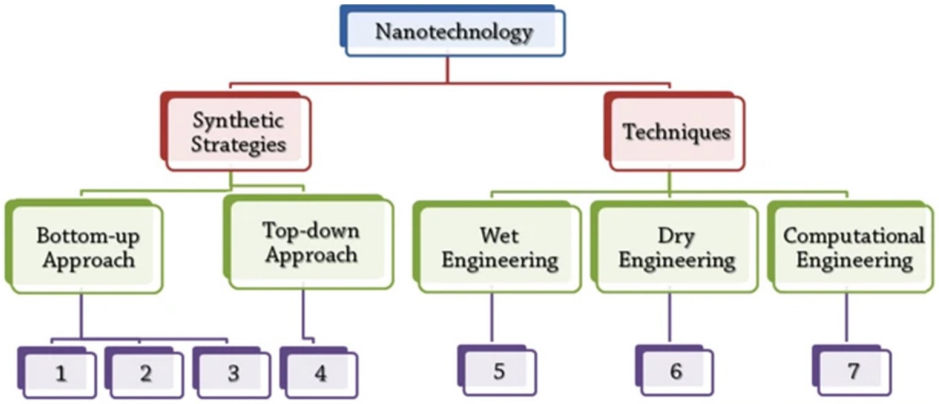

1	2	3	4
Physical *(Gas solid transformation)* 1. CVD and PVD 2. MBE 3. PLD 4. ALD 5. Ion-implantation 6. Spray pyrolysis	**Chemical** *(Liquid solid transformation)* 1. Co-precipitation 2. Sol-gel 3. Chemical reduction 4. Sono- and photochemical 5. Electrochemical 6. Microemulsion 7. Solvo-thermal (hydrothermal) 8. Template/surface derived method	**Biological** *(Bioreduction)* 1. By plants 2. By bacteria 3. By fungi 4. By yeast 5. By algae 6. By biomolecules 7. By agricultural and industrial wastes	1. Bulk nanomachining 2. Fragmentation: Nanomilling, spark erosion, etc. 3. Lithography (Optical, ultraviolet, X-ray, electron beam, laser, etc.)

5	6	7
1. Biomimetic and tissue nanotechnology 2. Bioimaging, biosensing and bioanalytics 3. Nanodiagnostics 4. Nanotherapy 5. Pharmaceuticals 6. Cosmetics 7. Environment harvesting and remediation	1. Information processing, storage and transmission 2. Electronics, optoelectronics and photonics 3. Sensors, MEMs and energy devices 4. Food packaging and storage 5. Pigments, protective glasses, textiles	1. Ab-initio and semi empirical: a. Quantum or molecular mechanics b. Quantum or molecular dynamics of: i. *Nanostructures and interfaces* ii. *Assembly and growth* iii. *Biointeractions* 2. Optimisation and predictability

Figure 1.2: Metal oxide nanomaterial synthesis routes and used techniques and applications (CVD: Chemical Vapor Deposition, MBE: Molecular Beam Epitaxy, SP: Spray Pyrolysis "from [3]".

1.4 Research objective

Among all of the transition metal oxides, molybdenum oxide (MoO_3) is a promising versatile material especially in its most stable phase as alpha phase. In recent times, synthesis of nanomaterials has been broadened in the direction of new engineering concepts like self-assembly and more arranged structures directly on desired device by direct growth procedures on various kinds of substrates (e.g. rigid or/and flexible, conducting or/and non-conducting). The present research was performed with the following goals in mind:

- Synthesis of vertically aligned α-MoO_3 nanoblades as 2D material on different substrates using a low-cost hydrothermal technique for large-scale, dense, reproducible fabrication. To our knowledge, no study has yielded vertically aligned α-MoO_3 nanoblades using the hydrothermal technique.
- Understanding the role of the oxygen vacancies in tuning the electrical properties by applying thermal treatment under common atmospheres. The combination of thermo-chromic characteristic and sensing property of α-MoO_3 treated under different atmospheres can provide a bright explanation about the role of vacancies.
- Applying α-MoO_3 nanoblades to different applications such as a gas sensor and supercapacitor application to address the influence of the morphology and the treatment on their performance in the applications.

2. Scientific Background

2.1 Overview

The main objective of nanochemistry is concerning about developing new bottom-up methodologies for large scale, low cost and better controlling the material's function.

In the nanotechnology approach, the dimensionality is the crucial factor, which can alter the material's physical, chemical, mechanical and other characteristics [18]. One dimensional (1D) nanostructures such as nanowires, blades, rods and flacks generate a considerable interest in terms of combining nanoscale and microscale dimensionality and properties. Sensors and versatile electronics nanodevices based on 1D materials have recently been applied intensively due to their high aspect ratios [19, 20]. Most of the metal oxides have been synthesized as 1D nanostructures and showed a significant impact on the performance in the applied fields.

When we are talking about dimensionality, we must think about defects in the nanomaterials and their types and roles for tuning the material properties. Since the 1920s, stoichiometric FeO showed a non-stable behavior. This demonstrates that most of the metal oxides acknowledge a wide range of homogeneity and stability even in non-stoichiometric conditions. Non-stoichiometric metal oxides are simply mixed valent with integer electron/atom ratios [11].

Moreover, for mixed valance states, wherein the metal cations exist in more than one oxidation state, the properties can be determined based on the movement of the electrons between these different oxidation states. Mainly, oxygen vacancies, as a kind of defects, are the responsible agent for such different oxidation states. Originally, these defects in the metal oxides are responsible for changing the electronic properties and depicted in transition in the material between metal, semimetal, insulator, n- and p-types. (For more information about metal oxides defects please see [11].) In our study, oxygen vacancies have been introduced to α-MoO_3 nanoblades and have been intensively characterized for better understanding their role for tuning the electronic properties.

2.2 Structure configuration

Molybdenum trioxide (MoO_3) as a transition metal oxide has a rich chemical structure with interesting electronic, optical and magnetic properties related to its crystal structure. Molybdenum trioxide (MoO_3) exists in different phases; the most common ones are the thermodynamically stable orthorhombic α-phase (space group $pbmn$), the metastable monoclinic β-phase (space group $p2_1/m$), and the metastable hexagonal h-phase (space group pb_3/m) [21]. These phases are based on the octahedron MoO_6 as we can see in Fig 2.1.

Among the most well known MoO_3 phases, only α-MoO_3 has a desired layer structure, which facilitates the synthesis of different 2D and 1D nanostructures [22]. α-MoO_3 layers consist of thin sheets of bi-layers with a thickness of 1.4 nm [23]. Each bi-layer forms from linked distorted MoO_6 octahedron with corner-sharing along the a-axis and edge-sharing across zigzag along the c-axis

via covalent and ionic bonds [24]. Lamellar formation occurs when the double bi-layers connect through the b-axis *via* van der Waals bonds [25].

On the other hand, β-MoO_3 has shared-corner octahedra MoO_6 in the three dimensions to form the distorted cube structure as we can see in Fig. 2.1. The transition from β- to α-phase is found to be feasible under heat treatment of 350 °C and above [26]. The h-MoO_3 was found to consist of zigzag chains of interconnected octahedra through *cis* position and tunnels along the c-axis [27].

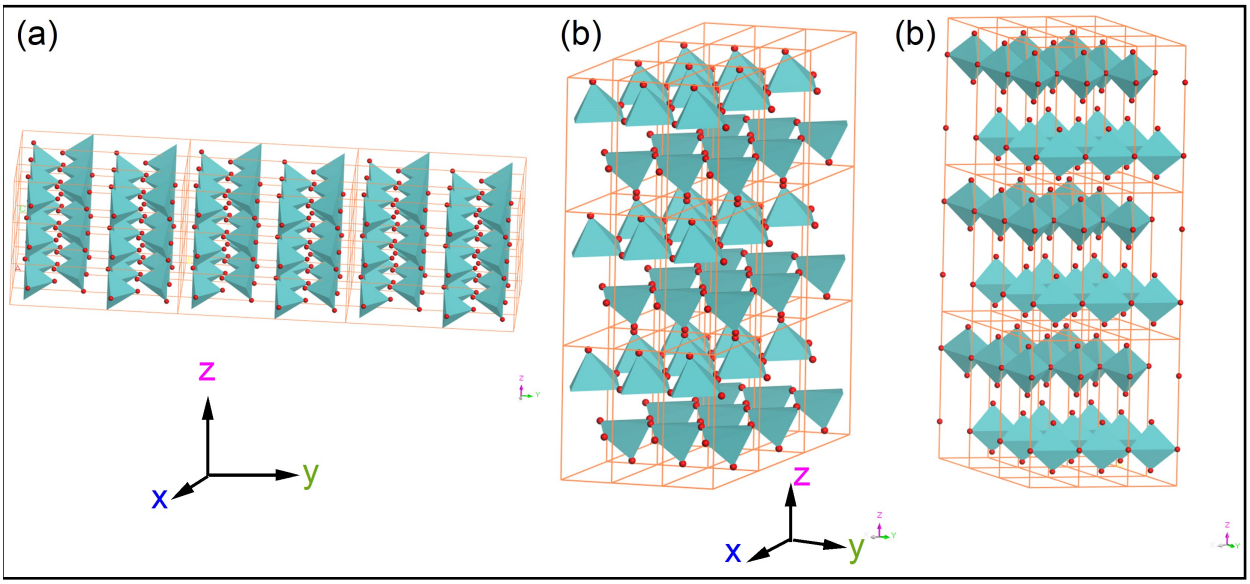

Figure 2.1: (a) α-MoO_3, (b) β-MoO_3, (c) h-MoO_3. All the mentioned phases consist of three crystals.

2.3 Significance of molybdenum trioxide

α-MoO_3 is receiving much attention due to its unique layer structure. Remarkably, α-MoO_3 has the highest work function among non-soluble transition metal oxides in the range of 6.9 eV [21] with a wide bandgap around 3 – 3.2 eV, which makes it transparent. α-MoO_3 has a variety of oxidation states from 2+ to 6+, which are believed to alter the electronic properties [4, 28, 29] in the form of a broad range of the conductivity ($10^{-10} - 10^{-4}$ S cm^{-1}) [30]. The most striking property is the ability for fast intercalation and deintercalation of ions between the layers through van der Waals bonds. Moreover, its high chemical activity and stability lead to innovative progress in the field of energy storage and conversion as in Li-ion batteries and supercapacitors [31].

α-MoO_3 tends to be highly competitive as anode material in a durable Li^+ storage with experimental capacity of 630 mAh g^{-1} [32] and a theoretical capacity of 1111 mAh g^{-1} in comparison to graphite materials with experimental capacity of 372 mAh g^{-1} [33]. As an asymmetric supercapacitor, α-MoO_3 noticeably conducts a wide applied potential up to 2.7 V [34].

Moreover, α-MoO_3 shows a self-photo-recharge ability as a photocatalyst, which combines solar energy conversion and charge storage in a single material system [35]. Thus, α-MoO_3 reveals high ability of O_2 evolution from water and photodegradation of organic compounds using UV illumination [36].

Additionally, a wide range of spectral onset from visible to UV area has been introduced to α-MoO_3 which implies a good response as a photodetector corresponding to its various oxidation states [37].

In the environmental monitoring field, there is a considerable potential interest toward the applied α-MoO_3 nanostructure in a gas sensing device, which proved to evaluate different hazardous gases such as CO [38], NH_3 [39], H_2S [10, 40], H_2 [41], and other organic gases [42].

2.4 Deposition methods of nanostructure MoO_3

A variety of α-MoO_3 nanostructures such as 1D nanobelts and nanorods, 2D nanolayers and nanoblades, and 3D nanospheres have been synthesized *via* different techniques based on two approaches, vapor phase deposition and liquid phase deposition [38, 43]. Solid films are mainly fabricated using vapor phase deposition, which offers limited ability to alter the structure and the morphology [44]. Whereas, the liquid phase synthesis approach is feasible to be used based on common solvents and to be deposited on various substrates [43, 45].

2.4.1 Vapor phase method

Vapor phase deposion can be devided to two methodologies: Physical vapor deposition (PVD) and chemical vapor deposition (CVD) [46]. The PVD method consists of a vaporized source and condensation media, where mostly MoO_3 is used as a source material to be deposited onto different substrates [47, 48]. Until now, this method is widely used despite of its challenging and costly requirements (e.g. high temperature, controlled atmosphere and suitable limited substrates for high temperature deposition) because of the high crystallinitiy of the deposited material [49]. On the other hand, CVD occurs owing to thermal decomposition of a molybdenum based precursor [50]. In CVD, high energy is not required as in PVD, however highly toxic materials based precursor is the major issue for this technique to be widely used [47]. A CVD method relies on different parameters (e.g. substrate's type and structure, precursor sublimation and carrier gas flow rate) [47].

2.4.2 Liquid phase growth

This method demonstrates a convenient way to have a well morphological control. Exfoliation techniques using mechanical and/or sonication in various solvents and surfactants have been used to obtain a wide range of nanostructure MoO_3 [51].

2.5 Chromic effect of α-MoO_3

Among all the significant properties of MoO_3, a great attention has been given to its chromogenics character. The chromic phenomenon is recognized as the ability of the material to change its light absorption as a result of exposure to external excitation sources such as optical irradiation, which is known as photochromic effect, thermal treatment, which is known as thermochromic effect, and electric field, which is known as electrochromic effect.

The induced coloration, which has been described by Pohl and others for alkali halides, remains unchanged when the excitation source has been removed spontaneously [52]. Hence, some materials behave reversibly to their initial state as in MoO_3 [53] by applying for example irradiation or by heating the material at 300 °C under oxygen rich atmosphere, or by applying the opposite polarity of the external electrical field, which causes a bleaching effect. This phenomenon is favorable to be used as a promising applied material into a wide range of applications such as large area displays,

smart windows [54], erasable optical storage media, self-developing photography and holograms [55], and as optical attenuators for human vision, which shows a significant stability in air and irreversible ability over longer time. The coloration-decoloration process can be understood from the following relations Eq.2.1 [56, 57]:

$$MoO_3 + x\,e^- + x\,M^+ \rightleftharpoons M_x\,Mo^{VI}_{1-x}\,Mo^{V}_{x}\,O_3 \tag{2.1}$$

$$\text{Decoloration} \rightleftharpoons \text{coloration} \tag{2.2}$$

2.5.1 Photochromic effect

The pristine MoO_3 films are almost transparent in the visible range of the spectrum except for a small absorption around 800 nm. Whereas after having been exposed to UV light for a certain time, it changes its appearance to dark blue color. The colored film shows absorption bands in the range of $780-900$ nm with a shoulder towards the visible range with Gaussian shape, which is an indication of localized states absorption [58]. In order to reinduce bleaching of the film, thermal treatment under oxygen atmosphere has to be applied. [58] Additionally, the bleaching effect cannot be observed when the film is subjected to irradiation under oxygen rich atmosphere [59].

2.5.2 Electrochromic effect

This phenomenon happens when an external electrical field in one direction (forward or reversible field) has been applied to a sandwich structure device of a deposited MoO_3 layer between two transparent electrodes (SnO_2 or In_2O_3). As a consequence, coloration can be observed. Interestingly, decoloration cannot easily happen if an electrical field of reversed polarity has been applied. This is due to the effect of charge injection of the bottom contact to the oxide layer in the reversible field, which delays the decoloration effect. In order to achieve a bleaching effect, an insulating layer should be deposited between one of the electrodes and the oxide layer. This alters the charge injection from the electrode to α-MoO_3 layer, and subsequently ejection of the electrons from the trap levels can be occurred (bleaching effect). Then bleaching can be observed (explained in the coming section 2.6) [56].

2.5.3 Thermochromic effect

In general, when heating MoO_3 films under a reducing atmosphere such as a H_2 rich atmosphere, deep color can be seen, which leads to strong absorption in a non-optical band gap region as explained in section 2.5.1. [59]. Various studies have demonstrated a linear relation between the time of heating the films under reducing atmosphere and the extension the absorption region. The decoloration effect has been observed ultimately in all films colored through photo, electro, thermal coloration process *via* a thermal heating in a temperature of $\geqslant 300\,^{\circ}C$ under O_2 atmosphere [53,60].

2.6 Mechanism of the chromic effect

A number of theoretical models propose obvious explanations for the origin of the coloration-decoloration related optical absorption, and it was found to be a result of one of the following reasons [61]:

- Inter-band transition (excitation) between a filled conduction band and a higher excited bands, which does not lead to a lower energy absorption because these later bands spread over a large energy range[not applicable in the present study].
- Charge transfer from a valance band to a split-off Mo^{5+} state; this means that charges transfer from the oxygen valance band to the Mo^{5+} ion have a similar energy to the band gap with a very small difference (slightly less than the band gap energy).
- Color center formation in oxygen vacancies (F, F^* centers)
- Inter-valence transfer absorption, which requires highly delocalized electrons with overlapping to metal ions.
- Small polaron absorption.

2.6.1 Color center model

An early study supposed by Deb *et al.* [53] suggested that the light induced coloration effect in MoO_3 films is due to a color center formation. The color center concept has been hypothesized as the existence of metal ions (cations) in two oxidation states (Mo^{6+} and Mo^{5+}), which suggests a substoichiometric oxide. The oxygen vacancies in the substoichiometric oxide induce free electrons to be trapped into these cation sites. According to this model, the oxygen vacancies are believed to be the major cause of the coloration process [56, 58, 62, 63].

There are two types of color centers (F, F^*) as supposed by Pick *et al.* [64, 65]. The F^* center is described as a broad absorption band, which is weakly bound and can be bleached and ionized easily at low temperature around 20 K, and this behavior supports the photoconductivity at low temperature. On the other hand, F centers require high temperatures to be ionized and these centers supply electrons to F^* centers as a bound excited state [66].

There are some limitation to this model, e.g. to provide an adequate explanation why in some cases the density of the color centers is much higher than the oxygen vacancy concentration. Besides, in some cases the evidence of the color center bands is hardly seen from their spectra, which leads to other models [58].

2.6.2 Inter-valance charge transfer model (IVCT)

This model was proposed by Faughnan *et al.* to explain the electrochromic effect in WO_3, which is known as a double insertion/extraction of ions and electrons model. IVCT model found acceptance by researchers to elucidate the photochromic mechanism of transition metal oxides, specifically MoO_3 and WO_3 [58, 67].

This model suggests that we have adsorbed water molecules on the surface of the oxide film as a result of the preparation process and/or exposure to ambient condition. The water molecules can be dissociated into oxygen and protons by exposing the films to external excitation such as UV radiation ($h\nu \geq E_g$) or by heating up the films. The produced protons diffuse into the lattice and interact with free electrons (produced by the external excitation) in the crystals, which can

be found, wherein the radical oxygen occupies the vacancy sites or electrons occupy the vacancy due to the escaped molecular oxygen into the atmosphere. The diffused protons in the lattice form bronze molybdenum oxide and are causing an inter-valence charge transfer absorption between Mo^{5+} to Mo^{6+} sites (i,j sites). Subsequently, the coloration effect occurs when the inter-valence-charge transfer between valance band -like of Mo^{5+} to conduction band-like of Mo^{6+}. Those two sites are nonequivelant in the configuration, but they are energetically similar. As we can see in the following relation [58]:

$$MoO_3 + h\nu \rightarrow MoO_3^* + e^- + h^+ \tag{2.3}$$

$$2\,h^+ + H_2O \rightarrow 2\,H^+ + O \tag{2.4}$$

$$MoO_3 + x\,e^- + x\,M^+ \rightleftharpoons M_x\,Mo^{VI}_{1-x}\,Mo^{V}_{x}\,O_3 \tag{2.5}$$

$$Mo_i^{6+} + Mo_j^{5+} \overset{h\nu}{\rightarrow} Mo_i^{5+} + Mo_j^{6+} \tag{2.6}$$

Additionally, a photo corrosion effect can happen, which can be understood according to the following relation:

$$e^- + h^+ \rightarrow \text{heat} \tag{2.7}$$

$$MoO_3 + 2\,h^+ + 2\,H_2O \rightarrow MoO_4^{-2} + 4\,H^+ + \frac{1}{2}\,O_2 \tag{2.8}$$

$$H^+ + e^- \rightarrow \frac{1}{2}\,H_2 \tag{2.9}$$

This model provides no clear explanation why the coloration effect of MoO_{3-x} cannot be observed in a lower substoichiometric level when $x < 0.3$.

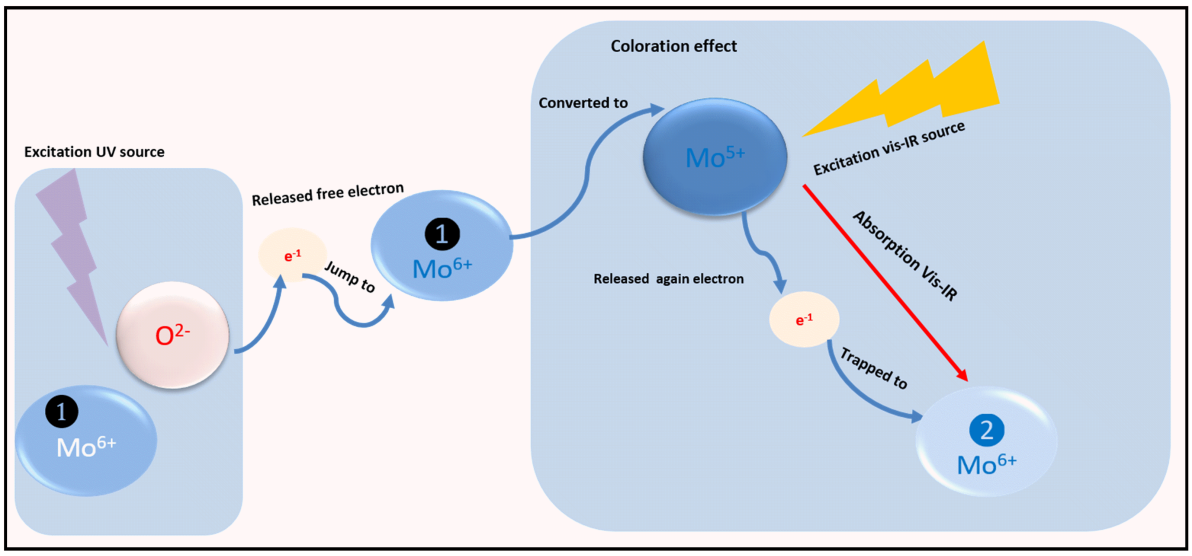

Figure 2.2: Inter-valance charge transfer model and polaronic model.

2.6.3 Polaronic model

This model is based on the polaron concept supposed by Landau [68]. The polaron consists of an electron or hole bounds to a potential well created between displaced atoms from their equilibrium position and their free charges cloud [69]. Consequently, the wave function takes place to one lattice site.

The small polaron migration model is a small refinement of the inter-valance charge transition model, with self-trapping of the charge carriers between the nonequivelant Mo^{6+} sites. The related absorption to the polaron migration occurs by hopping between neighboring other cation site (i-j). Hence, the polaron (charge) tends to occupy lower energy lattice sites and causes a polarization to its surroundings. The bonds in MoO_3 are ionic and covalent bonds, and they form large polarons (long range electron lattice interaction) and small polarons (short range electron lattice interaction), respectively [58, 70]. This effect can be understood according to the following relation [61]:

$$Mo_i^{6+} + Mo_j^{5+} + \text{photon} \rightarrow Mo_i^{5+} + Mo_j^{6+} \tag{2.10}$$

Whereas, the excess energy during the photon-assisted hopping is released as phonons.

2.6.4 The modified color center formation

Inter-valance charge transfer and polaronic models introduced acceptable explanations for the absorption in non-band gap absorption regions, but for the lack of coloration in very low defect levels no comprehensive verification has been given.

The Deb model suggested that the existence of the oxygen vacancies is associated with different oxidation states of the cations such as Mo^{4+} or/and Mo^{5+}. It gives the same concept of color center formation related to trapped electrons in the vacancy.

According to this modified model, Mo^{4+} or/and Mo^{5+} form as a result of vacancy existence. The oxygen vacancy considered as v_o^0 originally has two electrons as a defect state closer to or inside the valance band (holds two electrons). One electron can be released to create v_o^{+1} (Mo^{5+}). This behavior leads to an induced rearrangement of Mo ions due to Coulomb repulsion force between the positive charges of vacancies (v_o^{+1}, v_o^{+2}) and the metal cations. This shifts the defect level upward in the band gap. The optical transition between these charged defect states as (v_o^{+1}, v_o^{+2}) or Mo^{5+}, Mo^{6+} cause the coloration effect [70, 71].

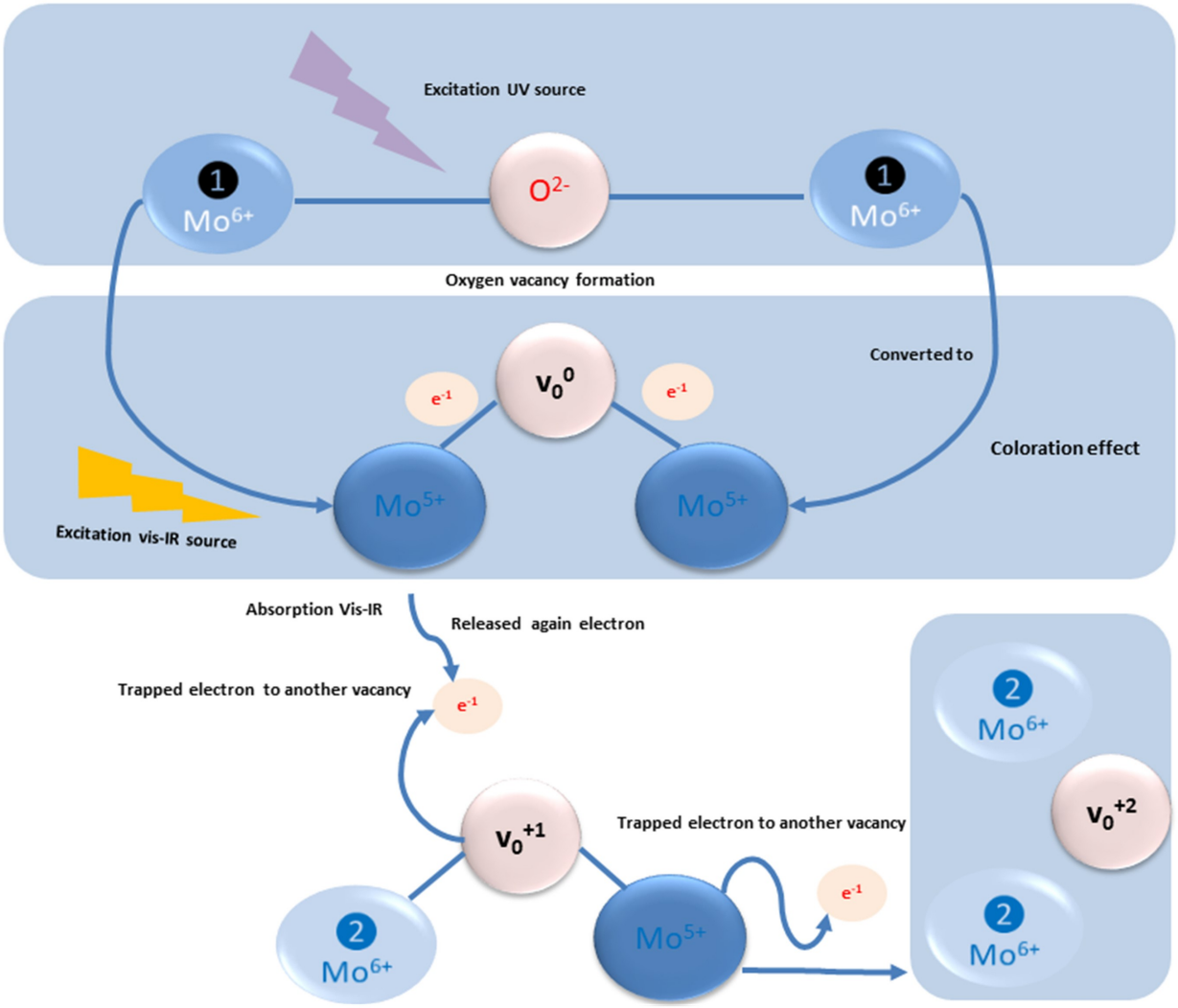

Figure 2.3: Modified color center formation model.

2.6.5 Summary of those models

Taken together, those models are the most acceptable ones to explain the formation of the oxygen vacancies and related color centers. It is worth mentioning that the coloration effect can be seen more easily in highly disordered films in comparison to crystalline films. The coloration can be induced *via* different excitation sources such as optical, thermal annealing, electrical and ionized radiation, which shows a small variation in the absorption peak position and its full width at half maximum regarding these different excitation sources [70]. The previously mentioned models can be divided into two categories regarding Mo^{5+} formation and the induced coloration:

- According to IVCT and small polaron models, there is an increase in Mo^{5+} when the film is exposed to an excitation source (such as UV source). The electrons are released from the valance band (p oxygen orbital) to the conduction band (one d orbital of high energy Mo^{6+}), which reduces the oxidation state of the metal ions to Mo^{5+}, and the coloration effect can be observed in this stage. The concentration of the lower oxidation states corresponding to

the coloration effect increases significantly when the exposure period of the UV excitation is increased [53, 72]. Following that, absorption in the visible near IR region can be observed, which excites the electrons from Mo^{5+} to lower energy Mo^{6+} as summarized in Fig. 2.2.
These models fail to declare the role of the oxygen vacancies related to lower coloration efficiency [70].

- As has been demonstrated by Deb *et al.* [70, 72], the color centers form as a result of oxygen vacancy formation with trapped electrons. This model supposes no changes in the concentration of Mo^{5+} (Fig. 2.3). The oxygen vacancy implies that two Mo^{5+} atoms are in the valance band, whereas one electron can be excited to the conduction band, where it changes the oxidation state to Mo^{6+} and forms the color center. The color center can absorb visible IR light to release one electron to the conduction band in a different state of energy, which acts as a trap level itself. The important thing is that the free electron can jump between different sites of the oxidation states without changing the total concentration of each oxidation state, even though color changes can be observed [70].
  Deb proved his interpretation using electron paramagnetic resonance (EPR) signals associated with electrons trapped by a negative ion vacancy, which form the color centers. This relation can be written in the form of the Kröger-Vink notation [4, 73]:

$$O_o^x + 2\,Mo^{6+} \rightarrow v_o^{\bullet\bullet} + 2\,Mo^{5+} + \frac{1}{2}\,O_2 \tag{2.11}$$

where O_o^x is the oxygen anion in its original position in the lattice, and $v_o^{\bullet\bullet}$ is a double positively charged oxygen vacancy.

2.7 Optical and electronic properties of MoO_3

A number of optical band gap values of α-MoO_3 have been reported, which affirm the differences in the content of the oxygen vacancies. α-MoO_3 is a wide band gap material around 3 – 3.1 eV. Originally it is a d^0 oxide, which is composed of a valance band of O–2p band and a conduction band of Mo–4d band as can be seen in Fig. 2.4 [4]. In its stoichiometric form, it behaves as an insulator material, but it tends to be n-type since its Fermi level is closer to the conduction band. This is due to the fact that there is always an equilibrium concentration of oxygen vacancies, as has been given by thermodynamics in 2.6.1.

The electronic band depends on the oxidation states of the Mo–4d band. The increase in the oxygen deficiency is connected to partial filling in the Mo–4d band within the bandgap, which produces states closer to its Fermi level until it reaches the metallic oxide MoO_2 (Fig. 2.4) [4, 74].

According to Nethercot's postulate of geometry, the non-stoichiometric MoO_{3-x} shows a linear relation between E_F and the oxygen deficiency x [73, 75]. As we see from Fig. 2.4, the oxygen deficiency shifts the Fermi level closer to conduction band and consequently, the work function decreases [73].

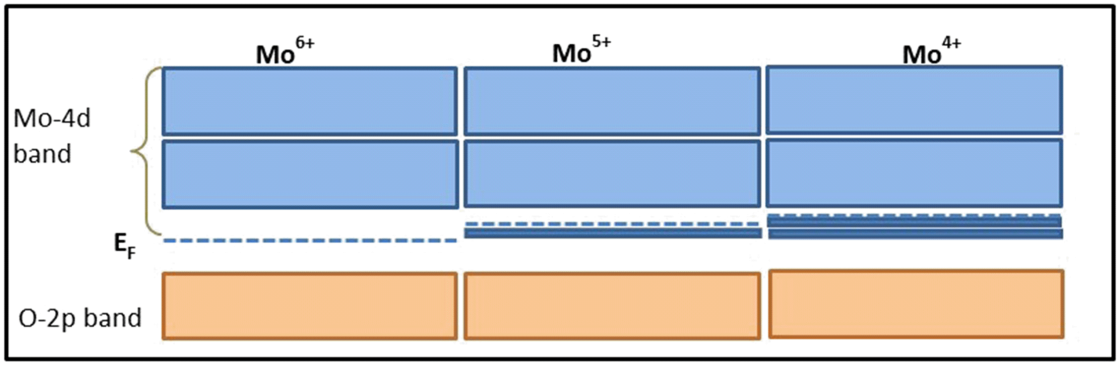

Figure 2.4: Schematic of stoichiometric and gradual increase of oxygen deficiency for the electronic band of α-MoO_3 "after [4]".

The work function is considered an important parameter for charge extraction, since it is the energy required to remove electron from the Fermi level to the vacuum level. Initially, the reproduceability of the work function of MoO_3 is very hard to obtain because of the uncontrollable effect of oxygen deficiency in the material, which leads to doubts about the absolute value [73]. It was demonstrated that higher oxidation states of the cation tend to induce a higher work function.

There is another important parameter connected to the metal oxide: It is the electronegativity, which is favorable to understand many of the chemical parameters. The electronegativity has a proportionality, which implies a linear relation to the work function and the oxidation number of the metal ion.

Moreover it is also found that the work function tends to vary according to the type of the substrates used for deposition. This is attributed to the substrate's activity: More reactive materials induce reduction of the cation (Mo^{6+} to Mo^{5+} and/or Mo^{4+}), which causes metallic or semimetallic behavior near the interfaces. Hence, α-MoO_{3-x} shows semiconductor behavior for $0 < x \leq 0.125$, and for $0.125 \leq x < 1$ it shows quasimetallic behavior [76]. The electrons injected by reducing the oxidation state of the metal cations are delocalized electrons, which act as free electrons as demonstrated by the Drude model [77]. Consequently, the electrical conductivity increases for the

reduced form in comparison to the stoichiometric form. Controlling the role of the oxygen vacancies and the related conductivity depend highly on the reduction method, time, and other parameters due to the asymmetric nature of α-MoO_3 crystal configuration [76].

3. Experimental Details

Vertically aligned α-MoO_3 nanoblades were directly grown on the substrates using the hydrothermal technique followed by treatment at high temperature under oxidizing and reducing atmospheres. They have been addressed to structural, spectroscopical and electrical characterization techniques. The vertically aligned α-MoO_3 nanoblades have been applied to gas sensor and supercapacitor applications. In this chapter, the synthesis technique, preparation, characterization techniques and the used workstations for devices performance test have been introduced.

3.1 Substrates cleaning procedure

Different types of substrates such as commercial fluorine-doped tin oxides (FTO, sheet resistance 15 Ω/cm^2), Si wafers (100), p-doped Si/SiO_2 wafers (SiO_2 thickness 1 μm) were cleaned using a standard procedure by sonication in acetone (5 min), isopropanol (5 min), and ethanol (15 min), followed by drying in a nitrogen gas flow. The cleaned substrates were treated with a UV/ozone cleaner (Ossila) for 20 min to form a polar surface to improve the adhesion of the α-MoO_3 seed layer [78].

3.2 Thermal evaporation coating technique

The seed layers of α-MoO_3 have been deposited by using the thermal evaporation technique (Tectra mini-coater) at a base pressure of $< 2 \times 10^{-6}$ mbar with applied current and power of 15 A and 1 kW, respectively. As evaporation sources for the seed layer, Molybdenum (VI) oxide powder (99.98 %, Sigma Aldrich) and chromium plated tungsten rods (99.9 %, Testbourne) have been used. The thickness of the film was monitored using a quartz micro-balance with a resolution of ± 0.1 nm.

3.3 Hydrothermal technique

An aliquot of concentrated hydrochloric acid (HCl) was added dropwise to an aqueous solution of $Na_2MoO_4 \cdot 2\,H_2O$ into a PTFE autoclave liner to yield a total volume of 21.5 ml. The mixed solution was stirred for at least 10 min to dissolve the precursors completely. Then the seed layer coated substrates were placed upright into a PTFE holder and submerged in the prepared precursor solution. Finally, the PTFE autoclave liner was sealed and put into a preheated oven at 180 °C for 210 min. After the reaction, the autoclave was rapidly cooled down to ambient temperature in a water bath. The grown MoO_3 substrates were washed with ethanol and allowed to dry under ambient conditions. The synthesis procedure and related growth conditions and parameters were written by me and corrected by Dr. Klaus Boldt at department of chemistry & Zukunftskolleg, University of Konstanz.

3.4 Characterization techniques and applications

3.4.1 X-ray diffraction

X-ray diffraction (XRD) analysis was performed using a Bruker AXS D8 Advance diffractometer employing the Bragg-Brentano geometry and Cu-Kα radiation in combination with grazing incidence (GIXRD). Measurements were performed in the range of $5-60^{o}$.

The XRD data acquisition was done by Ms. Brigitte Bössenecker and Elana Harbalik in the "Particle Analysis Center", supported by the Deutsche Forschungsgemeinschaft (DFG) through the Collaborative Research Center SFB 1214 project Z1.

3.4.2 Scanning electron microscope (SEM)

Surface imaging was done using two different SEM versions: 1 - Zeiss Cross Beam 1540XB field emission SEM using an electron energy of 5 kV. 2 - KMAT GeminiSeM 500 by Zeiss using an electron energy of 5 kV. The elemental mapping was achieved using electron the dispersive X-ray spectroscopy of an Ultimax standard large area analytical silicon drift EDS 100 detector.

3.4.3 High resolution transmission electron microscope (HR-TEM)

High resolution transmission electron microscope (HR-TEM) images were obtained on JEOL-2010 microscope operated at 200 kV. The HR-TEM samples were prepared on conventional TEM grids (carbon-coated copper grid) supplied by Quantifoil GmbH. Furthermore, the obtained nanostructures were analyzed using selected area electron diffraction (SAED), bright-field imaging, and zero-loss filtered high-resolution TEM.

The data acquisition was done by Dr. Marina Krumova at the Nanostructure Laboratory, Physics Department at the University of Konstanz. The data has been analyzed by myself within the scope of my current Ph.D. studies.

3.4.4 Electron paramagnetic resonance (EPR)

Electron paramagnetic spectroscopy (EPR) spectra have been recorded using the following steps: Powder form of α-MoO_3 nanoblades were prepared by placing the vertically aligned α-MoO_3 nanoblades onto FTO substrates in a DI water beaker, and they were introduced to an ultrasonication bath for a time of 3 min (peel off the powder nanoblades on the water). The powder was clarified using a centrifuge under acceleration of 9000 rmp for 20 min. The α-MoO_3 nanoblades powder was annealed in oxidizing (O_2) and reducing atmospheres (H_2, vacuum, N_2), separately, as mentioned before for the substrates.

As-prepared, oxidized and reduced α-MoO_3 nanoblades have been filled into quartz tubes (inner radius of 2 mm, Technical Glass Products, Inc.) and pressed slightly with a plastic piston from the top to avoid any occasional movement of the powder particles in the magnetic field. The weight of the powder samples was determined as the difference in masses of the empty quartz tubes and the filled ones. The height of all samples in the quartz tubes was $\approx$1 cm, which corresponds to the length of the sensitive part of the resonator.

Continuous wave (CW) EPR spectra were recorded at the X-band ($\approx$9.3 GHz) on an Elexsys E580 EPR spectrometer (Bruker Biospin) equipped with a split-ring resonator ER 4118X-MS3 (Bruker Biospin). The measurements were performed at 80 K, which was realized in a gas-flow cryostat CF935O combined with an intelligent temperature controller ITC503 (both from Oxford Instruments) and using helium as a cooling agent.

Experimental settings were adjusted to avoid any saturation and over-modulation of the spectral lines. Typical experimental settings were: Modulation amplitude of 1 G, modulation frequency of 100 kHz, microwave power of 0.64 mW, magnetic field range of 1000 G, time constant of 40.96 ms, conversion time of 40.96 ms, number of points per scan 4096, and number of scans 4.

The standard $CuSO_4$ sample was prepared from $CuSO_4 \cdot 5\,H_2O$ as a 10 mM solution in a H_2O/glycerol (8:2 v/v) mixture. 30 μL of this solution were transferred into a quartz tube and shock-frozen in liquid nitrogen prior to the measurement. Spectral simulations were performed using the EasySpin software package for Matlab [79].

The measurements were done in the laboratory of the working group of Prof. Malte Drescher, Chemistry Department at the University of Konstanz. The data recording and analysis were done by myself under the supervision of Dr. Mykhailo Azarkh, the manager of EPR units. The data simulation was operated by Dr. Mykhailo Azarkh.

3.4.5 X-ray photoelectron spectroscopy (XPS)

The samples treated under oxidizing atmosphere (O_2) and reducing atmospheres (H_2, vacuum, N_2), grown on Si/SiO_2 substrates, were introduced into a standard Omicron XPS system with a Mg X-ray source in an ultrahigh vacuum (UHV) system. CASA XPS software was used for data fitting, and C1s was used as a reference for data calibration.

The measurements were done in the laboratory of the working group of Prof. Mikhail Fonin, Department of Physics at the University of Konstanz. The data has been recorded by Prof. Muhammad Sultan, National Center for Physics at Quaid-i-Azam University Campus Islamabad. The data analysis was performed by myself under the supervision of Prof. Muhammad Sultan.

3.4.6 UV-visible spectrophotometer

The diffuse reflectance spectra have been recorded using a Cary5000 system (Agilent technologies) with spectra incident wavelength in the range of 300 – 800 nm in a 150 mm integrating sphere. The samples were housed in the integrating sphere's backside, where the incident light illuminates the samples perpendicularly. In addition, the 100 % and 0 % transmissions have been measured to calculate the diffuse reflectance values correctly.

3.4.7 Photoelectron spectroscopy in air (PESA)

Photoelectron spectroscopy in air (PESA) measurements have been carried out using an AC-2 instrument (Riken Instruments). The analysis has been performed at 2400 nW excitation light power and in a scan range of 4.6 – 6.2 eV with a step size of 0.05 eV. The measurements have been recorded for three different positions on the substrate, and they were repeated three times for each position.

3.4.8 Raman spectroscopy

Raman spectra have been recorded using a Mono-Vista CRS system by Spectroscopy and Imaging GmbH using a laser excitation energy of 488 nm. The measurements have been done in the laboratory of Prof. Andreas Zumbusch, Chemistry Department at the University of Konstanz. The samples have been measured by Dr. Peyman Zirak Yousefabadi. The data analysis was done by myself.

3.4.9 Self-made high temperature DC-electronic gas sensing workstation

A home-made multi-purpose chamber has been designed to be able to perform several measurements, such as the DC-current-voltage characteristics under vacuum and other different atmospheres, and DC measurements under different gases and UV top illumination.

The DC-gas sensor workstation (see Fig. 3.1) has been designed by myself and was realized at the University of Konstanz by Mr. Louis Kukk, a technician in the group of Prof. Eva Weig, Physics Department; Mr. Hamidreza Riazi-Nejad, a technician in the group of Prof. Schmidt-Mende; Ing. Simon Haus, a nanotechnology engineer in the group of Prof. Scheer, Physics Department; Ing. Bruno Erne, an electrical engineer at the workshop; Mr. Michael Weiland, a technician in precision mechanics at the workshop; and Mr. Ekkehard Moser, a technician in apparatus construction at the workshop.

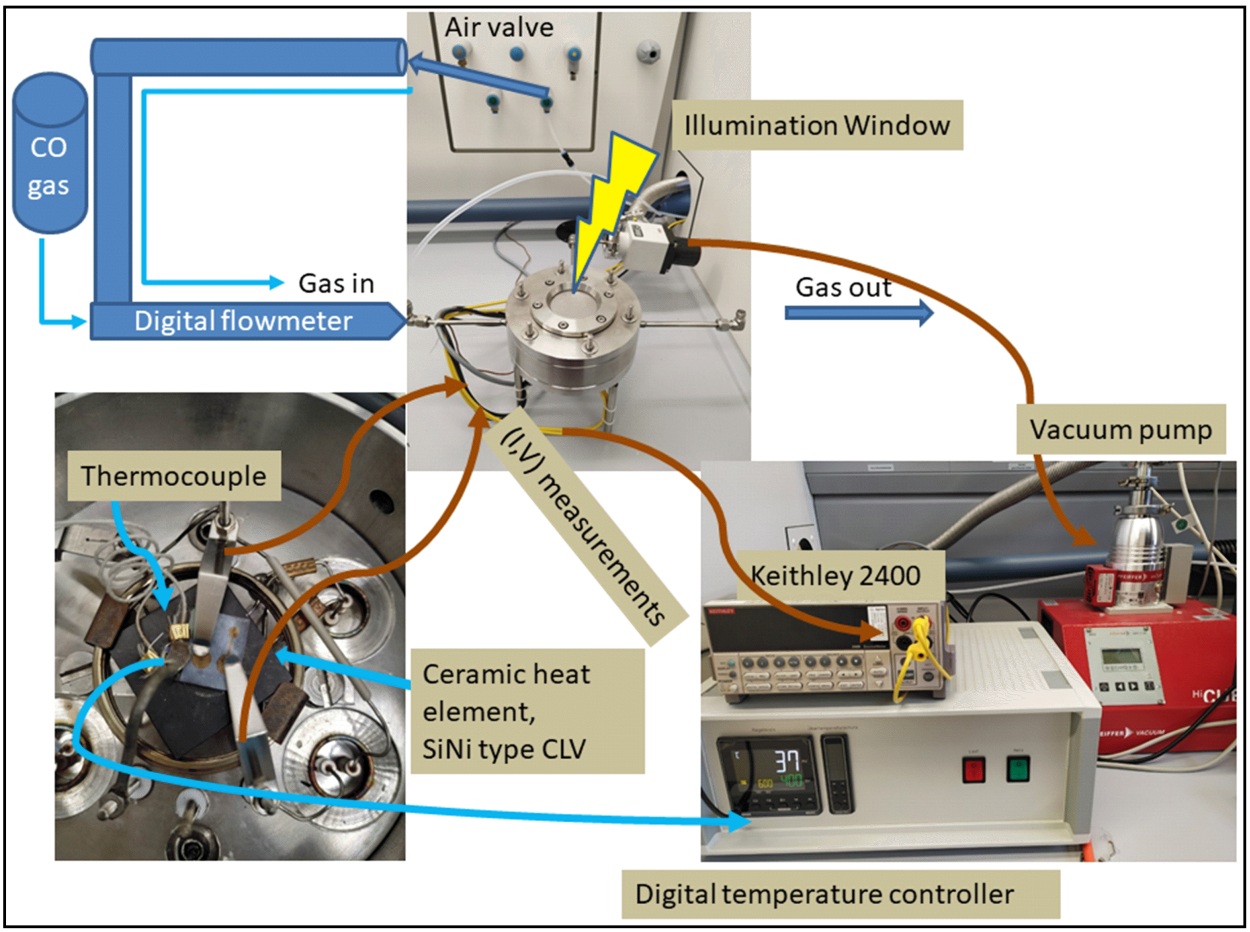

Figure 3.1: Schematic of a home-built DC-gas sensor workstation

Temperature-dependent current-voltage characteristics have been measured using a home-made DC chamber, with an embedded ceramic heat element (SiNi type CLV) connected to a digital temperature controller TR400 with CX-Thermo OMRON E58-CIFQ2. The temperature is adjusted digitally through a Pt-100 thermocouple that is fastened to the top of the substrates and connected to the temperature controller. The samples were measured in the temperature range of 30 – 140 °C with steps of 10 °C in 30 sec and a stabilization time of 5 min.

Purpose-built current-voltage contacting probes have been made of Ni foil covered with an evaporated thin layer of Cr as adhesion layer followed with a Au layer of 150 nm thickness (reduce the resistance between the probes and our top electrodes on the vertically aligned α-MoO_3 nanoblades). As extreme precaution, a Ni foil has been used to make sure that the vertically aligned nanoblades are not destroyed by the weight of the contacting probes.

A Keithley 2400 source meter was incorporated to the contacting probes and the data acquisition was controlled by a Matlab program. The seed layer electrical characterizations at room temperature have been evaluated by using a nano-probeers miBot^{TM} NANO-SM100 system placed and operated by KMAT GeminiSeM 500 by Zeiss. The measurements have been done by Stefan Schupp, a Ph.D. student in a group of Prof. Schmidt-Mende in the Physics Department at the University of Konstanz.

For the gas sensor measurements, the gases air and carbon monoxide (CO) were controlled by a digital flowmeter (Bronkhortst controlled by Flow DDE and flow tune program). The flow was kept constant at 500 mL/min. The vertically aligned α-MoO_3 nanoblades were connected to the electrodes, heated to the desired temperature, and kept there for 5 min for stabilization. Then we applied a certain voltage and recorded the current vs. the time within the gas on/gas off mode.

3.4.10 Supercapacitor workstation

The electrochemical activity evaluation has been performed using cyclic voltammetry (CV), galvanostatic charge-discharge (GCD) and electrochemical impedance spectroscopy (EIS) techniques using a PARSTAT MC-1000 Electrochemical Workstation and VERSA STUDIO software. All tests were accomplished in a three-electrode system using platinum (Pt) as counter electrode and a saturated calomel electrode (SCE) as reference electrode in a 0.5 M Li_2SO_4 electrolyte where our films are used as working electrodes.

The measurements have been done within the scope of a collaboration DAAD exchange program with a group of Jr. Scientist, Dr. R. Ananthakumar at the School of Advanced Research in Polymers (SARP), Laboratory for Advanced Research in Polymeric Materials (LARPM), Central Institute of Plastic Engineering and Technology (CIPET), India. The study follows the research topic of "Hybrid 3D Architecture Electrode for Smart and Flexible Supercapattery". The measurements have been performed and analyzed by Ankita Mohanty, a Ph.D. student in the group of Dr. R. Ananthakumar.

4. Synthesis Procedure and Structural Analysis

4.1 Overview [1]

[1] The synthesis of various MoO_3 nanostructures has been achieved through different methods [38], including electrodeposition [26], thermal evaporation [80], chemical vapor deposition [81], sonochemical methods [82], flame [83], aqueous solution processes [84], laser-assisted evaporation [85], and ultrasonic spray pyrolysis [86]. The morphological engineering development in the nanomaterial science is owing to the unique characteristics of large surface area, the small dimensions comparable to the Debye length, superior stability, and easier functionalization, which differ from the respective bulk properties [87, 88].

However, growing dense vertically aligned 1D MoO_3 nanostructures in a reproducible manner remains a big challenge. Vertically aligned 2D and 1D nanostructures films were found to enhance the sensitivity of gas sensing materials in comparison to a random network of 2D materials on a substrate [9, 88, 89].

Recently, highly efficient, low power consuming, and long-lasting vertically aligned nanowire-based multifunctional devices have been demonstrated in different applications such as MEMS-based sensors and flexible wearable and portable safety clothes [90] and multisensor chips (optical, magnetic and conductometric gas sensor) [91]. Vertically aligned metal oxides have been integrated into organic solar cells, which showed improved charge separation and extraction [92].

The aforementioned synthesis procedures for vertically aligned 1D and 2D MoO_3 rely on a range of sophisticated techniques, such as using thermal evaporation at a very high boat temperature of 1100 °C to prepare the structures on Si substrates [93], plasma-assisted paste sublimation on nickel coated glass [60], and also a modified hotplate method at 450 °C on Au/Si substrates [94]. Those methods require high temperature or are limited to certain types of substrates. Furthermore, the final product is neither highly reproducible nor does it provide a very dense structure, but only a low number of wires or flakes per unit area.

The hydrothermal process is the most versatile and cheapest technique employed in nanochemistry to grow a variety of nanostructures. It has been used intensely for synthesis of MoO_3 nanostructures as a powder or dispersion. Additionally, the hydrothermal technique has been used to grow direct 2D and 1D structures of other metal oxides on substrates such as ZnO [95], TiO_2 [96], and SnO_2 [97]. However, we are not aware of such synthesis directly on substrates for MoO_3.

An essential goal of this work is to grow vertically aligned, densely packed MoO_3 structures as films on substrates, such as transparent conducting oxides (TCOs), Si wafers, and flexible substrates. Here, we report specifically an efficient method to produce a homogeneous and dense

[1] Sections 4.1-4.3 were written based on [1], where I performed the experiments and wrote the paper with the support and intense discussion with the co-authors.

vertically aligned film of one-dimensional α-MoO_3 nanoblades on seeded substrates, using a highly reproducible hydrothermal method with short reaction time. The synthesis proceeds without the use of any additional organic surfactants, catalysts, or dispersing additives.

Here, we studied various parameters such as reaction time, precursor concentration, and pH value to control the growth, the morphology, and the phase evolution of the MoO_3 nanostructure [1].

4.2 Vertically aligned 2D MoO_3 synthesis route [1]

A dense layer of vertically aligned α-MoO_3 nanoblades was prepared on various substrates through a process which consists of depositing the seed layer, followed by hydrothermal synthesis of a vertically aligned α-MoO_3 film. This can be seen in Fig. 4.1 and will be explained in detail in the coming sections [1].

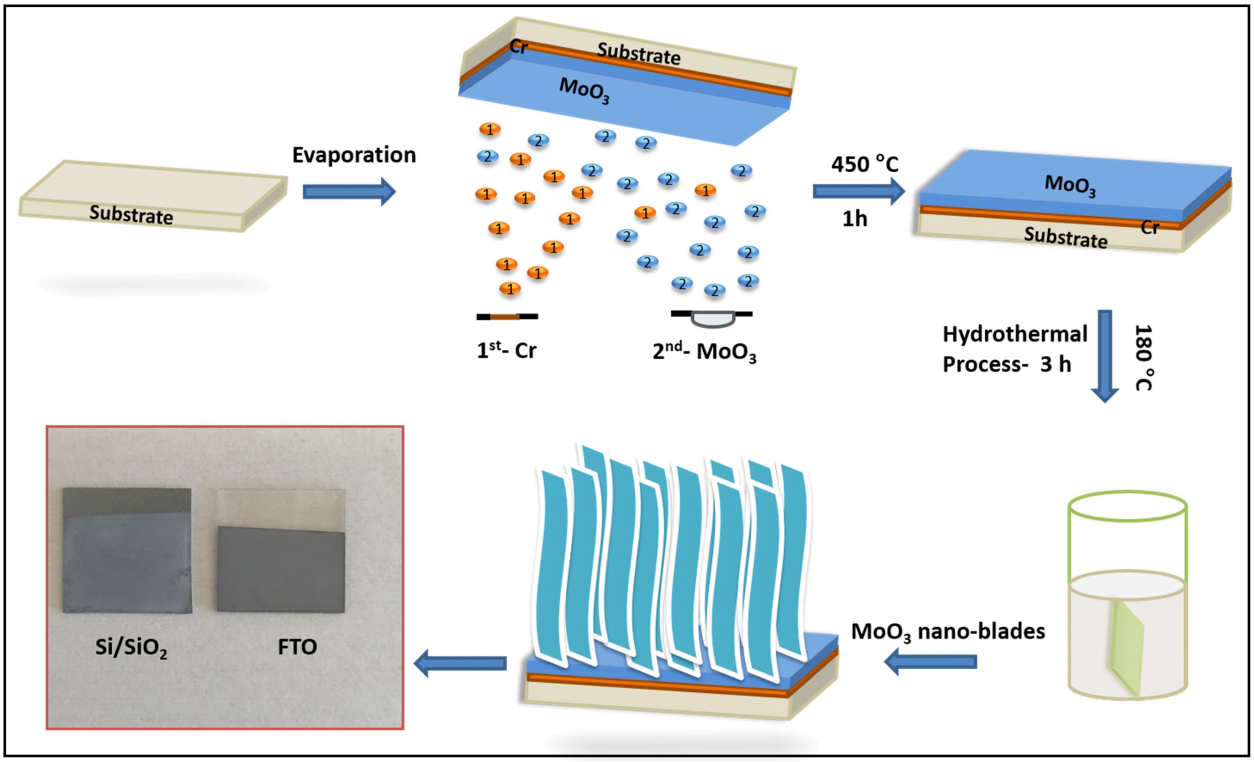

Figure 4.1: Schematic illustration of the synthesis process for vertically aligned α-MoO_3 nanoblades "from [1]".

4.2.1 Seed layer deposition

To ensure proper adhesion of the nanostructures on the substrate, a thin adhesion layer has to be deposited initially. We found that only a thermally deposited layer of the chromium (Cr) worked well as adhesion layer for the MoO_3 growth. The structure and composition of the Cr layer were characterized using GIAXRD at a grazing incidence angle of 0.5°. In Fig. 4.2, the XRD patterns of the Cr adhesive layers with thicknesses of 5, 10 and 20 nm are presented on Si/SiO_2 substrates.

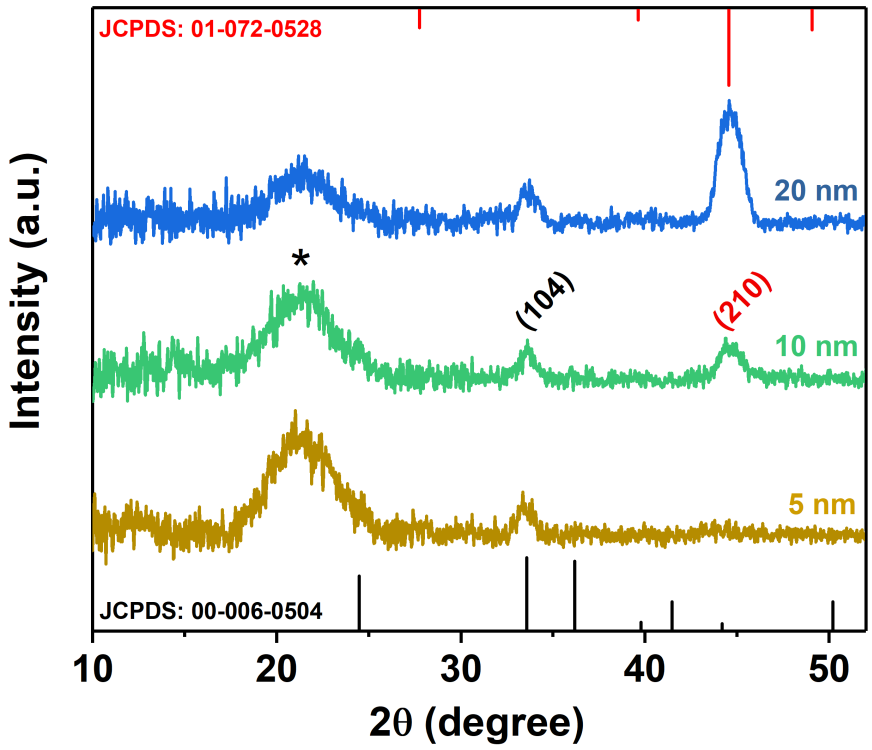

Figure 4.2: GIAXRD patterns of annealed chromium layers on Si/SiO_2 substrates, with corresponding stick patterns of Cr_2O_3 (black) and Cr_3O (red), respectively. The star symbol ($\star$) indicates the amorphous SiO_2 peak "from [1]".

The Cr layer was directly exposed to an annealing process (450 °C for 1 h in ambient condition) to ensure the same conditions that have been applied to the complete seed layer, including the evaporated MoO_3 layer on top of the Cr layer. The obtained XRD pattern revealed that the coated metallic Cr was converted to chromium oxides consisting of the two most stable chromium oxides phases: Rhombohedral Cr_2O_3 and cubic Cr_3O.

Oxidation of the Cr layer can be attributed to the interaction of the layer with the oxygen-rich substrate on the bottom, as well as to the formation of a metal oxide layer from the top during the annealing process [98]. The stoichiometry changed in favor of Cr_3O in thicker adhesive layers (10 and 20 nm), indicated by the increasing intensity of the (210) reflex at 44.55° as a predominant peak of Cr_3O (space group $Pm3n$, JCPDS 01-072-0528). An earlier study has shown that this phase of Cr oxide is formed from the interaction between Cr_2O_3 and metallic Cr [99]. In case of thinner layers (5 nm) Cr_3O cannot be detected. Cr_2O_3 was indicated by the (104) reflex at 33.58° (space group $R3c$, JCPDS 00-006-0504). This result is consistent with previous studies, which indicate the conversion of the Cr to its oxides by applying heat treatment and/or exposure to an oxygen–rich atmosphere [100, 101]. The broad peak observed in all films and centered at 21.4° (indicated by $\star$) is attributed to the amorphous SiO_2 substrate (JCPDS 01-086-1561) [102].

It was demonstrated that the chromium layer forms very strong chemical bonds to the oxidized substrate (SiO_2, FTO) *via* an oxide transition layer [102, 103]. Findings regarding the Cr layer by Benjamin *et al.* are worth mentioning: The adhesion on glass substrates is increasing with the exposure time to ambient condition. It is generally offers a better adhesion compared to noble metals, which is strongly depending on the deposition conditions and exposure to air [104, 105].

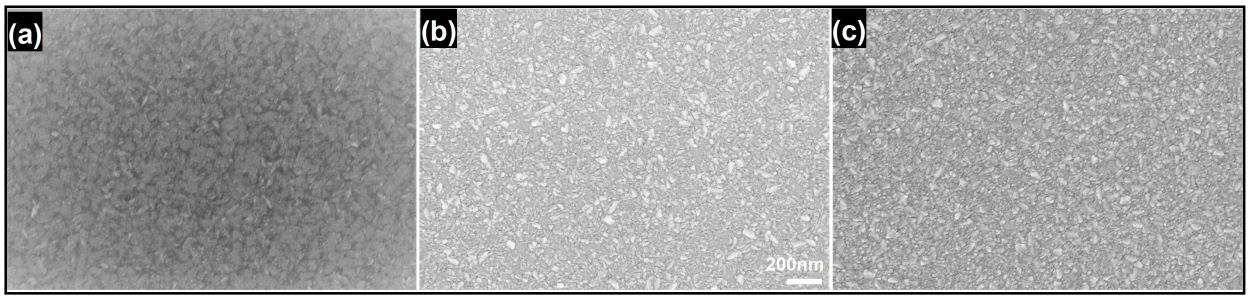

Figure 4.3: FE-SEM micrographs of evaporated and treated Cr layers with a thickness of (a) 5 nm, (b) 10 nm, and (c) 20 nm "from [1]".

The thickness of the Cr oxide layer was found to be influenced by the temperature during oxygen exposure, and it saturates at 400 °C [100]. Furthermore, prior studies [98] have shown that using Cr as an adhesion layer for Au/dielectric and semiconductor materials on glass and oxidized substrates decreased the roughness of the Au layer, which leads to smaller and more stable nucleation centers. Best adhesion was reported for thicknesses between 1 and 30 nm. Thicker films up to 100 nm lead to stress, which causes delamination [106]. In case of the study by Benjamin *et al.* the Cr layer was composed of closely spaced islands with a width of 5 nm and a height of 10 nm [104]. We observe similar structures as we can see in Fig. 4.3.

Therefore, we suggest that beyond acting as an adhesion layer, the Cr oxide could also functionalize as nucleation centers. The atomic radii of Cr and Mo are similar, which allows the adhesion layer to reduce the lattice mismatch between α-MoO_3 and the substrate. The effect can be quantified by comparing the lattice misfit (f) between the exposed lattice planes according to XRD calculated through the relation [107]:

$$f = \frac{(a-b)}{b} \cdot 100\,\% \tag{4.1}$$

where a and b are in-plane lattice parameters (preferred orientation) of the deposited layer and substrate, respectively. The corresponding values are given in Table 4.1 for deposited layers on FTO and Si/SiO_2 substrates.

Table 4.1: Lattice parameters of the substrates and the formed adhesive layer of Cr oxides for the calculation of the lattice mismatch.

Material	a (Å)	b (Å)	c (Å)	Ref. Card
FTO (substrate)	4.737	4.737	3.186	00-770447
Si/SiO (substrate)	5.082	5.082	7.095	01-086-1561
Cr_2O_3	4.958	4.958	13.593	00-006-0504
Cr_3O	4.544	4.544	4.544	01-072-0528

The calculation of the misfit between the layers reveals that MoO_3/FTO have 16 % misfit, MoO_3/SiO_2 have 21 %, Cr_2O_3/FTO have only 6 %, Cr_2O_3/SiO_2 have as little as 1 %, Cr_3O/FTO have 4 %, and Cr_3O/SiO_2 have 9 %. These observations are in line with previous studies and form a compelling argument for the use of a Cr adhesion layer for fast growth of the MoO_3 nanoblades.

In the next step, MoO_3 seed layers of different thickness (40 nm and 100 nm, respectively)

were directly deposited onto the Cr layer, followed by annealing at 450 °C for 1 h. As can be seen in Fig. 4.4, this leads to the formation of pure α-MoO_3 [108], which has also been confirmed by X-ray diffraction (Fig. 4.5 (a), JCPDS – 005-0508) [86]. A thickness of 100 nm was found to be optimal to partially uniformly cover the substrate, which was directly reflected in the density of MoO_3 nanoblades growth.

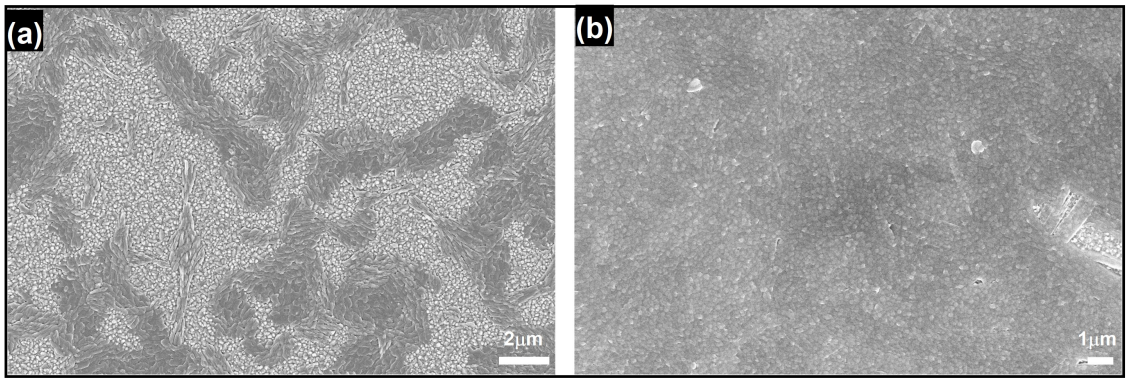

Figure 4.4: FE-SEM micrographs of (a) 40 nm and (b) 100 nm thick evaporated MoO_3 seed layers on FTO substrates "from [1]".

4.2.2 Vertically aligned direct growth of MoO_3 on the substrates *via* hydrothermal method

Vertically aligned MoO_3 nanoblades were grown directly on the pre-treated seeded substrates under hydrothermal conditions using sodium molybdate as a precursor under strongly acidic conditions. The effect of growth temperature and time on the MoO_3 structure was systematically analyzed by FE-SEM at different growth temperatures between 100 – 200 °C and reaction times between 60 – 210 min.

Prior studies have established that under strongly acidic conditions $[MoO_4]^{2-}$ ions condensate into hydrated MoO_3 *via* several polymolybdate intermediates [109]. At elevated pressure and a temperature > 100 °C the product loses water of crystallization to form α-MoO_3 as per Eq. 4.2:

$$\begin{aligned}[MoO_4]^{2-} \xrightarrow{\text{pH}\,6} [Mo_7O_{24}]^{6-} \xrightarrow{\text{pH}\,1.5-2.9} [Mo_8O_{16}]^{4-} \xrightarrow{\text{pH}<1} MoO_3 \cdot 2\,H_2O \\ \xrightarrow{\triangle} MoO_3 \cdot H_2O \xrightarrow{\triangle} \alpha\text{-}MoO_3\end{aligned} \tag{4.2}$$

With an optimum precursor concentration and a temperature of 180 °C, the reaction results in a dense array of aligned MoO_3 nanostructures after 3 h, as shown in Fig. 4.5 (b).

The XRD analysis of the nanoblades demonstrates that they crystallize in the α-MoO_3 phase. No reflexes of any other phase, impurity or inter-diffusion from the Cr layer could be detected (see Fig. 4.5 (a)). The sharp reflexes in the diffractogram indicate that the nanoblades are highly crystalline. (For the analogous reaction on Si/SiO_2 substrates see Fig. 4.6.)

The XRD pattern was found to have a preferred orientation favoring the (021) planes, which reflects the single crystalline growth along the [001] axis, in a good agreement with previously reported studies [38, 110]. The cross-sectional FE-SEM image (Fig. 4.5 (c)) confirmed the vertical

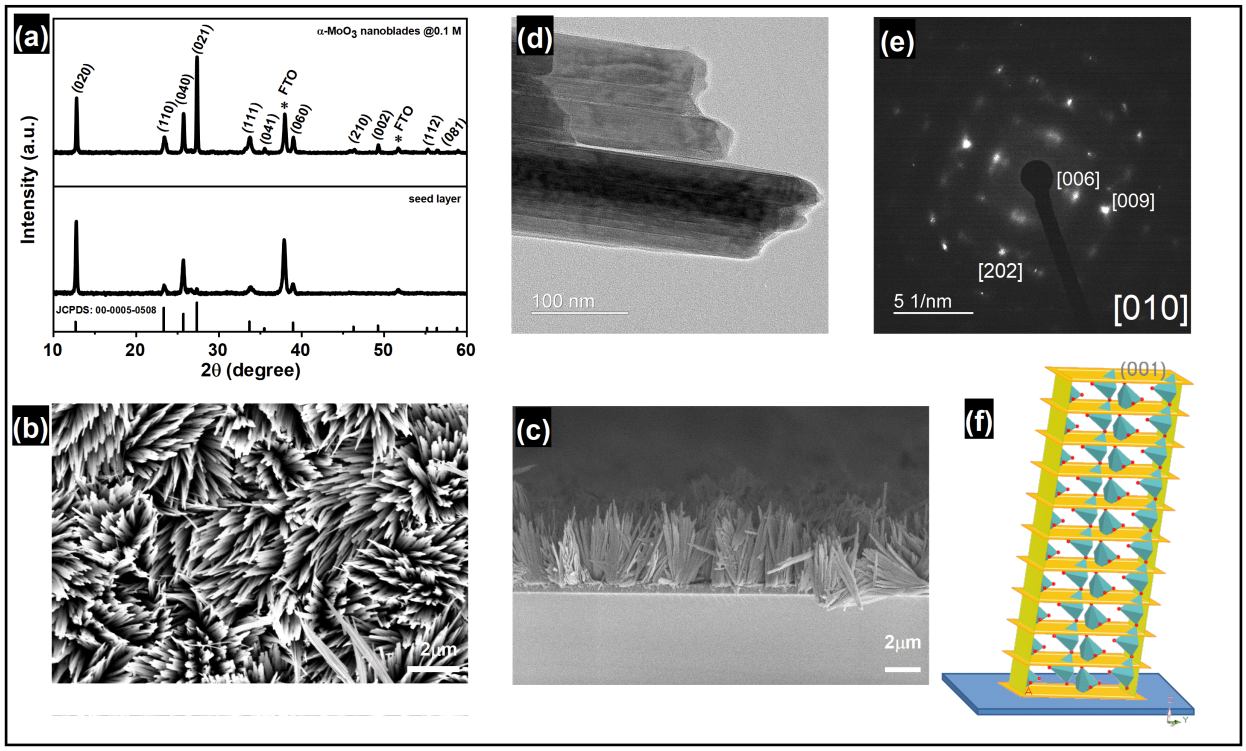

Figure 4.5: (a) XRD spectra of the annealed seed layer and vertically aligned α-MoO_3 nanoblades on FTO substrates. (b-c) FE-SEM images of vertically aligned α-MoO_3 nanoblades. (d-e) HR-TEM-SAED of α-MoO_3 nanoblades. (f) Schematic of MoO_3 nanoblades growth planes on the substrate "from [1]".

growth of MoO_3 nanostructures and arrangement in rows and bundles with a flower-like structure. No by-products from precursor decomposition appeared as shown in EDX (see Fig. 4.6 (e)).

Raman spectra [2]confirmed that the material is pure, stoichiometric α-MoO_3, as can be seen in Fig. 4.7.

The individual nanoblades are $\approx 10-50$ nm wide, as shown by HR-TEM (Fig. 4.5(d)), and they consist of fragile 2D sheets that do not stack onto each other, as can be seen in Fig. 4.8.

[2]Raman spectra were recorded by Dr. Peyman Zirak Yousefabadi, analyzed and written by me.

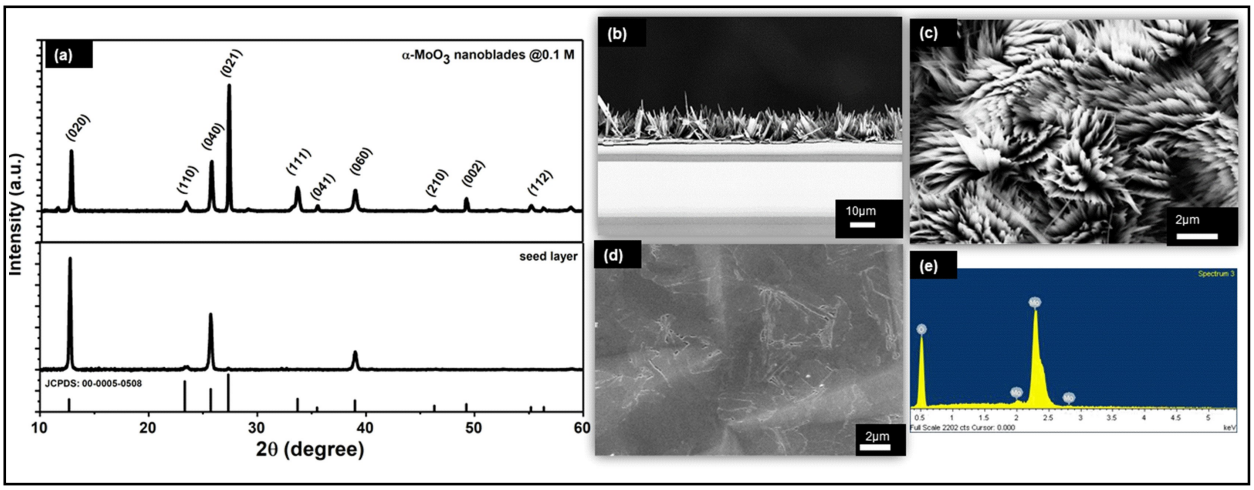

Figure 4.6: (a) XRD patterns of seed layer and vertically aligned α-MoO_3 nanoblades on Si/SiO_2 substrate. FE-SEM images of (b) seed layer, (c) cross-section, (d) top view of vertically aligned α-MoO_3 nanoblades on Si/SiO_2 substrate, and (e) EDX elemental peaks of the vertically aligned α-MoO_3 nanoblades "from [1]".

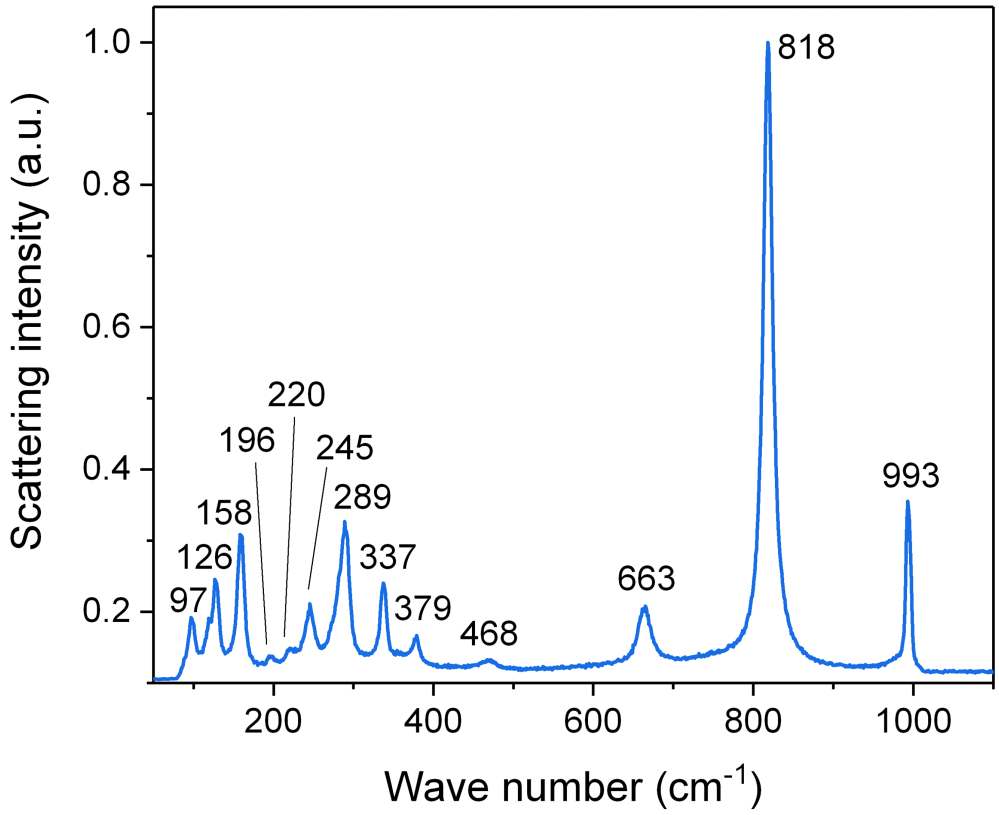

Figure 4.7: Raman spectra for the vertically aligned α-MoO_3 nanoblades on the substrate "from [1]".

Selected area electron diffraction (SAED, Fig. 4.5(e)) recorded perpendicular to the growth axis of the blades is attributed to the [010] zone axis, which supports preferential growth along the [001] direction as shown in Fig. 4.5 (f). The anisotropic crystal growth ties well with previous studies for well-ordered MoO_3 layers prepared on substrates [17,111]. It suggests that the nanoblade formation occurs *via* a direct precipitation reaction of highly anisotropic α-MoO_3 [112]. The nanoblades grow linearly with reaction time until the precursor is fully consumed or the reaction is interrupted by rapid cooling, as shown in Fig. 4.9.

It is worth mentioning that increasing the hydrothermal reaction time results in overgrowth of the fine structure. This can be seen in Fig. 4.10.

In addition, we observe weak adhesion in these overgrown samples, likely due to higher stress triggered by the increased film thickness. This constitutes a significant increase in reaction rate compared to previous studies on hydrothermal synthesis of MoO_3 nanorods and fibers, which give reaction times between 7 h and 7 days, respectively [10, 18, 109, 113–115]. In our study the growth time is significantly reduced – by a factor of 50 – for such 2D structures.

We propose that the increased growth rate is triggered by the introduction of our MoO_3 seed layer, which provides direct nucleation sites for the hierarchical structure growth. Therefore, no time for the primary formation of nucleation sites is required, allowing a direct initiation of the growth and reducing the growth times considerably (Fig. 4.9).

Another indication for this can be found by carefully looking at the backside of the seed layer (see Fig. 4.11). Their MoO_3 crystallites can be observed. Therefore, the nucleation has already occurred before the hydrothermal reaction.

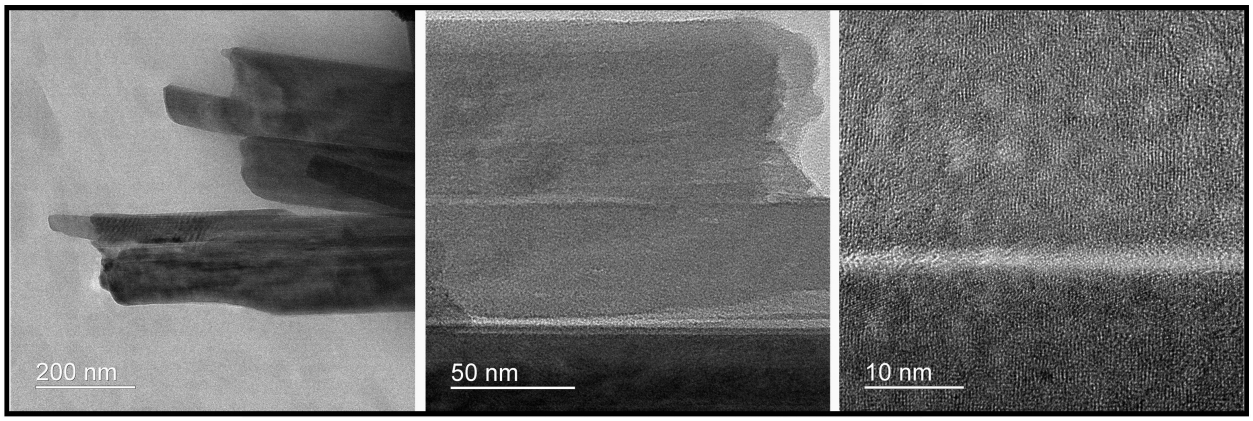

Figure 4.8: HR-TEM micrographs of the α-MoO_3 nanoblades "from [1]".

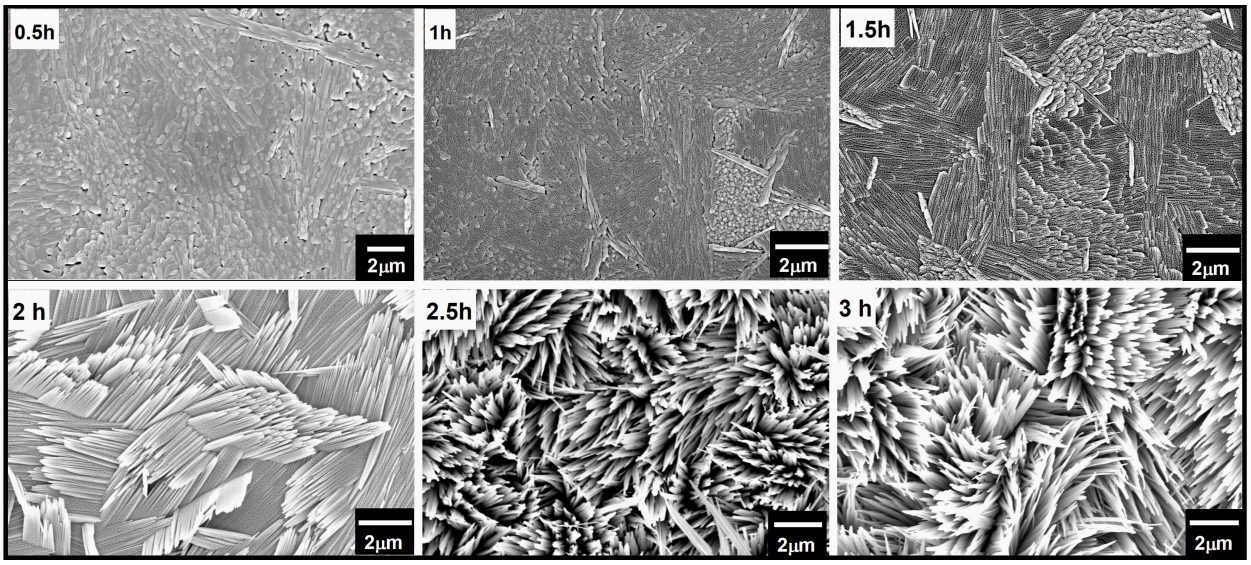

Figure 4.9: FE-SEM micrographs show the growth of vertically aligned α-MoO_3 on FTO at different times during the hydrothermal reaction using 0.3 mol/L acid concentration and a reaction temperature of 180 °C.

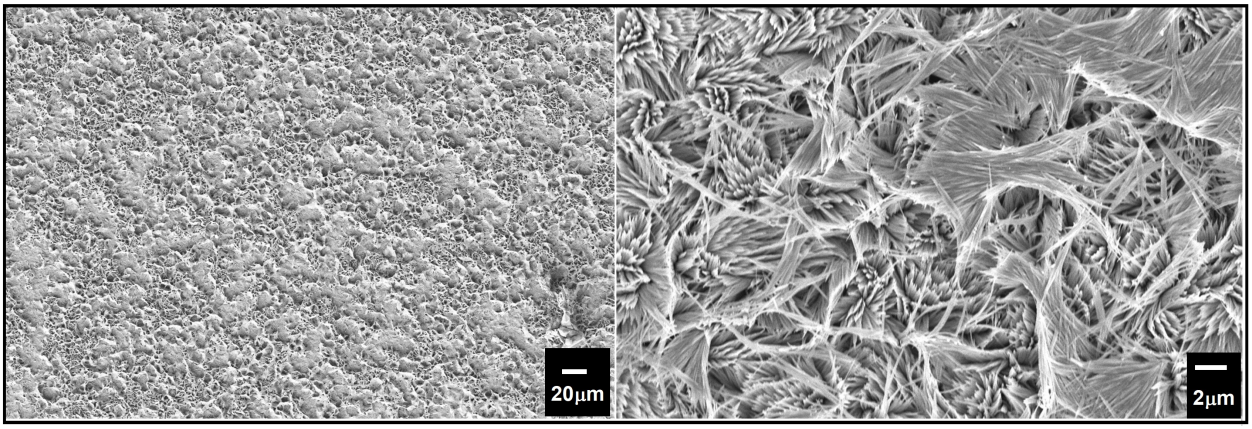

Figure 4.10: FE-SEM micrographs show the overgrowth of vertically aligned α-MoO_3 nanoblades due to an increased hydrothermal reaction time of 4 h (using an acid concentration of 0.3 mol/L) "from [1]".

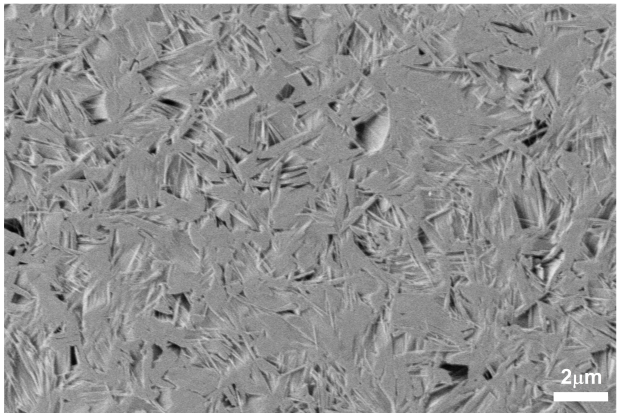

Figure 4.11: FE-SEM micrograph of backside of the vertically aligned α-MoO_3 nanoblades after removal from the substrate "from [1]".

4.3 Growth conditions and composition analysis

Hydrothermal synthesis depends on many factors that affect the morphology of the resulting nanostructure [116]. Acid concentration, precursor concentration, and reaction time were identified to have the most substantial impact on the immediate reaction. The rate at which the acid was added to the Na_2MoO_4 solution to form the reaction precursor was found to be crucial for the shape control of the resulting nanostructures. Slow addition with a rate of ∼1 drop per second yielded thin blades, while a faster rate led to the formation of hexagonal monoliths with a significantly reduced surface area.

This highlights the importance of precursor structure. The absolute amount of acid was used to control the length of the resulting nanoblades with different heights. The isopolymolybdate anions contain octahedral coordinated Mo(VI) ions that are connected *via* edges, as opposed to the tetrahedral coordinated MoO_4^{2-}, and thus form a fragment of the target structure.

By varying the HCl concentration from 0.06 mol/L to 0.85 mol/L, the length of the nanoblades could be increased from 3 to 11 μm using a seed layer of Cr/MoO_3 of 10/100 nm. FE-SEM micrographs are shown in Fig. 4.12 and Fig. 4.13, and the results are summarized in Table 4.2.

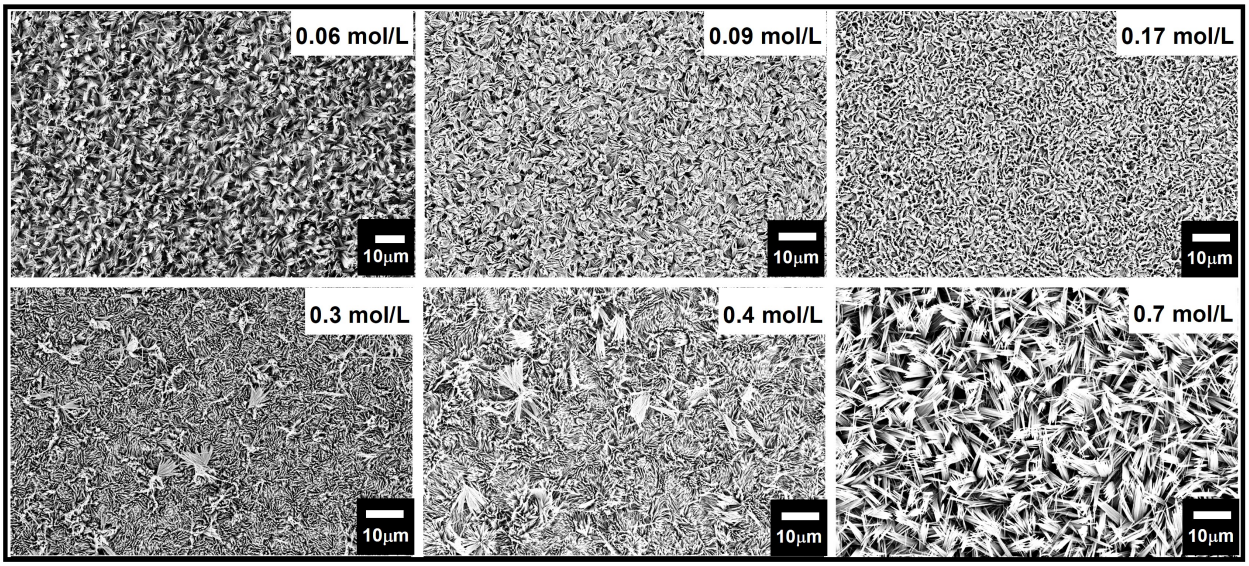

Figure 4.12: FE-SEM micrographs of vertically aligned α-MoO_3 nanoblades prepared by varying the acid molar concentration at a growth temperature of 180 °C on the seeded substrate of 10/100 nm of Cr/MoO_3 "from [1]".

Above a specific concentration of the $Na_2MoO_4 \cdot 2\,H_2O$ solution (between 0.02 mol/L and 0.3 mol/L, depending on the acid concentration), the blade-like shape of the nanostructures changed to larger crystallites with a hexagonal cross-section. Consequently, the crystal structure changed from α-MoO_3 to h-MoO_3 (JCPDS 00-065-0141), as can be observed in Fig. 4.14.

The hexagonal phase suffers from a significantly reduced surface area and poor adhesion to the substrates. In this case, we obtained a film thickness of 30 μm with a densely packed structure. Therefore, slow (dropwise) addition of the precursor was necessary to avoid formation of these larger crystallites.

The reaction temperature was found to have a minor effect on the morphology between 100 and 200 °C as shown in Fig. 4.15. This is in line with previous reports using in situ EXAFS [117].

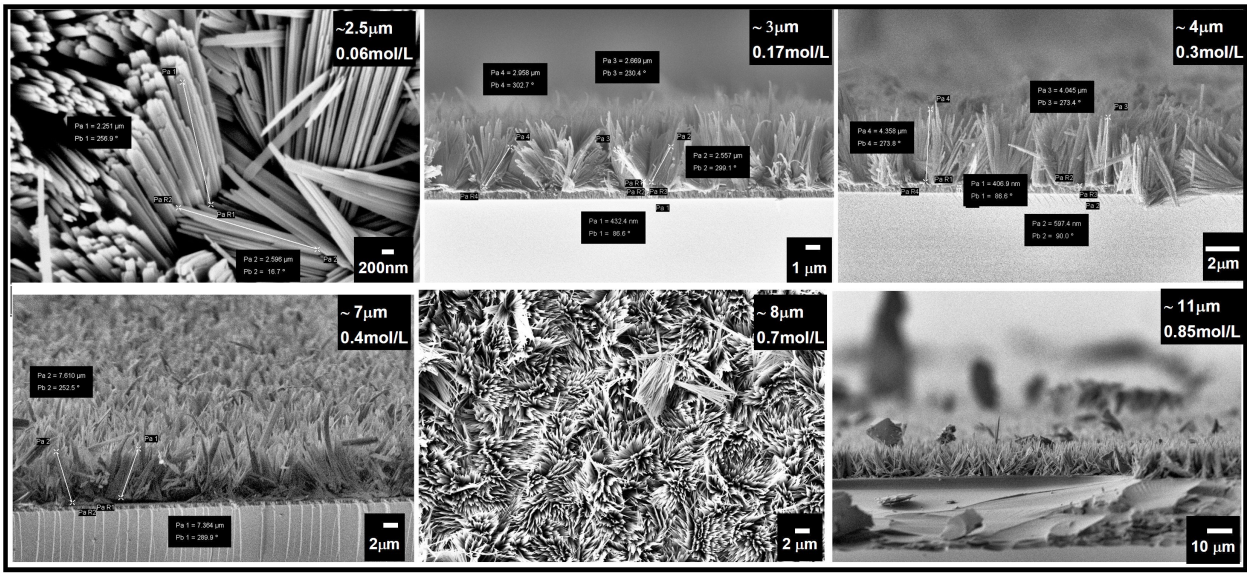

Figure 4.13: FE-SEM micrographs show the growth of vertically aligned α-MoO_3 nanoblades *via* different acid concentrations on a seed layer of 10/100 nm of Cr/MoO_3.

Table 4.2: Obtained vertically aligned α-MoO_3 nanoblade's length corresponding to the used acid concentration.

Acid concentration (mol/L)	Nanoblade's length (μm)
0.06	≈ 2.5
0.17	≈ 3
0.3	≈ 4
0.4	≈ 7
0.7	≈ 8
0.85	≈ 11

Hence, the formation of α-MoO_3 rods above a threshold of 100 °C was observed. The uniform length of the nanowires, and the flower-like shapes in which they are arranged on the substrate, lead to the conclusion that growth occurs exclusively from the seed particles orientation perpendicular to the substrate. This behavior is caused by the blades mutually pushing each other up when they start touching each other (Fig. 4.9).

While the conditions of the hydrothermal reaction can be tuned to reach optimal conditions for fast growth of MoO_3 films with a high surface area, the adhesion layer is crucial to accommodate a wide range of different substrates with significant variations in roughness. Rougher substrates (FTO) require the deposition of a thinner Cr layer in the range of 5 – 10 nm for the MoO_3 film to adhere to the substrate. On the other hand, smooth substrates (Si/SiO_2) require a 10 – 20 nm thick Cr layer to have better adhesion between the α-MoO_3 layer and the substrate.

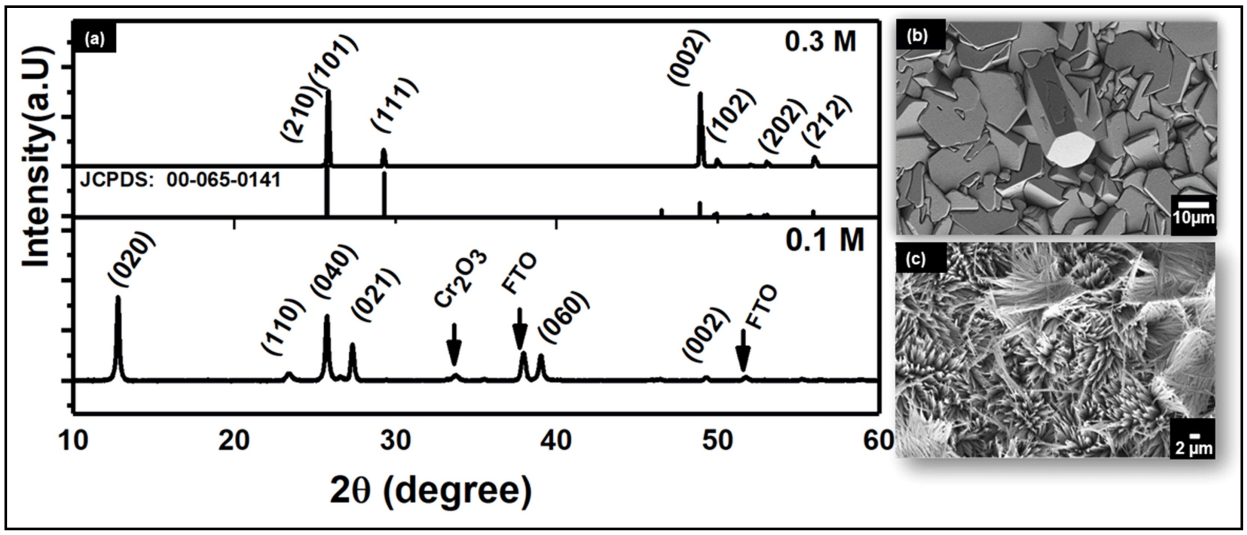

Figure 4.14: XRD patterns of MoO_3 nanostructures prepared at different molar concentrations at 180 °C using a seed layer of Cr/MoO_3 of 10/100 nm (a) 0.1 M and 0.3 M. FE-SEM images of MoO_3 nanostructures at different molar concentrations (b) 0.1 M and (c) 0.3 M "from [1]".

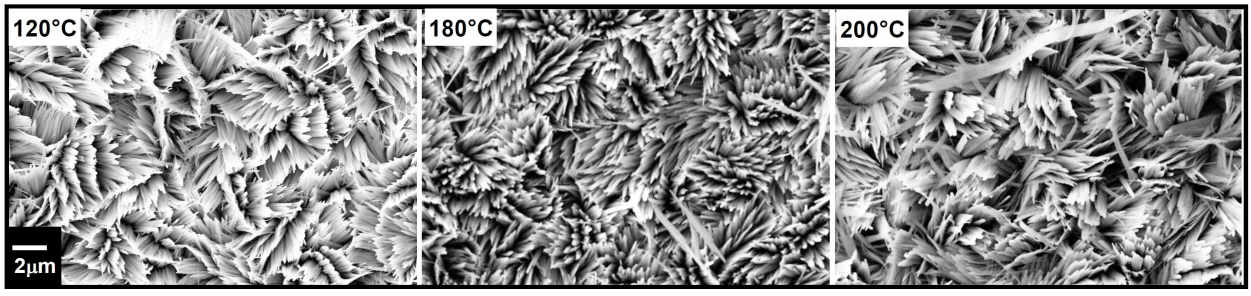

Figure 4.15: FE-SEM micrographs of vertically aligned α-MoO_3 nanoblades prepared at different hydrothermal reaction temperatures using an acid molar concentration of 0.3 mol/L and a seed layer of 10/100 nm of Cr/MoO_3 "from [1]".

4.4 Thermochromic effect and heat post treatment of α-MoO_3 under reducing and oxidizing atmospheres

4.4.1 Overview

Among versatile transition metal oxides, MoO_3 has chromogenic properties. As has been introduced in a previous chapter, the early study by Deb *et al.*, who devoted their attention to the chromogenic properties of MoO_3, revealed the ability to change the optical density by using external agents. Those external agents can be in three forms: Light, heat and electrical field. Subsequently, they lead to coloration effects that are known as photochromic [118, 119], thermochromic [55] and electrochromic effect [73], respectively.

This coloration effect reflects the effect of stoichiometry of MoO_{3-x}. As we showed in the previous chapter, MoO_3 can exist in different crystal structures as crystalline and amorphous (orthorhombic phase, and monoclinic phase), and it has a chromogenic property. Nevertheless, it is found that the chromogenic property is more strongly observed in the amorphous monoclinic structure than in crystalline phases.

Previous studies showed that MoO_3 films at room temperature in hydrogen rich atmosphere form molybdenum bronze [120], and this results in a decrease of the band gap by introducing gap states. Subsequently, changes in the work function can be observed due to exposure to such reducing atmospheres as well as to oxidizing atmospheres such as air [73].

In the present study, we tried to combine both effects, the thermochromic effect and the sensitivity to atmospheres, which are not intensively studied, to tune the electronic properties. As an attempt to address the role of the oxygen vacancies for altering the electronic-optical properties, the results have been compared and discussed with regard to previously reported theoretical studies.

As far as we know, no previous accurate report about lattice distortion mechanism and doping effect on MoO_3 have been established until the study by Ding *et al.* in 2014. Various van der Waals (vdW) corrected density function theories (DFT) have been applied to result in a decisive valuable study about lattice parameters, bond length and formation energies and deformation in MoO_3 [30]. Moreover, it was believed that α-MoO_3 is a p-type material until the last mentioned theoretical studies proved it as n-type material.

A critical open question is whether it is possible experimentally to yield accurate information about the positions of oxygen vacancies in the crystal, and the related electrical properties. Therefore, in this part of the present study, different oxidizing and reducing atmospheres were used during the thermal treatment applied to our vertically aligned α-MoO_3 nanoblades on FTO substrates.

4.4.2 Thermal treatment under reducing and oxidizing atmospheres

We mentioned before that, different acid molar concentration affects the length scale of the wires on the substrates (see Table 4.2). Now one scale length of 5 μm, corresponding to 0.3 mol/L acid concentration, has been used to anneal separately at high temperature of 450 °C under oxidizing atmosphere [O_2] and reducing common atmospheres [H_2, N_2 and vacuum] for 3 h. The resulting films can be seen in Fig. 4.16 at different magnifications.

It is worth to mention that, a further increase in the annealing temperature above 450 °C leads to a collapse and deformation in the nanoblades under nitrogen and vacuum conditions, as can be seen in Fig. 4.17.

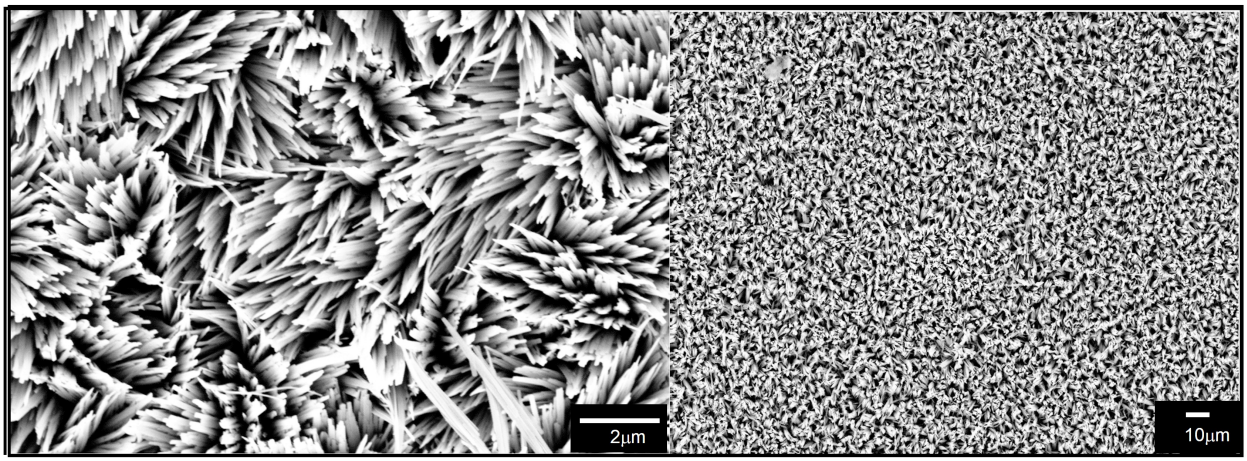

Figure 4.16: FE-SEM micrographs of vertically aligned α-MoO_3 nanoblades prepared using acid molar concentration of 0.3 mol/L and seed layer of 10/100 nm of Cr/MoO_3.

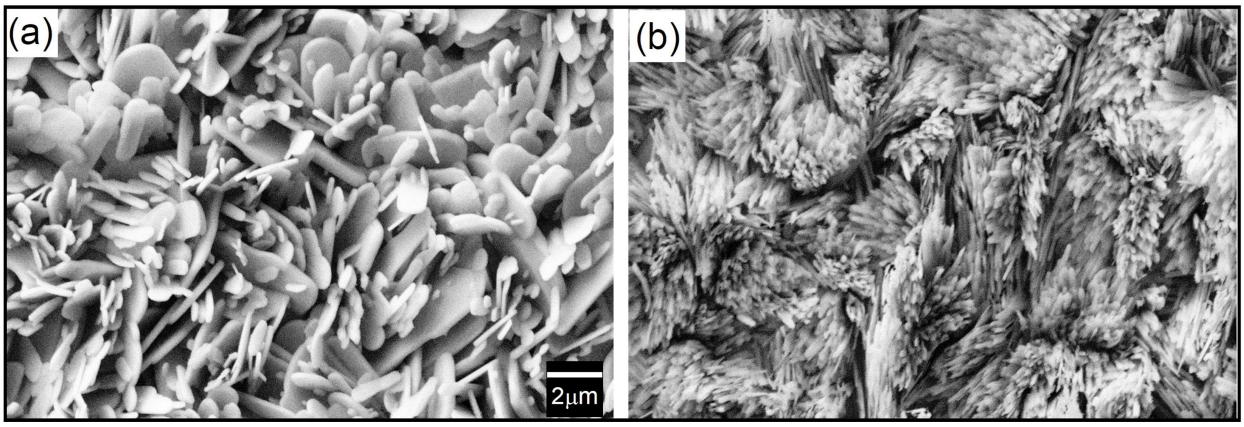

Figure 4.17: FE-SEM micrographs of vertically aligned α-MoO_3 nanoblades annealed under N_2 and vacuum conditions at 500 °C.

4.5 Structural and morphological analysis of reduced and oxidized α-MoO_3 films

Vertically aligned α-MoO_3 nanoblades on FTO substrates treated separately under different oxidizing and reducing atmospheres (such as O_2, H_2, vacuum, N_2) at 400 °C for 3 h have been characterized using different techniques as we can see in the following sections.

4.5.1 X-ray diffraction analysis

As initial stage, XRD patterns have been analyzed for the post-treated samples under oxidizing and reducing atmospheres such as O_2, H_2, N_2, and vacuum. Fig. 4.18 (a) shows diffraction patterns of vertically aligned α-MoO_3 nanoblades on FTO substrates separately annealed at 400 °C for 3 h under the aforementioned atmospheres.

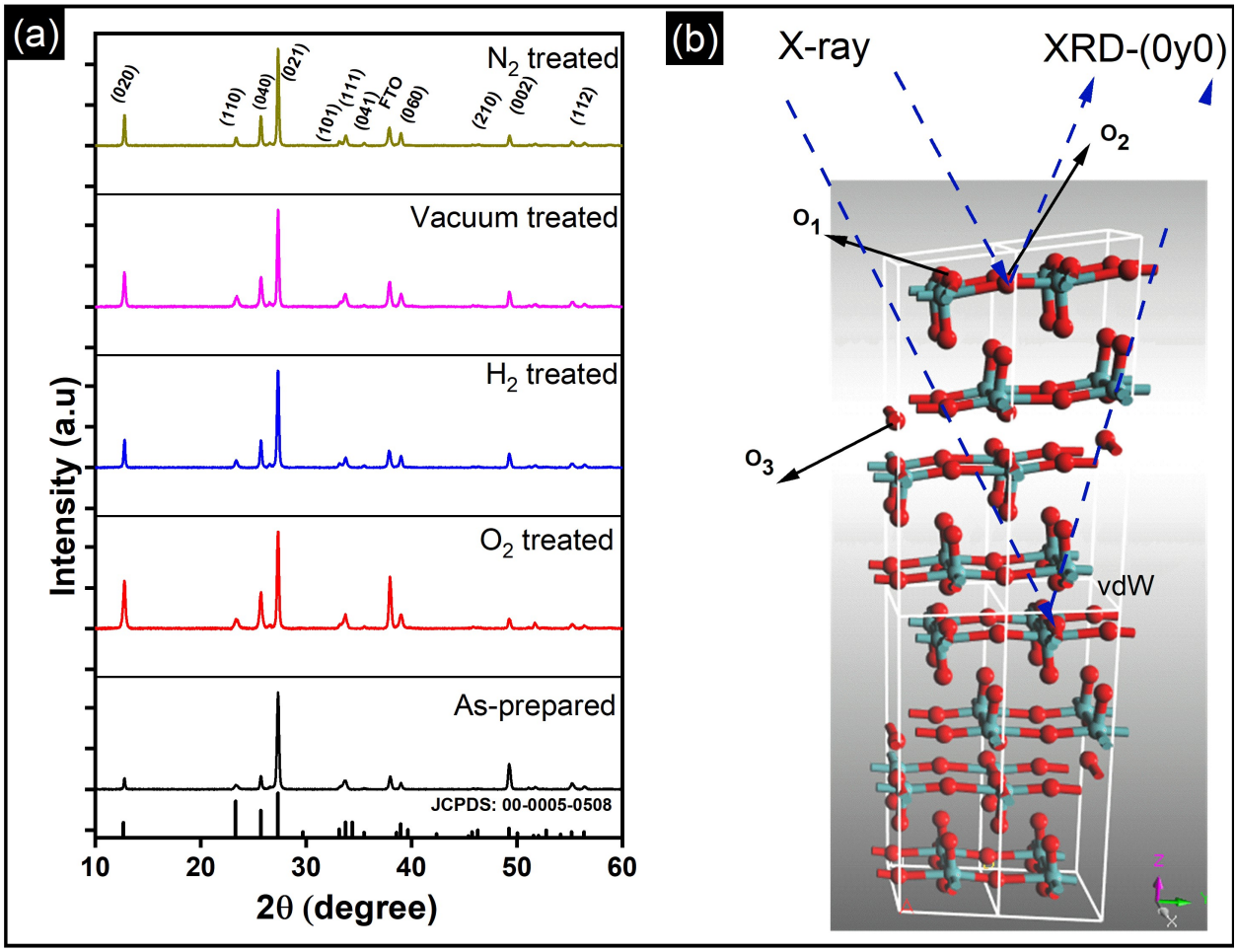

Figure 4.18: (a) X-ray diffraction patterns of vertically aligned α-MoO_3 on FTO substrates prepared by hydrothermal technique and post-treated substrates under different atmospheres at 400 °C for 3 h such as oxidizing (O_2), reducing (H_2, vacuum, N_2). (b) Illustration of the crystal structure of the vertically aligned α-MoO_3 nanoblades grown in z-direction with indication of the stacked layers *via* van der Waals (vdW) in y-plane and its oxygen atom positions in the crystal as O_1, O_2, O_3 in apical in the octahedral, edge-sharing and corner-sharing, respectively. The dashed blue lines illustrate the incident X-ray beam on the substrates on the direction of the vdW bonds.

The XRD patterns of α-MoO_3 nanoblades were found to be consistent with orthorhombic α-MoO_3 (JCPDS: 00-005-508, space group *Pbnm* and unit cell parameters $a = 13.86$ Å, $b = 3.70$ Å and $c = 3.96$ Å. For all conditions, the vertically aligned α-MoO_3 nanoblades diffraction patterns show highly crystalline nature without appearance of peak shifts in comparison to as-prepared films. However, upon closer observation, the peak intensities were found to be varied for all conditions after the treatment.

One of the major difficulties of structural characterization of thin films is the variation of the XRD peak's intensities, which is not intensively addressed in the literature. Whereas some researchers explain it as changes in the preferred growth directions, others explain it as defects in the crystal. Interestingly, in some cases, doping or defects in the crystal structure do not cause a shift the diffraction peak's position [121] but changes in the XRD pattern's intensity.

Basically, the variation in the intensities is found to be attributed to two factors: (1) The variation in the preferred orientation [122], and (2) the variation in stoichiometry and defects. Thus, the first factor can be changed due to the change in the film thickness or molar concentration of the liquid method synthesis (this cannot be changed in the present system) [121, 123–125]. This leads us to rely on the relative intensities. Hence, the relative intensity is a structural factor, which reflects the diffraction intensity by the content of one unit cell relative to the content of other unit cells, including electrons and defects such as vacancies or interstitial ions. (For more information see chapter 2 in [126].)

It is worth to mention here that, the relative intensity is an instrumental independent parameter [126]. The relative intensities of the diffraction peaks have been calculated by dividing the absolute intensity of every peak by the absolute intensity of the most intense peak, and then convert to a percentage where the predominant peak was set as 100 % [127, 128]. Based on this assumption, the relative intensities have been calculated separately for every condition. The results are listed in Table 4.3.

Table 4.3: XRD patterns relative intensities (RI %) calculated by considering the predominant peak as (100 %) relative to other peaks intensities for α-MoO_3, as-prepared and treated under O_2, H_2, vacuum, and N_2 conditions.

Plane	RI %				
	As-prepared	O_2	H_2	Vacuum	N_2
(021)	100	100	100	100	100
(020)	11	49	29	35	31
(110)	4	9	7	11	8
(040)	14	38	28	29	30
(111)	9	14	10	13	10
(060)	7	14	11	13	13
(002)	26	10	14	14	10

Initially, it was expected that under reducing atmospheres the oxygen vacancy concentration increases, which should result in a decreasing trend in the relative intensities. However, a more careful inspection revealed that the relative intensities in (0y0) planes increase. This reflects the increase in the number of scattering centers, which cause a more pronounced amplitude of the scattered intensity in that plane, and sustains that the vacancies in all cases are not introduced in the y-direction (O_1 lattice site; see Fig. 4.18). Whereas in the (002) plane, the relative intensities decrease in the z-direction (O_3 lattice site).

An increase in the number of scattering centers in y-direction is consistent with the conclusion given by Duo *et al.* that rearrangement and refilling of the vacancies spontaneously happens in the y-direction [129]. It reinforces the existence of the vacancies in (x,z) plane [129]. This result has further strengthened our observation of the high crystallinity nature under all conditions and emphasizes the validity of these results.

Additionally, according to vdW-DFT calculations by Inzani *et al.*, the oxygen vacancies in the O_1 and O_3 lattice sites cause less lattice distortion in comparison to the O_2 site where the highest lattice distortion can occur [130]. Furthermore, it lends supports to the DFT + revised Perdew-Burke-Ernzerhof (RPBE) approach calculations by R.Tokarz, which indicate that the O_1 site has the largest formation energy in comparison to other oxygen defects in the x- and z-plane [131]. This implies that the oxygen vacancies in the O_2 and O_3 sites allow polaron migration and replenishment

of vacancies in the y-lattice planes.

In spite of being in good agreement with previously reported theoretical studies, a further investigation using SAED has been employed to find out whether dislocation and deformations in the diffracted lattice points (corresponding to d-space) in x- and z-planes can be detected.

4.5.2 High resolution transmission electron microscope analysis

[3]To assess our observation and assumptions obtained from XRD analysis, high resolution transition electron microscope (HR-TEM) micrographs and selected area electron diffraction (SAED) patterns have been examined. These can be seen in the Figures 4.19, 4.20, and 4.21.

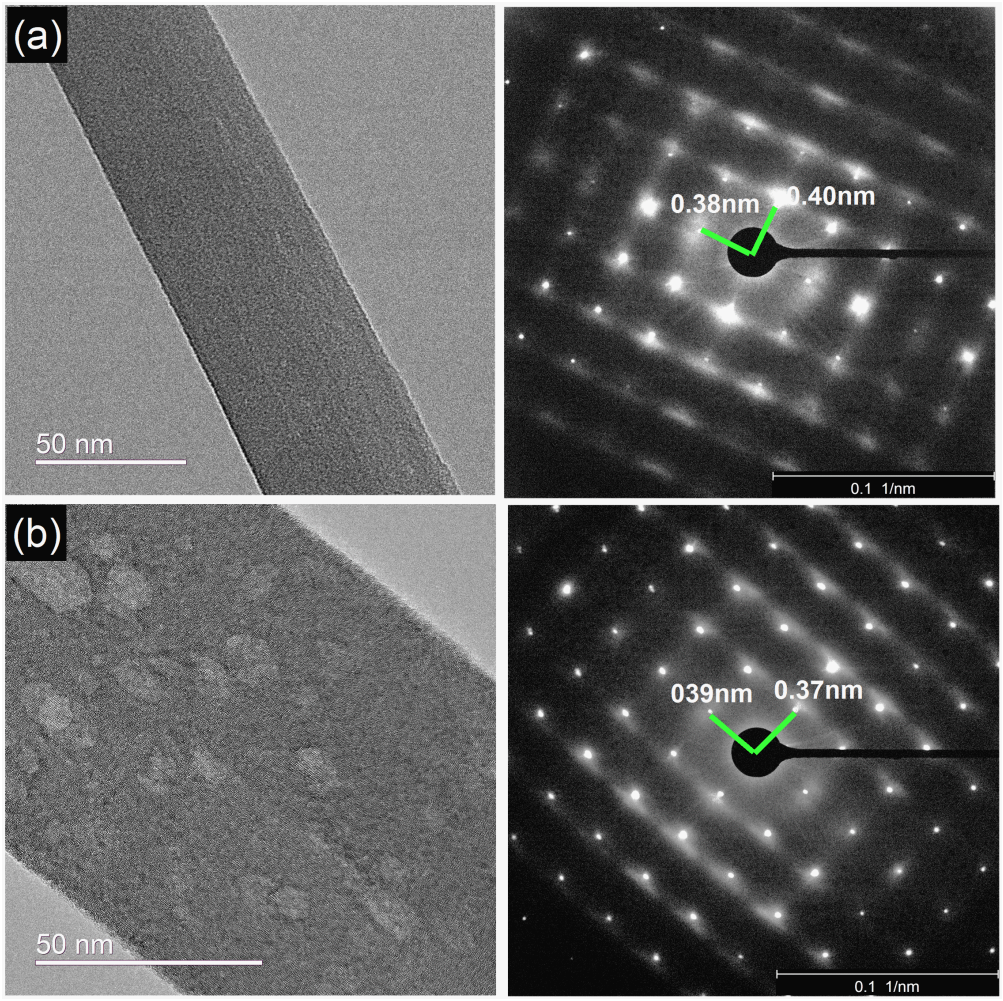

Figure 4.19: (a) HR-TEM micrograph and SAED patterns of as-prepared α-MoO_3 nanoblade with the measured d-spacing in x-y-planes. (b) HR-TEM micrograph and SAED patterns of α-MoO_3 nanoblade treated under oxygen rich atmosphere with the measured d-spacing in x-y-planes.

Interestingly, the shape of the nanoblades appeared to have random spots of lower contrast after the heat treatment for all conditions, which might be due to the influence of heat on the very

[3]HR-TEM micrographs were recorded by Dr. Marina Krumova, analyzed and written by me.

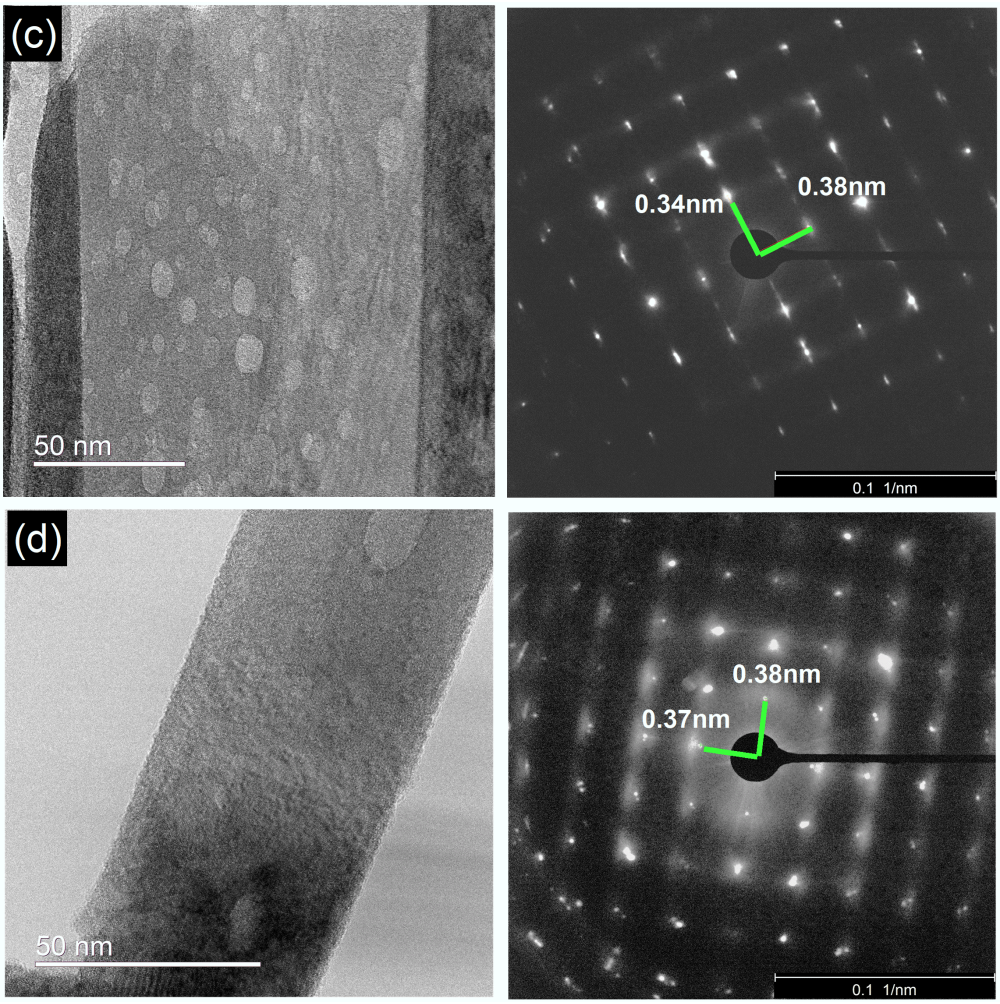

Figure 4.20: (c) HR-TEM micrograph and SAED patterns of α-MoO_3 nanoblade treated under H_2 atmosphere with the measured d-spacing in x-y-planes. (d) HR-TEM micrograph and SAED patterns of α-MoO_3 nanoblade treated under vacuum with the measured d-spacing in x-y-planes.

thin nanoblades. Overall, the SAED patterns indicated no deviation from crystallinity, as has been confirmed by XRD peaks.

Additionally as shown in the SAED pattern in Fig. 4.5-(e), the diffraction patterns reflect the zone axis of [x0z]. This allows us to obtain the inter-planar spacing (d-spacing) in those planes. The d-spacing has been carefully calculated (d = 2 / reciprocal lattice). As we can see in the Figures 4.19, 4.20 and 4.21, the d-spacing of the (x,z) plane has been evaluated, and the results are shown in Table 4.4.

The d-spacing values are found to be identical for all conditions in one direction, and the resulting values are in good agreement with the standard lattice constant $a = 0.396$ nm that corresponds to the x-direction.

As has been predicted, d-spacing values are not identical for all conditions in the other direction, which is suggested to be the z-direction (lattice constant $c = 0.369$ nm). The best match of the d-spacing with the standard value of the z-direction is found for nanoblades treated under oxygen rich atmosphere. This condition tends to produce highly defect-free nanoblades, which can be

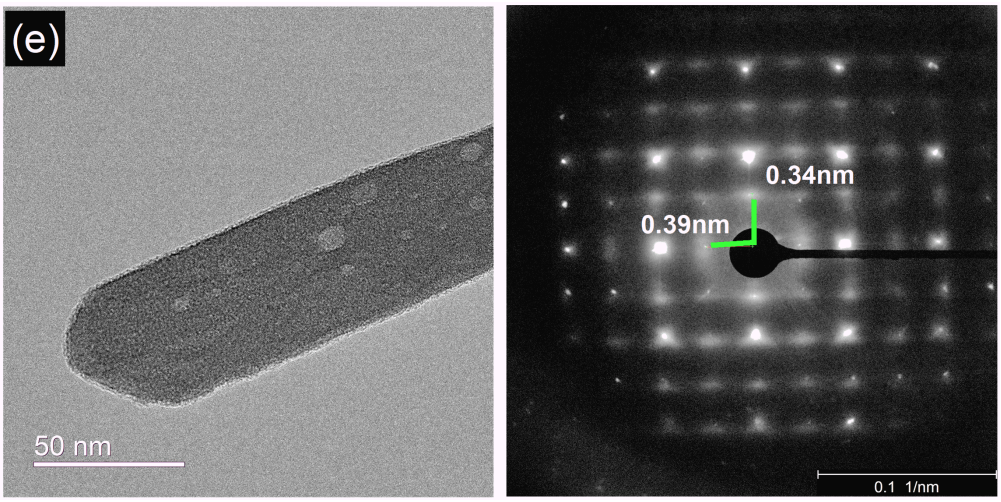

Figure 4.21: (e) HR-TEM micrograph and SAED patterns of α-MoO_3 nanoblade treated under N_2 atmosphere with the measured d-spacing in x-y-planes.

Table 4.4: Values for the d-spacing obtained from SAED patterns of α-MoO_3, as-prepared and treated under O_2, H_2, vacuum, and N_2 conditions.

Samples	d-spacing (nm)	d-spacing (nm)
As-prepared	0.38	0.40
O_2	0.37	0.39
H_2	0.34	0.38
Vacuum	0.37	0.38
N_2	0.34	0.39

found as a residual from the synthesis procedure. This can be understood from the value obtained in the as-prepared nanoblades.

As the nanoblades are reduced, the d-spacing deviates from its standard value. A smaller deviation is found for vacuum treated samples, and the highest deviations are found in the case of H_2 and N_2 treated samples. The data evaluation can be understood through different approaches:

- The results support the notion given by modified color center formation (2.6.4), that oxygen vacancies were introduced in the crystal. The formation of oxygen vacancies according to vdW-DFT calculations in the z-plane and in the x-plane lead to less perturbation in the positions of Mo ions toward the closest O ion and do not exceed ≈ 0.2 Å, which ties well with our results [30].
- However, we can still verify that in H_2 and N_2 annealed samples, a substitution of the oxygen ion with the adsorbed H^+ and N^- ions is favorable to occur, which can be assumed as external doping (defect), respectively. The substitution of an oxygen atom (atomic radius 0.48 Å [132]) with the bigger hydrogen and nitrogen ions (atomic radii of 0.53 and 0.56 Å, respectively) can cause additional shrinking of the d-spacing.
- The variation in the relative intensities of XRD peaks reflects the scattering intensity by the electron density that is periodically distributed in the crystal lattice (intensity is proportional to the total number of core electrons) [126]. Oxygen has 8 electrons, whereas hydrogen and nitrogen have only 1 and 7 electrons, respectively. Substitution of oxygen with hydrogen and nitrogen could explain the reduced relative intensities of XRD peaks in z-direction.

5. Spectroscopical Characterization

5.1 Overview

As we already discussed about metal oxides in general and MoO_3 specifically, oxygen vacancies are the intrinsic defects that play a major role in the material properties. It was an interesting comparison made by Prof. Pacchioni in his research [133] that the oxygen vacancies can be considered as reminiscent of a series named "Invisible Agent" which was a well-known movie in 1942. Hence, for a long time the visualization of the oxygen vacancies was unfeasible, even though the knowledge about them is very rich in previous early studies. This was until the first observation of the oxygen vacancies migration on TiO_2 surface was made by Prof. Flemming and his team using atomically resolved scanning tunneling microscopy (STM) [134].

The interest of modern material science has been increasing continuously in the direction of defect engineering. Defect engineering broadens the ability of manipulating the material properties in a desired manner to produce more precise and well oriented applications to fit our needs as a human being.

In this chapter we will introduce common spectroscopic characterization techniques for further investigation of the crystal oxygen vacancies in α-MoO_3 nanoblades and their impact on the optical properties.

5.2 Electron paramagnetic resonance analysis

Electron paramagnetic resonance (EPR) [1] is a sensitive tool for investigation of shear structures, point defects, reduced ions, oxygen radical species, and color centers even in very low concentration [5].

Fig. 5.1 (a) shows the continuous wave (CW) EPR spectra recorded at 80 K of untreated α-MoO_3 nanoblades, and the treated α-MoO_3 nanoblades under oxidizing and reducing atmospheres. The signal intensity is plotted as a function of the g-values. This allows for a direct comparison of the EPR spectra irrespective of slight variations of the microwave frequency from one measurement to the other. The g-values have been calculated according to the following equation [135]:

$$g = \frac{(h\nu)_B}{\mu_B B_0} \tag{5.1}$$

where $(h\nu)_B$ is the microwave energy, μ_B is the Bohr magneton, and B_0 is the applied magnetic field.

[1] This part was written and analyzed by Dr.Mykhailo Azarkh and me.

EPR transitions appear at the g-values typical for α-MoO_3. The broad signals at around $g = 1.94$ are attributed to Mo^{5+} species [6, 136]. The hyperfine coupling owing to isotopes with $I = 5/2$ is not resolved. (The natural abundance for ^{95}Mo and ^{97}Mo is 15.92 % and 9.55 %, respectively [137, 138].) The EPR signals are significantly broader than expected for individual Mo^{5+} species, which can be an indication of the reduction degree [5, 6].

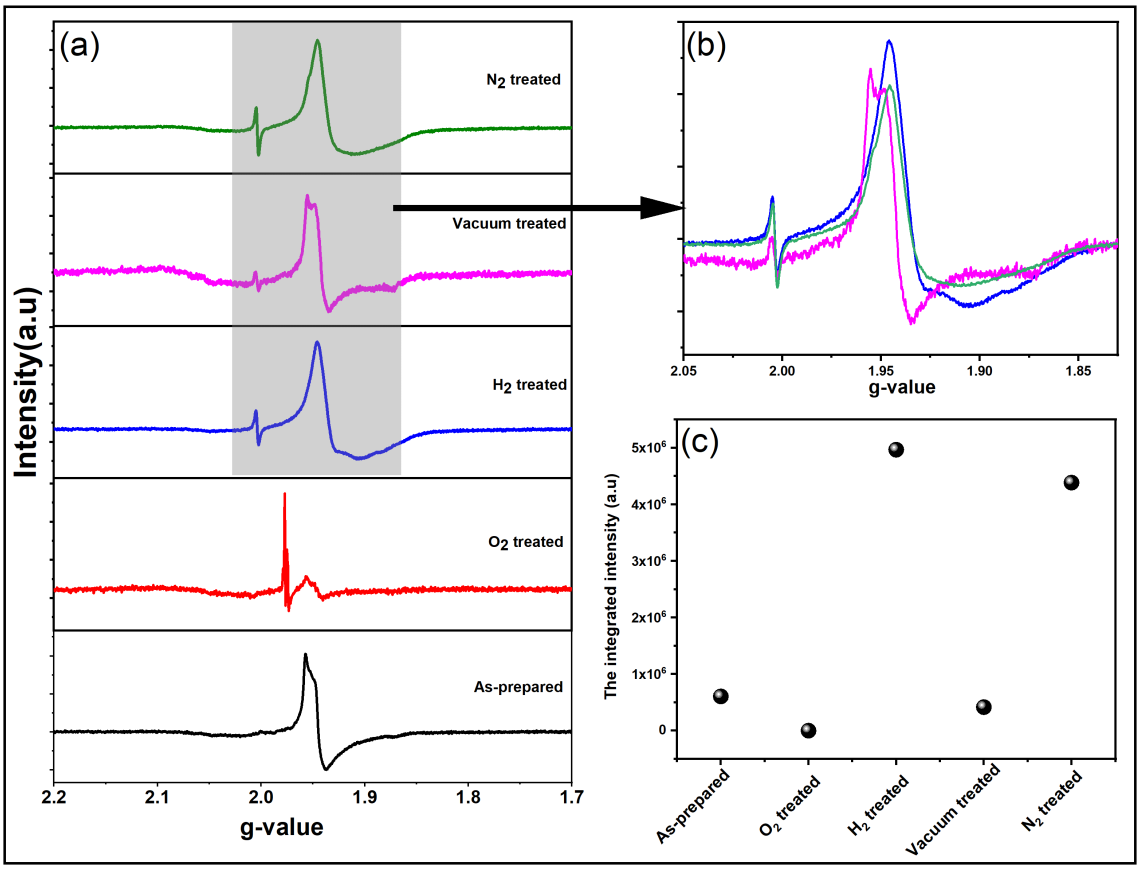

Figure 5.1: EPR spectra of as-prepared α-MoO_3 nanoblades and of nanoblades treated under O_2, H_2, vacuum and N_2 atmospheres.

The integrated intensity normalized to the sample weight is found to be the largest for H_2 and N_2. It is smaller by a factor of 10 for as-prepared and vacuum treated, and almost zero for O_2 treated nanoblades as can be seen in Fig. 5.1 (c). The integrated intensity of these EPR spectra reflects the number of Mo^{5+} ions in the nanoblades. The broadening of the peaks in Fig. 5.1 (a) suggest that the peaks consist of several overlapping signals, which is in line with previously reported studies [5, 6, 136, 139, 140]. The lower values of the absorption g-tensor around 2.003, which were detected in reduced samples (H_2, vacuum, N_2), can be ascribed to single ionized oxygen vacancies $O^{\bullet -}$ (radical oxygen) [140], see Fig. 5.1 (b).

In oxidized α-MoO_3 nanoblades, a low-intensity signal has been recorded, which is at the same position as the original signal of α-MoO_3. This signal can be attributed to a very low concentration of Mo^{5+} ions and the existence of F-centers ($F^{\star}$) as discussed in Section 2.6.1.

The shape of the spectrum for vacuum treated nanoblades indicates the asymmetrical line of

a local crystal field of nonaxial symmetry with very clear hyperfine structure, which is in good agreement with previous studies [5, 6, 136, 137]. However, in N_2 treated samples the hyperfine structure cannot be obtained. The H_2 treated sample shows the same broadening as the N_2 treated ones with a hyperfine structure related to g-tensors, which ties well with previous results of the H^+ effect on the MoO_6 octahedral structure [136].

For as-prepared and reduced α-MoO_3 nanoblades, g-tensors around 1.956 and 1.946, respectively, reflect Mo^{+5} species that can be explained by structural changes [139]. Various previous EPR studies of Mo^{+5} species showed that signals are assigned to hexacoordinated Mo(V) centers in shear defects caused by an off-center shift of Mo atoms toward surrounding oxygen [6, 141, 141], whereas those results lead to a rearrangement of the vacancies from corners to edge sharing (x- to z-) planes, as we found from XRD patterns decreasing in relative intensity in the z-plane. Additionally, the spin Hamiltonian function, which has been given by K. Dyrek *et al.*, indicates weakening of the octahedral crystal field around Mo^{+5}, which confirms strong lattice distortion in that plane [6].

Atomic hydrogen H^+ has been found to occupy anionic sites resulting in Mo^{+5} as $(MoO_6)^{-7}$ cluster of octahedral Mo^{+5}, wherein N^- accepts one electron (N^- not paramagnetic active impurities) from the oxygen and allows to detect the stabilized radical $O^{\bullet -}$ in the shear structure along the x- and z-planes [5, 137]. The lower intensity of the vacuum treated nanoblades spectrum confirms the lower concentration of free radical ions, which can lead to different conductivity between the reduced atmospheres themselves as will be described later in chapter 6.

For oxidized α-MoO_3 nanoblades, the EPR signal for the radical O^{2-} stabilized in Mo^{+6} was not detected in our case, which suggests the higher stability of our structure (ex-situ nanoblades).

We have verified that using XRD and EPR, oxygen vacancies have been eliminated from corner to edge-sharing α-MoO_3 nanoblades. A quantity of Mo^{5+} ions in each sample was determined from the comparison with the EPR intensity of a standard $CuSO_4$ sample as an indication of substoichiometric effects. Under the assumption that only Mo^{5+} species contribute to the EPR intensity and that there is an oxygen vacancy corresponding to each Mo^{5+} ion, the deficiency concentrations have been given in Table 5.1.

Table 5.1: The estimated stoichiometry evaluation of as-prepared α-MoO_3 nanoblades, and of nanoblades treated under oxidizing (O_2) or reducing atmospheres (H_2, vacuum, N_2) using EPR.

Sample	Stoichiometry
As-prepared	$MoO_{2.994}$
O_2 treated	$MoO_{3.000}$
H_2 treated	$MoO_{2.951}$
Vacuum treated	$MoO_{2.996}$
N_2 treated	$MoO_{2.957}$

In order to identify the paramagnetic species/defects in the oxidized and reduced α-MoO_3 nanoblades, we undertook spectral simulations [2]. Because of the broad EPR spectra that lack any resolved fine structure, the characteristic g-values of individual Mo^{5+} species cannot be read out from the spectrum. Instead, a set of known g-values was used, which correspond to various individual Mo^{5+} species as they were determined in reduced α-MoO_3 nanoblades. A set of EPR spectra that correspond to known Mo^{5+} species was generated and compared to the experimental EPR spectra as can be seen in Fig. 5.2.

[2]The simulation was performed by Dr.Mykhailo Azarkh.

The spectral components A, $A^{\bullet}$, B, F, and E were given by K. Dyrek *et al.* [6]. They can be found in distorted octahedral MoO_6 oriented as hexacoordinate, rhombically, and pentacoordinate of rhombic symmetry by removing weak oxygen atoms from Mo – O bonds. The spectral components K, C, and G were eliminated from further analysis because they contain signals outside the range of the experimental spectrum. The spectral component B was found to have a minor contribution to the spectra of N_2 and H_2 treated samples and can be completely neglected in the spectra of as-prepared and vacuum treated types. Thus the corresponding types of defects are not significant in the α-MoO_3 nanoblades as well.

Unfortunately, a detailed simulation of experimental spectra with the remaining components was not possible because the exact line shape of the individual components is not known. However, it is possible to conclude that α-MoO_3 nanoblades are heterogeneous samples that contain several Mo^{5+} based defects.

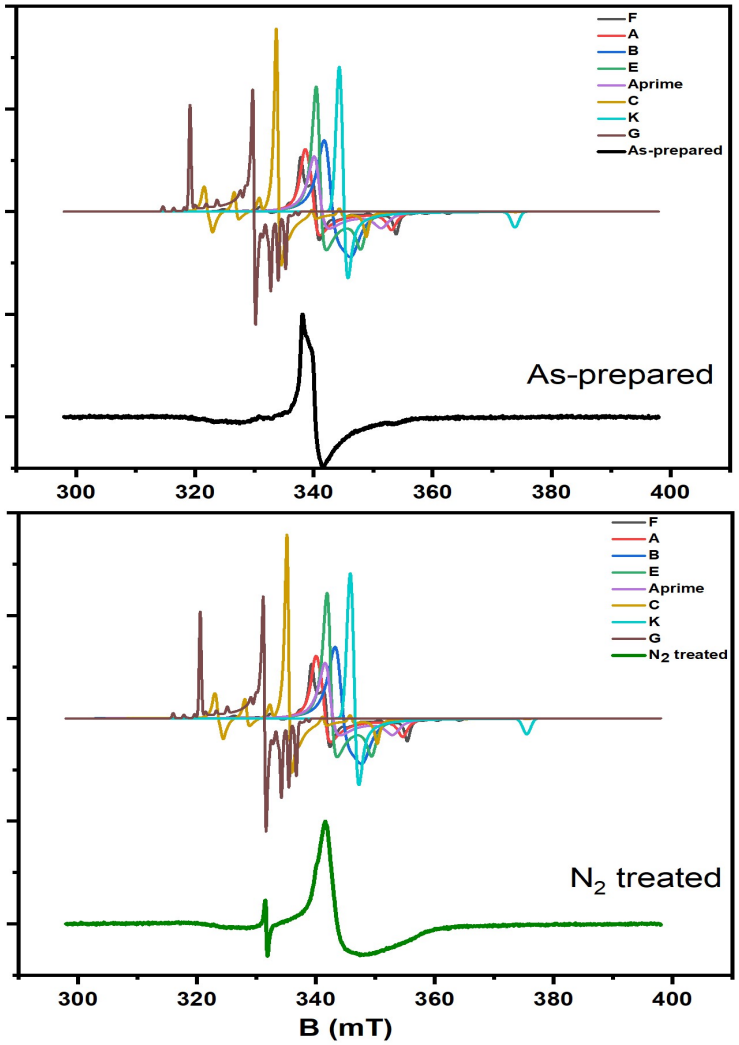

Figure 5.2: EPR spectra of as-prepared α-MoO_3 nanoblades, nanoblades treated under N_2 atmosphere, and corresponding component signals given previously for reduced α-MoO_3 [5, 6].

5.3 X-ray photoelectron spectroscopy analysis

X-ray photoelectron spectroscopy (XPS) [3]was used for identifying the surface stoichiometry of oxidized and reduced vertically aligned α-MoO_3 as is shown in Fig. 5.3. The doublet peaks around 235.6 and 232.5 eV are attributed to the binding energies of $3d_{3/2}$ and $3d_{5/2}$ orbitals of Mo^{6+}, with an energy of spin-orbital splitting of 3.15 eV that is typical for α-MoO_3 [111, 142].

The interfacial reduction of Mo^{6+} and Mo^{5+} at binding energies of 231.2 and 234.35 eV can be seen in XPS spectra for oxidized and reduced α-MoO_3 nanoblades, and they correlate to the existence of oxygen vacancies even in the case of oxidized α-MoO_3 [38, 76]. These findings further confirm our observations, obtained by electronic measurements, of the presence of shallow level in α-MoO_3 nanoblades even under an oxygen rich atmosphere. They are in a good agreement with the theoretical calculation by Guo *et al.* [129], as can be seen in the next chapter for n-type material.

It is worth to mention that in vacuum treated samples, there is a slight shift of the peaks to a higher binding energy by ≈ 0.2 eV. This can be related to the position of the Fermi level and defects [129]. It is crucial to mention that the data fitting deconvolution was found to be difficult to be separated. Moreover, pre-exposure to air gives additional components, which are included to the deficiency and produce uncertainty ratios of the reduced Mo ions to Mo^{6+}. (XPS is a surface sensitive method.)

Additionally, the concentrations of reduced oxidation states are below the detection limit of XPS [142] (lower concentration). Appearance of different oxidation states is consistent with our observation of altering the electronic properties as a proof of existence of oxygen vacancies even in oxidized α-MoO_3.

Furthermore, it is demonstrated that in near-stoichiometric α-MoO_3 the concentration of oxygen vacancies cannot be determined accurately using XPS. Formation of reduced ions releases free electrons, which become delocalized in the layers and act as Drude model like free electrons [31, 76]. Mo^{5+} oxidation states are found to be related to the loss of oxygen, which is associated to octahedral MoO_3 within the bilayer in the (x,z) plane as has been given previously [28].

Careful observation of the vacuum treated sample shown in Fig. 5.3 shows a lower intensity in the deconvolution corresponds to Mo^{5+} than the intensites for the other α-MoO_3 samples reduced under H_2 and N_2. An explanation for this is that the material is solely reduced to Mo^{5+} under the vacuum condition [28].

The existence of oxygen vacancies can be further seen from O1s spectra in Fig. 5.4. The deconvolution can be seen as around 530.8 and 531.7 eV corresponding to Mo – O and Mo – OH, respectively, without observation of water vapor formation, which has been seen even in oxidized α-MoO_3 in previous studies [143]. The hydroxyl components can result from the existence of ionized oxygen species O^{2-} or O^-, where O^- is the dominant ion, and which can have a similar binding energy as lattice oxygen found in our binding energy range [144, 145]. This has been pointed out using EPR measurements.

No observation of the transition to MoO_2 was observed for all conditions, and even no bronze molybdenum oxide (H_xMoO_{3-x}) was formed in this range of applied thermal treatment. As has been demonstrated in the literature, 500 °C is considered as the transition temperature to obtain metallic molybdenum oxide (MoO_2) [28]. Additionally, a longer time is needed to obtain bronze molybdenum oxide [120]. This observation ties very well with prior research showing that in the initial step of reducing α-MoO_3, formation of Mo^{5+} introduces a lattice rearrangement of the corner- to edge-sharing oxygen in the octahedral structure in the lattice [28].

In the N_2 treated nanoblades, no prominent peaks can be found for a binding energy corre-

[3]XPS was measured by Dr.Muhammad Sultan, written and analyzed by me and revised by Dr.Muhammad Sultan.

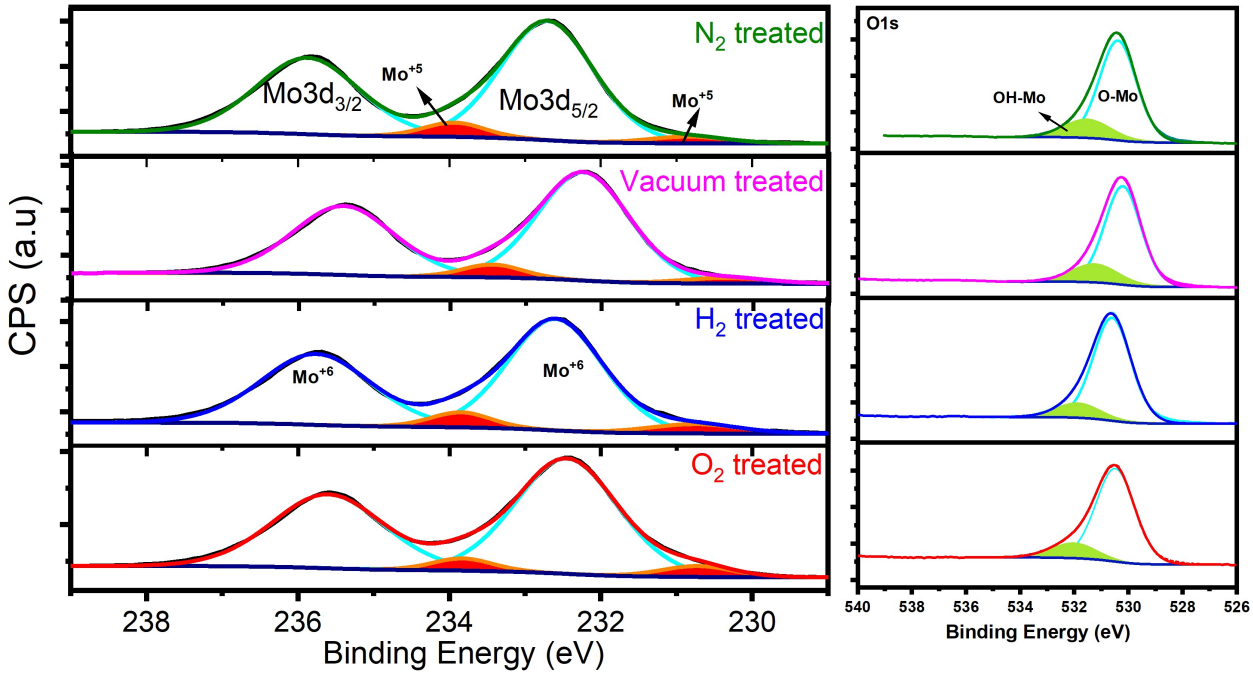

Figure 5.3: XPS spectra of O1s and Mo3d of α-MoO_3 vertically aligned nanoblades treated under O_2, H_2, vacuum and N_2 atmospheres, with indication of deconvolution peaks corresponding to Mo^{6+} and Mo^{+} in Mo3d, as well as O – Mo, OH – Mo for O1s core levels.

sponding to attached N (at 398.5 eV) [85, 146] in the survey spectrum presented in Fig. 5.4, which is identical with that of α-MoO_3 [34]. This can be attributed to the interaction between nitrogen and lattice oxygen and the according release of NO or NO_2 gases, which can be seen as a formation of Mo^{5+} cations in the octahedral structure.

5.4 UV-visible spectrophotometer analysis

Consequently, the optical identification regarding the oxygen deficiency role related to the color center formation and polaron model provides valuable information, which supports our DC activation energies, whether the traps are deep or shallow, in the following chapter.

Diffuse reflectance spectroscopy (DRS) has been applied to our vertically grown α-MoO_3 nanoblades to estimate the dispersion and optical constants using an integrating sphere UV-vis spectrophotometer. DRS is considered as a reliable way of measurement for such film surfaces, where multiple reflections and diffusion of the waves between vertical nanoblades (porous-like surface) are likely to occur. Various models and methods based on the diffuse reflectance are available to determine the optical band gap. In our study, two widely used methods have been applied: The Kubelka-Munk (K-M) function [147, 148], proposed in 1931 [149] (for more details about the measurement see [150]), and another model demonstrated by V. Kumar *et al.* for thick films based on diffuse reflectance spectra.

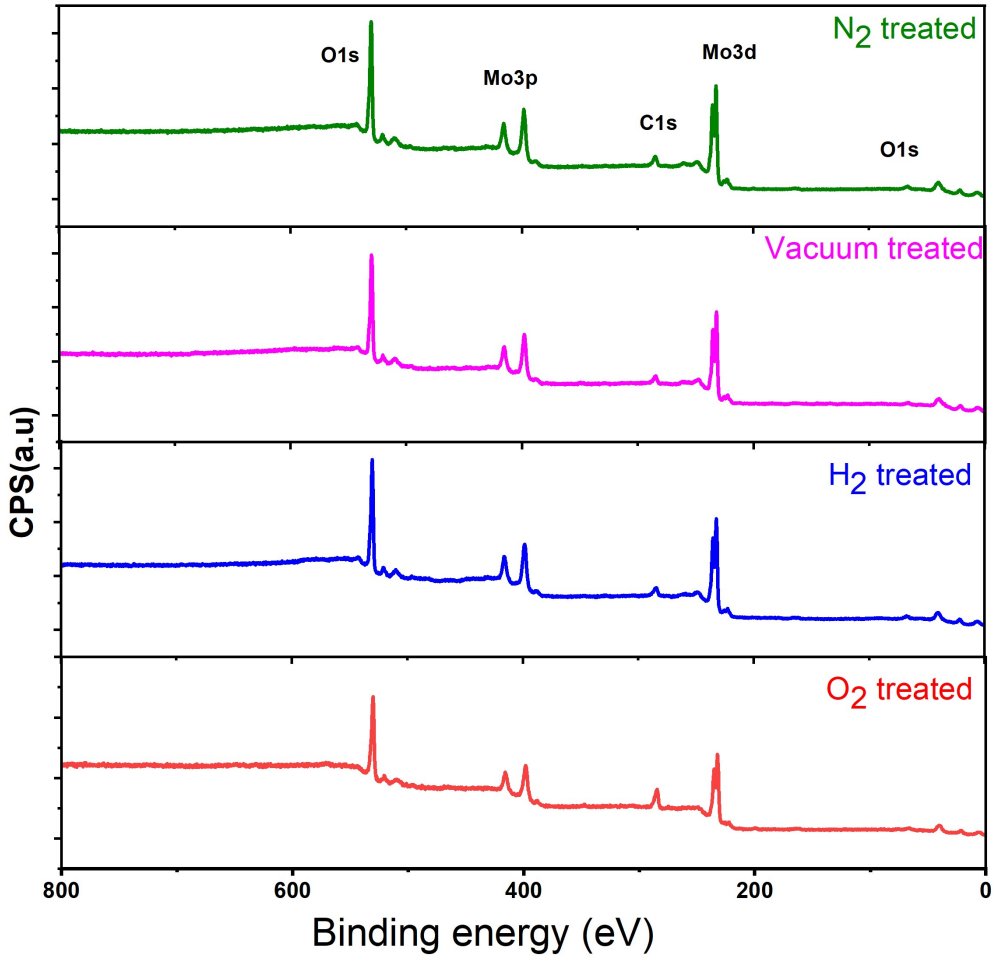

Figure 5.4: XPS spectra survey of vertically aligned α-MoO_3 nanoblades treated under O_2, H_2, vacuum and N_2 atmospheres.

5.4.1 Kubelka-Munk model (K-M)

In this model, the diffuse reflectance function $F(R)$ is proportional to the absorption coefficient α through the following relation [150–152]:

$$F(R) = \frac{(1-R)^2}{2R} = \frac{\alpha}{s} \tag{5.2}$$

Here, s is the scattering coefficient, which can be ignored, since it is independent of the incident wavelength, and α (cm^{-1}) is the absorption coefficient.

Fig. 5.5 (a) shows $F(R)$ versus the incident energy for films that were treated under different atmospheres. The film's color appearance (Fig. (a)-5.5) shows the thermochromic effect as it is well known naturally in α-MoO_3 [65,66]. The observed broad peak around the region of the fundamental absorption in Fig. 5.5 (a) was reported by Dexter to be caused by lattice vibrations and formed color centers (F-centers) in the band gap [153]. The spectra in Fig. 5.5 (a) identify the F-center absorption (as bands 1 and 2), which occur in the range of incident wavelength (585 – 650 nm and 650 – 700 nm), respectively.

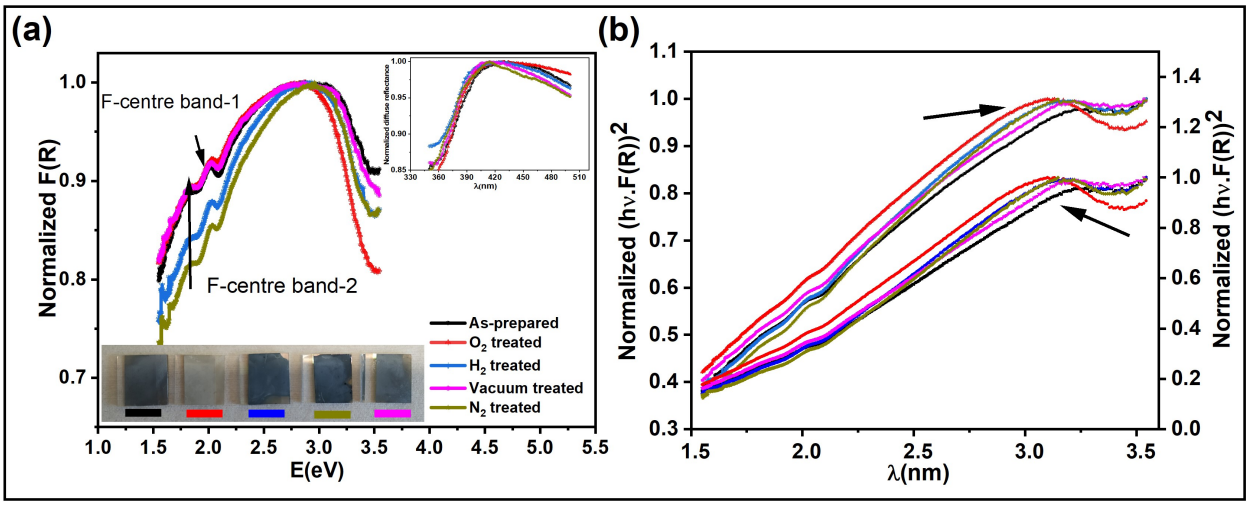

Figure 5.5: (a) Diffuse reflectance spectra of vertically aligned α-MoO_3 on FTO substrates, as-prepared and treated under O_2, H_2, vacuum and N_2 atmospheres. The inset figure shows the optical band gap position. (b) Direct and indirect transition calculated using the K-M function.

Experimentally, two color center bands have been detected: One is related to weakly bound states with lower ionization energy; it can be stabilized at low temperature. The other band has bound excited carriers, which require high temperature, as has been discussed in section 2.6.1 [66].

This supports the existence of F-centers in the sample treated under O_2 atmosphere. F-center bands for as-prepared films and for films that were thermally post-treated under vacuum conditions were found to be barely distinguishable. This observation reveals significant ramping in the colors with a slight shift in the bands toward higher wavelengths for the films: From bleaching white under thermal treated in rich oxygen atmosphere, to dark blue in N_2 atmosphere, which correlates to stoichiometric and deficient vertically aligned α-MoO_3 nanoblades, respectively.

The color center density N (cm^{-3}) can be estimated through Smakula's equation [72]:

$$Nf = C \times 10^{17} \, \frac{n}{(n^2+2)^2} \, \alpha_{\mathrm{Max}} \, u \tag{5.3}$$

where C is a factor depending on the shape of the band (1.29 in case of approximately Gaussian shape; 0.89 in case of Lorentzian shape), f is the oscillator strength (between 0.1 and 1), n is the refractive index ($n = 1.88$) [154], α_{Max} is the maximum absorption coefficient of the band (cm^{-1}), and u is the full width at half maximum of that band (eV).

The oscillator strength has a classical and quantum mechanical explanation, which can involve the expression of the polarizability of the atoms. There is no simple way to have the absolute value of N due to the uncertainty in the band FWHM and overlapping between the bands. So the product values of density of color centers and oscillator strength given in Table 5.2 correspond to their central band energy, which is in good agreement with previous studies.

The optical band gap E_g is given by the McLean relation [155]:

$$\alpha(h\nu)_{\mathrm{ph}} = k \left((h\nu)_{\mathrm{ph}} - E_g \pm E_p \right)^{1/n_{\mathrm{Bg}}} \tag{5.4}$$

where $(h\nu)_{\mathrm{ph}}$ is the incident photon energy, k is a constant, and E_p is the shallow trap level energy (allowed direct transition) or phonon assist transition (allowed indirect transition). The exponent

n_{Bg} is related to the nature of the transition: $n_{\mathrm{Bg}} = 2$ for allowed direct transition, 2/3 for forbidden direct transition, 1/2 for allowed indirect transition, and 1/3 for forbidden indirect transition.

Fig 5.5 (b) indicates both transitions, direct and indirect allowed transition, which show similar values with two relative equal possibilities of direct and indirect transition. As can be seen from Fig. 5.5, there is no significant change in the optical band gap (3.00 ± 0.18 eV). The similarity of the direct and indirect allowed transition can be attributed to the existence of closer trap level to the bottom of the conduction band gap. This can be related to the existence of the conduction band-like of Mo^{6+} as has been discussed in IVCT model (see section 2.6.2), which can be found slightly below the bottom of the conduction band.

However there is a change in the positions of the color center bands and small variations between the concentrations of the color centers under different reducing atmospheres, in comparison to treatment under rich O_2 atmosphere, which shows the lowest density. This can be seen in Table 5.2.

Table 5.2: The estimated values of the product values of color center concentration N and oscillator strength f for as-prepared vertically aligned α-MoO_3 nanoblades on FTO substrates, and for films treated under oxidizing and reducing conditions. Calculated according to the Kubelka-Munk model (K-M) and V. Kumar model at bands (1,2), corresponding to 585 – 645 nm and 650 – 700 nm, respectively.

Sample	K-M method		Kumar *et al.* method	
	Band-1 (cm^{-3})	Band-2 (cm^{-3})	Band-1 (cm^{-3})	Band-2 (cm^{-3})
As-prepared	$(6.35\pm1.54)\times10^{18}$	$(1.09\pm1.13)\times10^{20}$	$(1.07\pm0.93)\times10^{20}$	$(3.89\pm3.67)\times10^{21}$
O_2 treated	$(1.64\pm0.32)\times10^{19}$	$(3.22\pm0.61)\times10^{19}$	$(3.00\pm2.88)\times10^{20}$	$(7.79\pm9.78)\times10^{20}$
H_2 treated	$(1.69\pm1.31)\times10^{19}$	$(2.99\pm0.88)\times10^{19}$	$(3.26\pm0.69)\times10^{20}$	$(2.43\pm0.21)\times10^{21}$
Vacuum treated	$(1.09\pm0.33)\times10^{19}$	$(1.63\pm0.46)\times10^{19}$	$(2.25\pm0.79)\times10^{20}$	$(7.25\pm5.73)\times10^{20}$
N_2 treated	$(1.09\pm0.15)\times10^{19}$	$(1.72\pm0.04)\times10^{19}$	$(3.12\pm0.18)\times10^{20}$	$(1.17\pm0.21)\times10^{21}$

5.4.2 The recent method by V. Kumar *et al.*

This method has been applied to various thick films (> 1 μm) using the diffuse reflectance for estimation of the optical band gap. The method by Kumar *et al.* has been used as a decisive alternative method to determine the optical properties by using the following equation [38, 156]:

$$\frac{(h\nu)_{\mathrm{ph}}}{2h}\ \ln\left(\frac{R_{\max}-R_{\min}}{R-R_{\min}}\right) = k\left((h\nu)_{\mathrm{ph}} - E_{\mathrm{g}} \pm E_{\mathrm{p}}\right)^{1/n_{\mathrm{Bg}}} \tag{5.5}$$

where $R_{\max}$ and $R_{\min}$ are the maximum and minimum reflectance in the reflectance spectra, and R is the entire diffuse reflectance spectrum.

Fig. 5.6 shows the allowed direct and indirect transitions. As we can see, the lowest transition occurs as an indirect transition with an energy of 3.00 ± 0.05 eV, and the direct transition happens at a slightly higher energy of 3.20 ± 0.05 eV. This shows exciton absorption at an energy of ≈ 0.20 eV.

The density of the color centers has been calculated using Smakula's equation 5.3. Table 5.2 shows the given values of Nf corresponding to the different absorption bands. The sample treated under O_2 atmosphere shows lower color center concentration in comparison to other samples treated under H_2 and N_2 atmospheres. This suggests the higher and faster reduction influence by those atmospheres in comparison with vacuum treated samples.

Our results reveal a similarity in the color center concentration for all the conditions corresponding to band 1, which suggests consistent behavior with F* centers (thermodynamic stable center) as given in section 2.6.1. In contrary, according to band 2, there is a statistical distribution for all the cases, which are in a good correlation to the data obtained by EPR measurements. It turns out that it is sufficiently accurate to use Kumar's method, which is broadly in line with our observations.

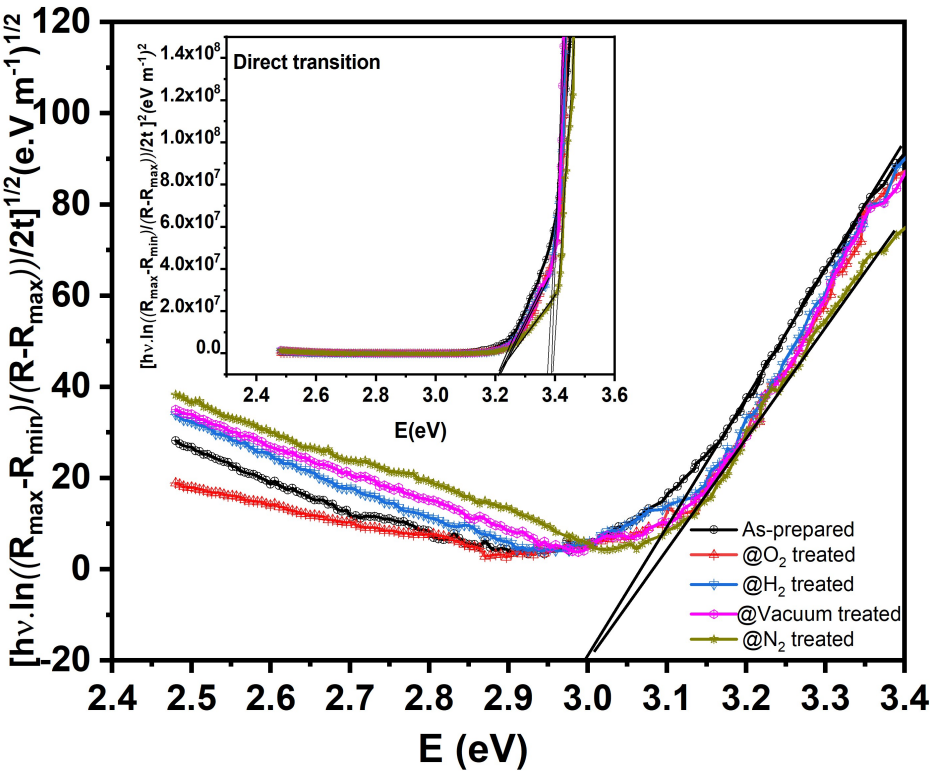

Figure 5.6: Indirect transition of as-prepared vertically aligned α-MoO_3 nanoblades on FTO substrates, and of films treated under oxidizing (O_2) and reducing (H_2, vacuum, N_2) conditions. The inset figure shows the allowed direct transition.

5.5 Photoelectron spectroscopy in air measurements

Photoelectron spectroscopy in air (PESA) measurement has been used to determine the valence band position (ionization energy) of as-prepared, reduced and oxidized vertically aligned α-MoO_3 nanoblades on FTO substrates.

The obtained estimated values show that oxidized vertically aligned α-MoO_3 films on FTO substrates have the deepest valence band position, corresponding to a lower energy level of oxygen vacancies as can be seen in Fig. 5.7 (a). In line with previous reports, introducing oxygen vacancies by treating the samples under reducing atmospheres results in a shift upward in the valence band. This indicates an increase in the free carrier concentration by introduction of oxygen deficiencies into the crystal [76]. The changes in the valence band energy between the different reducing conditions confirm our observation of lower concentrations of oxygen vacancies that have been introduced to the crystal. The obtained results are in good agreement with our calculations using EPR at very

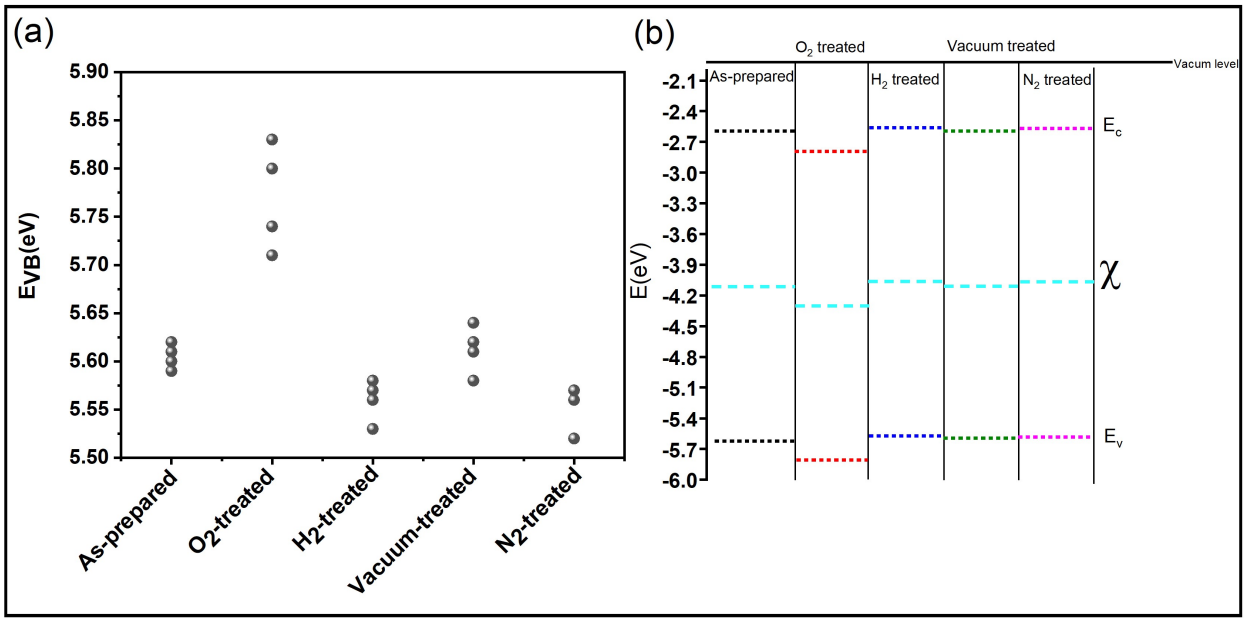

Figure 5.7: (a) Estimated values of the valence band energy E_{VB} relative to the vacuum level for vertically aligned α-MoO_3 nanoblades on FTO substrates, as-prepared and treated under oxidizing and reducing atmospheres. (b) The corresponding estimated energy values of the conduction band E_{C}, the valence band E_{V}, and of the electronegativity χ.

low concentration of oxygen deficiency and inhomogeneity distribution of that kind of defects as seen in HRTEM Fig. 4.19.

It is worth noting that PESA measurements do not provide accurate absolute values of the valence band energy as in the case of ultraviolet photoelectron spectroscopy (UPS). However, since our lower concentration of deficiencies lies under the detection level of 0.5 eV, we were able to provide an approximate evaluation of our energy levels.

The electronegativity (χ) is considered an important concept to introduce different chemical properties. It refers to the attraction force of valence electron to ion cores [157], and its relation to the work function is known as the Gordy-Thomas linear relation [73].

For a higher oxidation state Mo^{6+} concentration, the electronegativity increases in comparison to Mo^{5+}. This introduces donor states followed by a decrease in the work function [4]. The electronegativity describes the mid-gap position and can be calculated using the empirical relation by subtracting the ionization energy by half of the band gap obtained by our optical analysis. This is shown schematically in Fig. 5.7 (b) where χ was calculated according to the mean given values of the valence band energies.

The obtained results are consistent with a previous study on MoO_3 nanoflakes by Alsaif *et al.* [76]. Our results indicate a lower ionization energy of nanoblades in comparison with the reported ionization energy for MoO_3 thin films by $\approx$ 9.3eV [158, 159]. This can be attributed to a higher surface to volume ratio, which allows more interaction with the surrounding atmosphere and introduces a higher concentration of lower oxidation states of the cation. Hence, a thickness dependent work function of MoO_3 as given by Greiner *et al.* showed that within the first 10 nm of the films, there is a drop in the work function as a result of the formation of lower oxidation energies [4]. This can give some indications about the nature of nanostructure as high surface

materials, which can facilitate the formation of different oxidation states.

As a conclusion of our characterization of the oxygen deficiency in α-MoO_3 nanoblades, in both cases oxidized and reduced structures have shown a smaller deviation from the stoichiometric condition. The color center formation has been proved and it provides an explanation for the question why no changes have been observed in the fundamental band gap. In the next chapter we will introduce the influence of such treatment conditions on the electronic properties of vertically aligned α-MoO_3 nanoblades.

6. Electronic characterization of vertically aligned α-MoO_3 nanoblades

6.1 Overview

It is of interest to investigate the metal/dielectric material interface, although a lot of difficulties faces researchers in this area. The conduction mechanism is studied to understand the charge carrier transport, the relaxation mechanism, and other properties that are important for semiconductor industry electronic devices, solar cells and integrated circuits [160].

To be able to do this study, a lot of effort and development in the area of controlling the geometry of the device, such as electronic configuration and interfaces of the device, have to be achieved [161]. Therefore, a simple electrical device needs to be developed by using metal electrodes. The metal electrodes play a crucial rule in the α-MoO_3 conduction mechanism because a different work function leads to a different barrier height.

A previous study that has been employed to α-MoO_3 between several two metal electrodes (noble and non-noble metals) has shown a wide range of work functions related to metal/α-MoO_3 oxidation potentials at the interface. This can occur due to the reactivity nature of the metal electrode toward α-MoO_3 [4]. The study revealed a thin excess oxide layer formed on the interface between the metal and our metal oxide. The layer forms as a reducing effect on the cation Mo^{6+} to Mo^{5+} and Mo^{4+}, where the reduction degree and the thickness of this excess layer depends on the metal reactivity. The least reactive metal was found to be the noble metal gold.

As already stated in our previous discussion (2.6), it is hard to obtain stoichiometric α-MoO_3 which is considered as insulating material. Non-stoichiometric α-MoO_3 has a wide range of conductivity depending on the reduction degree. The latter is related to the gap states formed as a result of formation of Mo^{5+} and Mo^{4+} bands.

In this chapter, we investigate the electrical properties of as-prepared, oxidized and reduced vertically aligned α-MoO_3.

6.2 Electrode configurations

Electrical connections for vertically aligned nanostructure films are always a big challenge. We need a direct contact to the metal electrodes but must take precautions not to destroy the structure. In principle there are two types of electrode configurations: Co-planar electrodes (top or bottom contacts) and top-bottom electrodes. The literature on co-planar and top-bottom electrode configurations on such nanostructure films is less consistent. In this section, different electrode configurations will be introduced to obtain measurable stable contacts.

6.2.1 Co-planar electrode configurations

In our study, different shapes and dimensions of the co-planar electrodes have been prepared. These can be seen in Fig. 6.1.

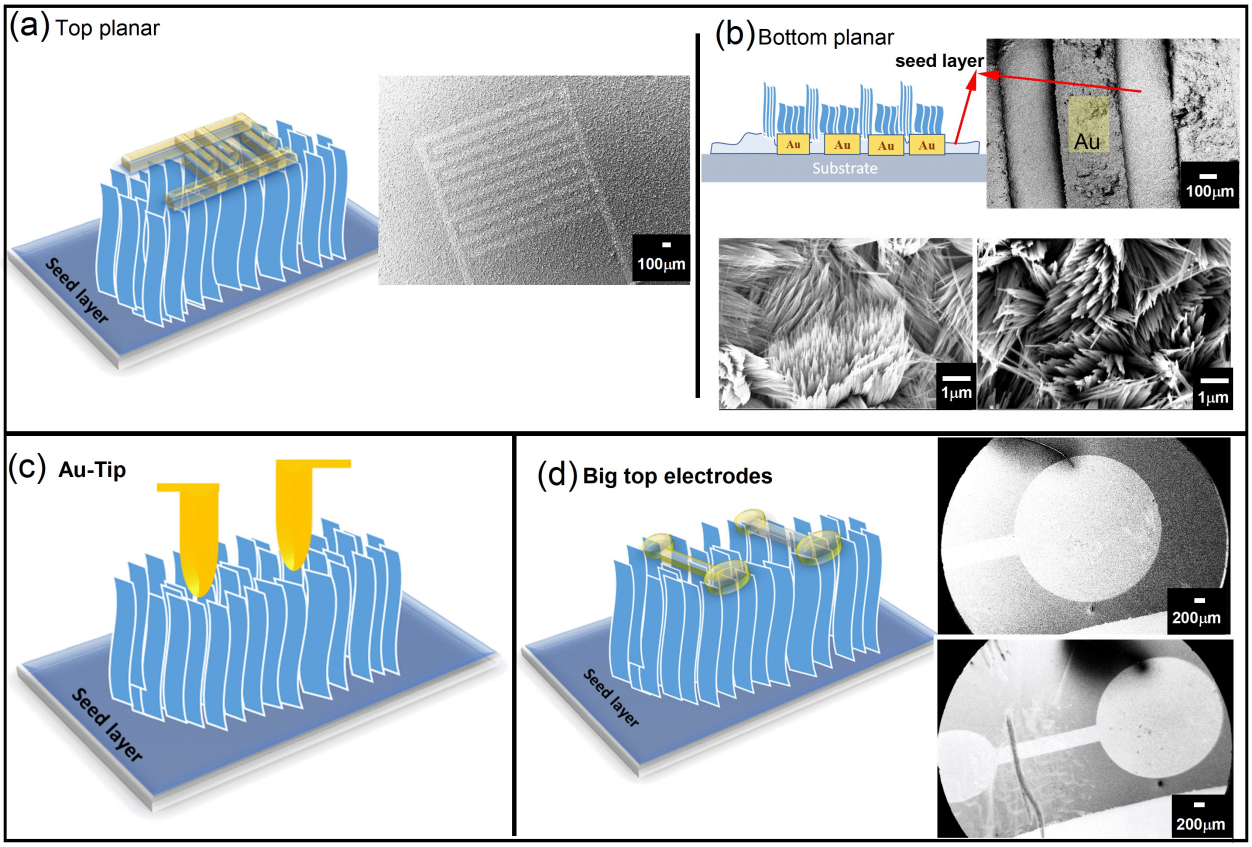

Figure 6.1: (a-d) Possible co-planar Au electrodes for vertically aligned α-MoO_3 nanoblades. FE-SEM micrographs indicate: (a) Top view of vertically aligned α-MoO_3 nanoblades coated with evaporated interdigitated Au electrodes. (b) Top view of grown vertically aligned α-MoO_3 nanoblades on Au pre-patterned substrates with two different length scales of the nanoblades, corresponding to different areas with/without Au layer. (d) Top view of vertically aligned α-MoO_3 nanoblades covered with a top Au layer evaporated through an evaporation mask.

- In Fig. 6.1 (a), a thermal evaporation mask has been used to deposit top electrodes (Au of 120 nm thickness) on pre-prepared and treated vertically aligned α-MoO_3 nanoblades with a width of 100 μm. These electrodes suffer from two problems: First, very small terminals are found difficult to be connected to our setup (technical problem). Second, if the top interdigitated electrodes are deposited on the grown and treated structures on Si substrates, the terminals of Au electrodes will be directly connected to the Si substrate. As has been proven, deposition of Au onto Si causes a substitution-interstitial diffusion of Au into the Si crystal. This causes vacancies by dislocation and damage in the device [162, 163].

- In Fig. 6.1 (b), bottom interdigitated Au electrodes of 120 nm thickness have been thermally deposited, followed by seed layer deposition of Cr/MoO_3, followed by the synthesis procedure

(hydrothermal reaction) and post treatment of the vertically aligned α-MoO_3 nanoblades. This electrode configuration has two further problems: First, due to the existence of a Au layer directly on the substrate before deposition of the seed layer and hydrothermal reaction, the growth mechanism of the nanoblades tends to alter. We can see this in FE-SEM micrographs (see Fig. 6.1 (b)). This issue needs a further growth mechanism modification and optimization to understand the role of the Au layer underneath the optimized seed layer. Second, the existence of a Cr/(MoO_3) seed layer, which is considered as a compact layer on the top of the co-planar electrodes, contributes to the current flow and impedes the current evaluation of the nanoblades. Additionally, this problem arises even more due to a Cr-oxide layer between the compact layer of α-MoO_3 which can hinder the current flow.

- In Fig. 6.1 (c), two Ir/Au tips of 1 mm diameter have been placed directly on the grown and treated α-MoO_3 nanoblades. This electrode configuration suffers from an undefined contact area as we can see in the top-bottom electrode Fig. 6.2 (a). In addition, there can be a gap of air and adsorbed water between the contact tip and the nanoblades, which leads to a rectifying behavior that does not originate from our structures. This effect has been intensively investigated in previous studies [164] including a monolayer of organic compounds, which exist on top of semiconductor nanostructure films to form metal-insulator-semiconductor diodes (MIS) with a rectifying behavior.

- Fig. 6.1 (d) introduces the most suitable electrode configuration to our study: Two top evaporated Au electrodes of 120 nm thickness were directly evaporated through a mask onto grown and treated vertically aligned α-MoO_3 nanoblades. This configuration is found to be fitting well to our contacting probes. It causes no deformation in the nanoblades and offers a well-defined contact area.

6.2.2 Top-bottom electrode configurations

For this kind of electrode configuration, our aim was to measure the conductivity through the nanoblades without deformation or detaching them from the substrates. This is a challenging problem and was approached by various trials as shown in Fig. 6.2.

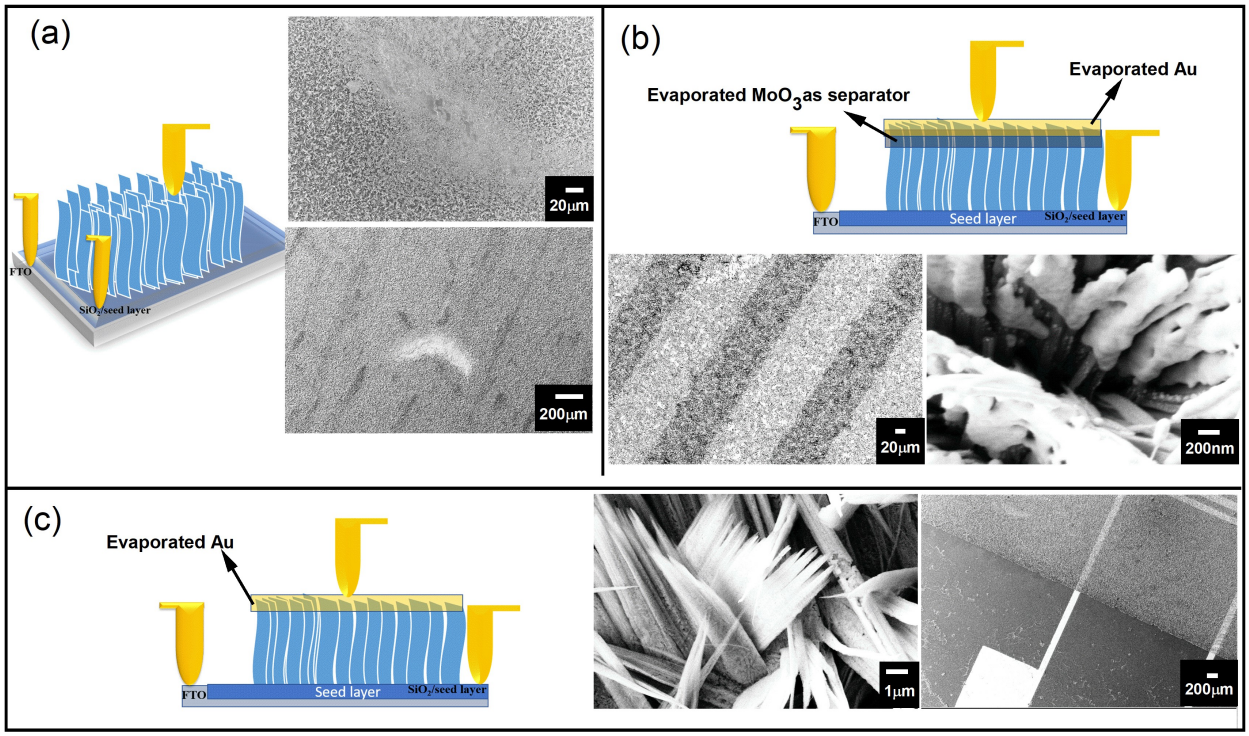

Figure 6.2: Possible top-bottom Au electrodes on vertically aligned α-MoO_3 nanoblades. FE-SEM micrographs indicate: (a) Influence of heat within the electronic measurements, and weight of the Au tip on vertically aligned α-MoO_3 nanoblades, respectively. (b) Top view of vertically aligned α-MoO_3 nanoblades and evaporated separator and Au layers. (c) Top view of vertically aligned α-MoO_3 and evaporated Au layer.

- In Fig. 6.2 (a), a direct top-bottom contact has been used by applying Ir/Au contacting tips of 1 mm diameter to form (Au-tip/FTO/Cr/α-MoO_3/α-MoO_3 nanoblades/Au-tip) or (Au tip/α-MoO_3/α-MoO_3 nanoblades/Au tip) (for Si/SiO_2). As can be seen in the FE-SEM micrographs, the nanoblades have been damped down. Additionally, if we apply heat (necessary for the conduction mechanism study), the nanoblades melt together and cause a ridge deformation in the film. This can be attributed to two factors: The heavier weight of the Au tips (0.5 g) on the structures (20 – 50 nm width), and different thermal expansion of Au (7.8×10^{-6} K^{-1} [165]) and α-MoO_3 (around 0.4×10^{-5} K^{-1} [166]). Hence, the thermal expansion causes changes in the material shape and volume due to an increase in the temperature. This can be a good explanation of such a flat melted layer of nanoblades after heating the substrates during the electrical conduction measurement.

- Fig. 6.2 (b) shows another attempt to measure the nanoblades from a top-bottom terminal, and also assuring that no short circuit (FTO substrate) can happen. An additional layer has

been thermally evaporated between the top evaporated Au (120 nm) and α-MoO_3 nanoblades as a separator. This layer (separator) consists of a 60 nm evaporated MoO_3 layer. One primary problem for this configuration is the amorphous nature of the separator layer (MoO_3), which has poor conductivity (current flow not measurable). Besides, it causes another device mechanism as a heterojunction between the α-MoO_3 nanoblades and an amorphous MoO_3 layer.

- Fig. 6.2 (c) shows a directly evaporated top Au electrode of 120 nm thickness and direct contact to the substrate (FTO or the seed layer of Cr/MoO_3 on Si/SiO_2 substrates). As we can see, the uncertainty of the top electrode is very high, which hinders accurate measurements and reproducible current values. Since the evaporated gold can be attached randomly to the nanoblades, the dimension of the film thickness will be not consistent.

6.3 Temperature dependent current-voltage characteristics

After investigating different electrode configurations tested in order to obtain reproducible and highly accurate electrical measurements, which fit well to our technical facilities, the co-planar big electrodes (6.1 (d)) offer us the best choice. Temperature dependent current-voltage characteristics have been measured on as-prepared vertically aligned α-MoO_3 and films treated under oxidizing and reducing atmospheres. For simplicity, FTO substrates have been used for the electrical characterization, since it is a desirable transparent substrate for semi-transparent organic photovoltaic devices and other energy production applications [167].

6.3.1 Low bias region conduction mechanism

A typical room temperature I-V characteristic of as-prepared Au/MoO_3 nanoblades and α-MoO_3 that was oxidized or reduced under O_2 or (H_2, vacuum, N_2) rich atmospheres, respectively, on FTO substrates is shown in Fig. 6.3.

Our designed shape of electrodes offers higher sensitivity to the current flow in comparison to uniform conventional rectangular electrodes, as has been shown in a previous study [168]. Besides, it has been demonstrated that the narrow gap between the electrode terminals leads to a lateral current flow. This is contrary to a wide gap between the co-planar electrodes, where a lateral and horizontal current flow is favorable to happen (down to the substrates) [169] as can be seen in Fig. 6.3 (d) .

Therefore, we supposed that there are two possible electric pathways: One pathway is across the interconnected nanoblades and the nanoblades to the seed layer, and then again through the nanoblades to the second terminal electrode (see Fig. 6.3 (d)). To clarify the contribution of the seed layer, a fast electrical measurement has been performed using a nanoprobing system, since the seed layer suffers from pin-holes (cannot use FTO) as can be seen from Fig. 4.4.

Fig. 6.4 (a) shows the I-V characteristic of the seed layer on Si/SiO_2 wafer, which indicates an almost insulating behavior of this layer at room temperature. This result is consistent with the nature of the air treated α-MoO_3 as insulator layer (see 4.2.1) [170–172] [1]. Additionally, the Cr layer is not a compact layer but rather contains an island-like morphology (see 4.2.1). Moreover, as is given in Fig. 6.4 (b), hardly any current flows through seed layer in the room temperature [from the top of the vertically aligned α-MoO_3 though the seed layer].

Subsequently, the device resistance can be simplified as shown in Fig. 6.4 (c). Here, the total resistance is a series of resistances: Two metal contacts to the vertically aligned α-MoO_3 nanoblades,

[1] Seed layer's I-V characteristics were performed by Mr. Stefan Schupp, written and analyzed be me.

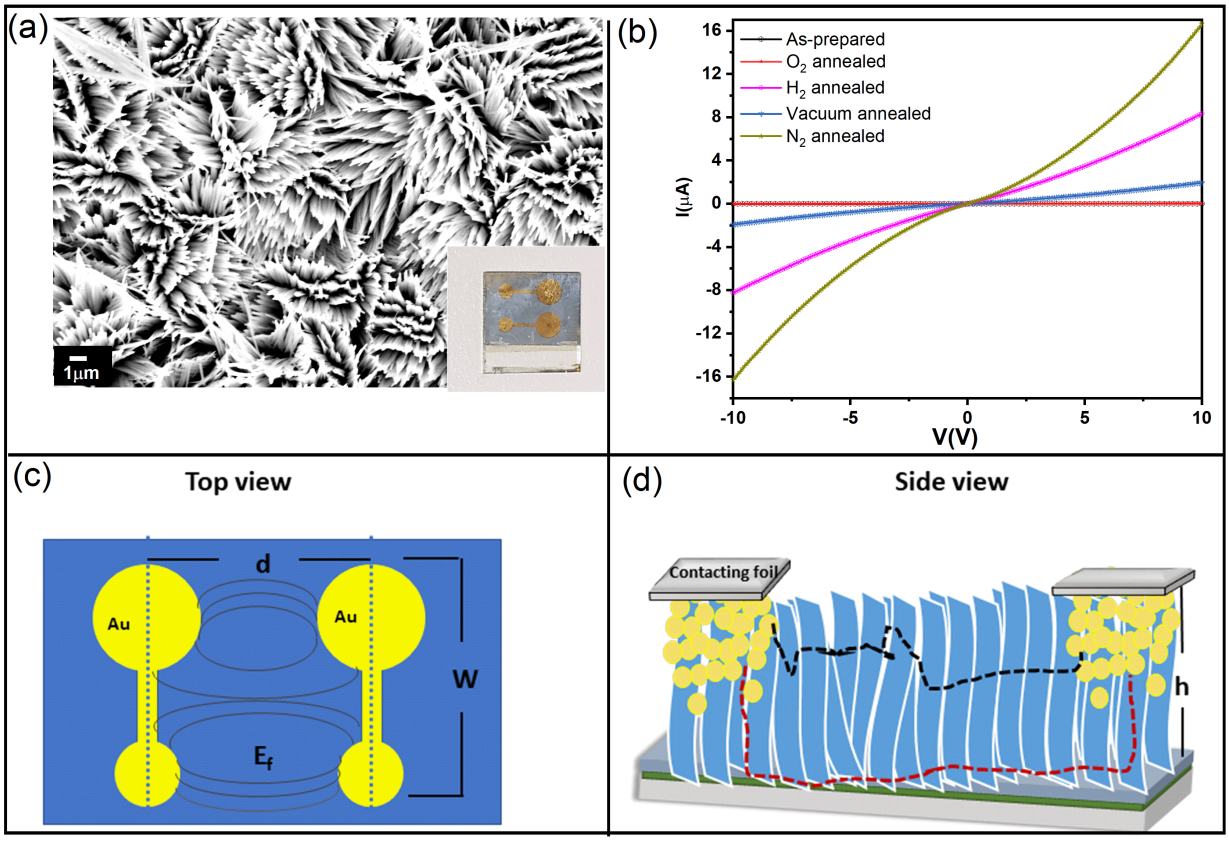

Figure 6.3: (a) FE-SEM micrograph of evaporated Au on the vertically aligned α-MoO_3 nanoblades. The inset image indicates the final shape of the electrical device. (b) Room temperature I-V characteristics of as-prepared and vertically aligned nanoblades on FTO substrates, and ones treated under O_2, H_2, vacuum, N_2 atmospheres, respectively. (c) Top view of the evaporated co-planar Au electrodes (d is the distance between the two central points of the electrodes terminals, W is the length of the electrode, E_f is an illustration of the supposed electrical field flow). (d) Side view of the electrical device (h is the nanoblades length) with illustration of possible electrical field flow paths. The red dashed line represents the flow through the nanoblades to the seed layer, and the black dashed line represents the path through the interconnected nanoblades.

the boundaries between the nanoblades themselves, and barely the seed layer contributing to the current flow.

Temperature dependent I-V characteristics have been recorded and plotted on a semi-logarithmic scale in Fig. 6.5 (a-e). The semi-logarithmic temperature dependent I-V curves show nonlinearity and symmetric trends in both forward and reverse bias. This behavior suggests the formation of a lower Schottky barrier at the interfaces between the metal electrode and the nanoblades (Au/α-MoO_3Au diode) [173, 174]. The semi-logarithmic temperature dependent I-V curves show two linear regions separated by transition segments (0 – 3 and 4 – 10 V). Hence, the power law ($I \propto V^m$) has to be applied, where the m value indicates the predominant mechanism in the applied voltage range. The exponent m is found to equal 1 in the first region [174]. Therefore, the dominant mechanism in the first voltage range implies ohmic conduction mechanism. The ohmic

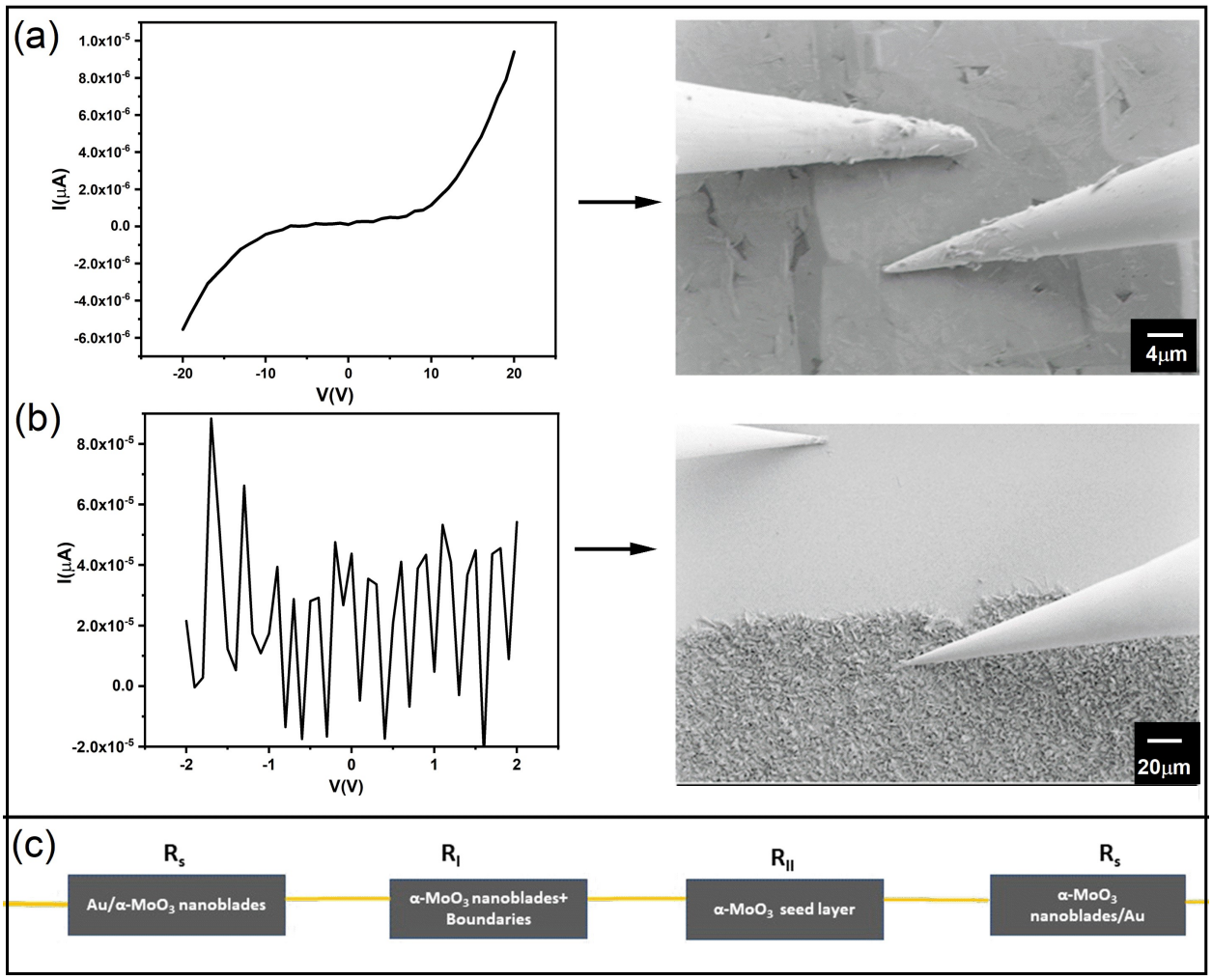

Figure 6.4: (a) Room-temperature I-V characteristic of the seed layer of 10 nm/100 nm of Cr/MoO_3 on Si/SiO_2 substrates with indication of the measured device FE-SEM micrograph. (b) I-V characteristic of vertically aligned α-MoO_3 nanoblades as top-bottom electrode configuration through the seed layer on Si/SiO_2 substrates with indication of the measured device FE-SEM micrograph.

conduction mechanism categorizes as a bulk limited conduction mechanism, which shows dependence on the semiconductor intrinsic properties resulting from the movements of mobile electrons in the conduction bands and holes in the valance band [160].

The electrical conductivity (σ) has been evaluated according to an ohmic law mechanism and is given by [175]:

$$J = \sigma E \quad \Rightarrow \quad I = \sigma \, \frac{A}{d} \, V \tag{6.1}$$

$$\sigma = en\mu \tag{6.2}$$

$$n = n_0 \, \exp \, \frac{-(E_\mathrm{C} - E_\mathrm{F})}{k_\mathrm{B} T} \tag{6.3}$$

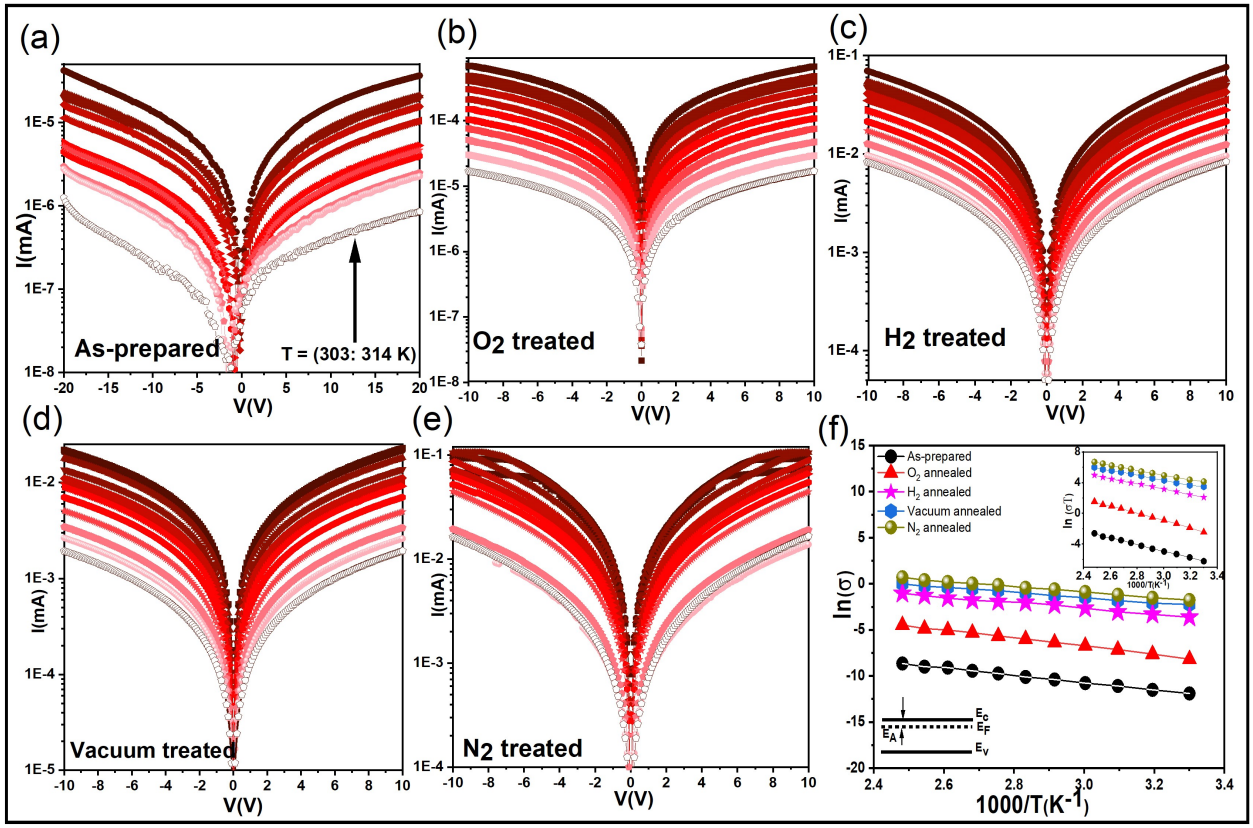

Figure 6.5: (a-e) Semi-logarithmic I-V characteristics of as-prepared vertically aligned α-MoO_3 nanoblades and vertically aligned nanoblades on FTO substrates treated under O_2, H_2, vacuum, N_2 atmospheres, respectively. (f) Arrhenius plot on the ohmic region of the applied voltage (0–3 V) with schematic shows the corresponding activation energy in the band diagram. The inset figure shows the Arrhenius plot corresponding to the hopping mechanism in the same region of the applied voltage.

$$\sigma = e\mu n_0 \exp \frac{-(E_C - E_F)}{k_B T} \tag{6.4}$$

$$\sigma = \sigma_0 \exp \frac{-(E_C - E_F)}{k_B T} \tag{6.5}$$

where J is the current density, E is the applied electric field, $A = 3.5 \times 10^{-8}$ m^2 is the cross section area, which has been calculated by multiplying the total length of the electrode $W = 8.71 \times 10^{-3}$ m with the height of the film $h = 4 \times 10^{-6}$ m according to Fig. 6.3, d is the average electrodes separation distance of 4.67×10^{-3} m [176,177], μ is the carrier mobility, n is the thermal equilibrium concentration of electrons in the conduction band, n_0 is the effective density of state function in the conduction band, and $(E_C - E_F)$ is the distance between the bottom of the conduction band and the Fermi level [175].

In order to evaluate the concentration of free electrons, the type of defects, and their position away from the Fermi level, $(E_C - E_F)$ can be determined from an Arrhenius plot $\ln(\sigma)$ versus $1000/T$, see Fig. 6.5 (f). In case of a linear relation, the slope value of $(E_C - E_F)$ is considered as the activation energy E_A. It can be obtained by the slope of the curve.

Table 6.1: Room-temperature electrical conductivity, activation energy (E_A), and hopping activation energy ($E_{hopping}$) in the applied voltage region of 0 – 3 V for as-prepared vertically aligned α-MoO_3 nanoblades and films treated under (O_2, vacuum, H_2, N_2) rich atmospheres.

Sample	Conductivity ($S\,m^{-1}$)	E_{A1} (eV)	$E_{hopping}$ (eV)
As-prepared	$(6.04 \pm 2.85) \times 10^{-6}$	0.34 ± 0.02	0.38 ± 0.05
O_2 treated	$(3.67 \pm 0.90) \times 10^{-4}$	0.38 ± 0.02	0.41 ± 0.02
H_2 treated	$(9.95 \pm 2.57) \times 10^{-2}$	0.23 ± 0.01	0.24 ± 0.02
Vacuum treated	$(2.60 \pm 0.33) \times 10^{-2}$	0.26 ± 0.01	0.29 ± 0.00
N_2 treated	$(12.80 \pm 1.79) \times 10^{-2}$	0.28 ± 0.01	0.30 ± 0.01

Table 6.3.1 shows calculated room temperature conductivities and activation energies of as-prepared vertically aligned α-MoO_3 nanoblades and devices treated under O_2, H_2, vacuum, N_2 atmospheres, respectively. The electrical conductivity in general revealed significantly higher values in comparison to similar structures in a previous study [130]. The trend values suggest more improvement in the obtained conductivity for films treated under reducing conditions (H_2, vacuum, N_2). As expected, O_2 treated nanoblades show the lowest conductivities, which is attributed to the oxygen re-adsorption and restitution to the crystal. It is worth to notice that due to their higher conductivity performance, the N_2 treated samples show a sudden decrease of the current at higher temperature, which can be attributed to damage or deformation in the structures (see 6.7 (f)).

The higher conductivities can be attributed to different factors: The higher density of the interconnected nanoblades grown on the films, which facilitate the carrier transport [130], the higher surface to volume ratio of the very thin sheet-like structure, and higher crystallinity nature [130] of the structure as has been proven by our XRD analysis (4.5.1).

The obtained values of the activation energies (E_A) imply the existence of shallow trap levels close to the bottom of the conduction band (E_C). Explicitly, the obtained data accounted to previously reported theoretical and experimental studies [7]. vdW-DFT calculations showed that the transition energies of the three different oxygen vacancy positions to the valance band maximum follow the order of $O_1 < O_3 < O_2$ (see Fig. 4.18). Based on their study, the O_1 vacancy constitutes the deepest intra-band level, whereas the O_2 vacancy reveals the shallowest defect state as indicated in Fig. 6.6.

A further study by Ding *et al.* [30] on small polarons (refer to Mo^{5+}) revealed hopping and polaron migration through different paths, distances and ranges of the activation energy in the crystal structure (Fig. 4.18) as summarized here:

1. A hopping and polaron migration through x-direction to a neighboring Mo-site in the x-z-plane (corner sharing oxygen) within the bi-layer in a hopping distance of 3.96 Å.

2. A hopping and polaron migration through z-direction in the x-z-plane (edge-sharing oxygen) within the bi-layer in a hopping distance of 3.7 Å.

3. A hopping and polaron migration in z-direction within the zig-zag direction in the same bilayer of (x,z) with a hopping distance of 3.39 Å.

4. A hopping and polaron migration across inter-bilayers in y-direction cross van der Waals gap within a hopping distance of 4.96 Å.

According to these paths of polaron migrations, the activation energy shows anisotropic behavior. The lowest energy is in paths 1 and 2 followed by path 3, in contrast to the highest activation

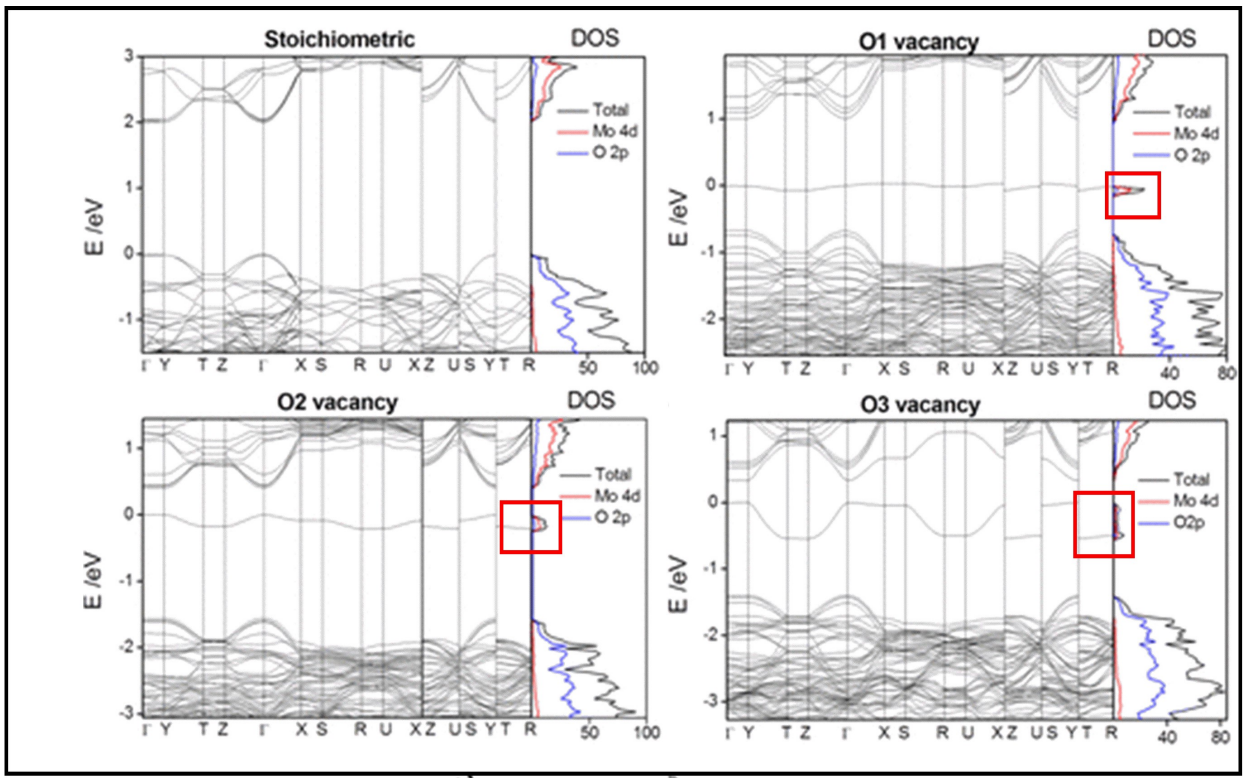

Figure 6.6: Band structure of stoichiometric and non-stoichiometric α-MoO_3 with oxygen vacancies in O_1, O_2, O_3 sites in the crystal, with indication of density of states of Mo-4d and O-2p in addition to the Fermi level at 0 eV. The red box indicates the formation of shallow and deep states within the band gap, "after [7]".

energy within the van der Waals gap. In combination with the small polaron theory, which has been investigated intensively by Mott (see 2.6.3), this affirms that the small polaron migration between different metal oxidation states is likely to occur. Besides, the conductivity happens as a result of electron movement between various cation sites, which suggests the hopping mechanism [178].

The hopping activation energy E_{hopping} can be determined through the following equation [178]:

$$\sigma T = \sigma_{\circ\circ} \exp\left(\frac{-E_{\text{hopping}}}{k_{\text{B}}T}\right) \tag{6.6}$$

where $\sigma_{\circ\circ}$ is the Mott constant for the hopping mechanism related to transition metal oxides. (For more information see [178].)

The inset of Fig. 6.5 (f) shows a good fit of $\ln(\sigma T)$ versus $1/T$ to the small polaron model. It is worth to note that E_{hopping} at high temperature reflects not only the Polaron hopping energy but also disorder energy. This can explain the higher obtained activation energies of E_{A} *via* the hopping mechanism (see Eq. 2.10) in respect to the ones obtained from the Arrhenius plot. Additionally, the higher values of the hopping energies correlate with the activation energy from the extrinsic Fermi level concurred with the Mott model. The barely excess in the hopping related energies can be attributed to the average change in the energy within the movements between one cation site to other cation sites [178].

The obtained activation energies of the reduced vertically aligned α-MoO_3 nanoblades (H_2,

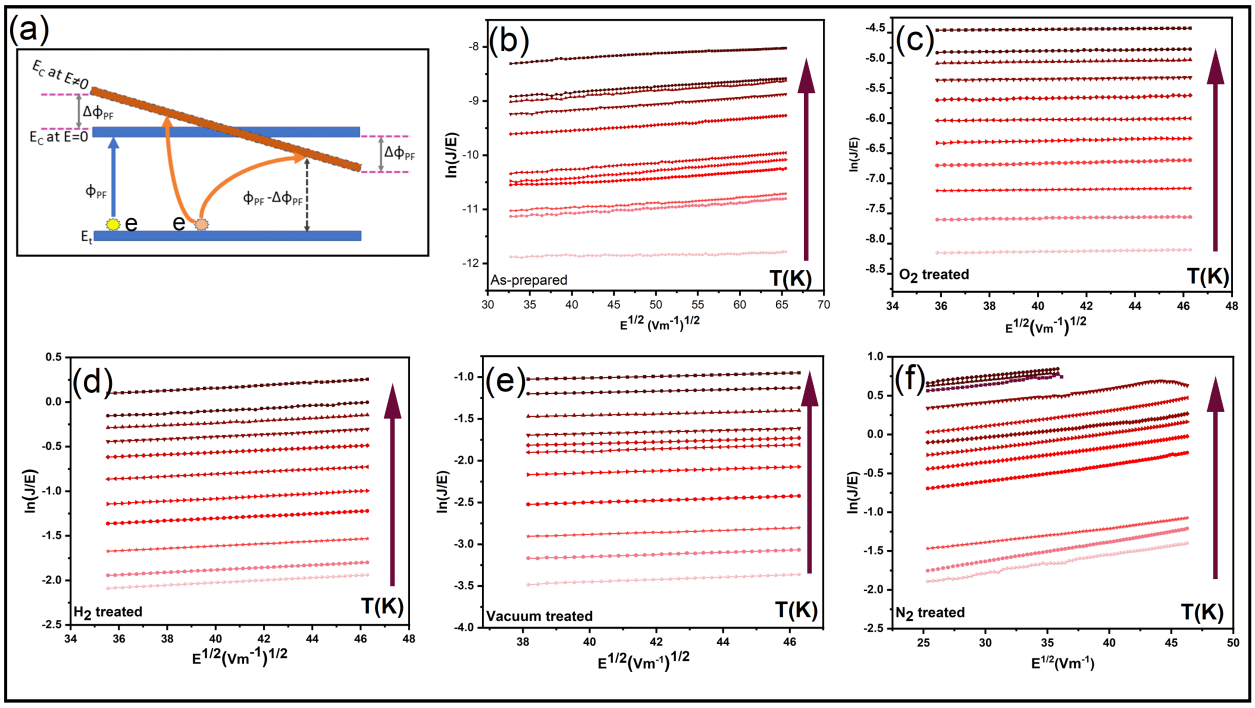

Figure 6.7: (a) Schematic of Poole-Frenkel mechanism with indication of the conduction band E_{C} with and without the applied electric field E, trap level E_{t}, trap level energy Φ_{PF}, and the barrier lowering $\Delta\Phi_{\mathrm{PF}}$ "after [8]". (b-f) $\ln(J/E)$ versus $E^{1/2}$ in the temperature range of 303 – 403 K[as indicated with the arrow's direction].

vacuum, N_2) tie well with theoretical calculations by Ding *et al.*, which confirm Polaron migration in x-z-plane. However, the higher values of the oxidized vertically aligned α-MoO_3 nanoblades may suggest polaron migration across the zig-zag path. Subsequently, the existence of shallow levels as intrinsic defects even in the oxidized vertically aligned α-MoO_3 nanoblades confirms its n-type nature in stoichiometric form, and degenerated n-type under reducing atmospheres [129].

6.3.2 High bias region conduction mechanism

In the higher voltage region, the power law ($I \propto V^m$) shows an exponent of $1 < m < 2$, which suggests a thermionic emission, or Poole-Frenkel emission. Poole-Frenkel emission gives a better fit to our case, since it is independent from the direction of the field (the symmetric behavior of the current) [174, 179].

Poole-Frenkel emission is due to field enhanced thermal or electrical excitation of trapped electrons from a localized state into the conduction band. This is known as bulk-limited conduction [8]. It is known as the dominant mechanism in a (metal oxide)/metal junction, where it involves defects and impurities. The Poole-Frenkel emission results from lowering the coulombic potential by the applied electric field [179]. The restoring force arises because of the coulombic attraction between the electrons and positive charges [179]. In our case, it arises because of the attraction between free electrons and oxygen vacancies as a polaron interaction.

The barrier lowering ΔQ_{PF} for the Poole-Frenkel emission is given by the following relation [8, 179]:

$$\Delta Q_{\mathrm{PF}} = \left(\frac{e^3 E}{\pi \epsilon_0 \epsilon_{\mathrm{r}}}\right)^{\frac{1}{2}} \tag{6.7}$$

where $\epsilon_0 = 8.85 \times 10^{-12}$ Fm^{-1} is the permittivity of free space, and $\epsilon_{\mathrm{r}} = 5.7$ is the high frequency relative permittivity (dielectric constant) of α-MoO_3 [53], where it was found to be in the range from 9×10^{-4} eV to 2×10^{-3} eV in the applied voltage region of 4 – 20 V.

The current density J_{PF} is given by [160]:

$$J_{\mathrm{PF}} = en\mu E \exp\left[-\frac{(Q_{\mathrm{PF}} - \Delta Q_{\mathrm{PF}})}{r k_{\mathrm{B}} T}\right] \tag{6.8}$$

The equation of the Poole-Frenkel mechanism can be written in a logarithmic form as follows:

$$\ln(J/E) = \ln(en\mu) - \frac{\Phi_{\mathrm{PF}}}{r k_{\mathrm{B}} T} + \frac{\sqrt{\frac{e^3}{\pi \epsilon_0 \epsilon}}\, E^{\frac{1}{2}}}{r k_{\mathrm{B}} T} \tag{6.9}$$

and/or:

$$\ln(I/V) = \ln(enA\mu/d) - \left(\frac{\Phi_{\mathrm{PF}} - \Delta\Phi_{\mathrm{PF}}}{r k_{\mathrm{B}} T}\right) \tag{6.10}$$

where Q_{PF} is the trap level energy, and r is a parameter ranging from 1 to 2 depending on the position of the Fermi level. A value of $r = 1$ reflects that the density of electrons n is less than the density N_{d} of donor sites, and a value of $r = 2$ reflects that the electron concentration is higher than the donor site concentration [179]. The latter situation applies to our case because every oxygen vacancy site produces 2 electrons.

Fig. 6.7 shows well-matching curve fits of $\ln(J/E)$ versus $E^{1/2}$, which confirms that the electric field is governed by the Poole-Frenkel mechanism. It is worth to mention that the determined slopes are not consistent with the theoretical value, which was calculated using the reported standard value of the high frequency dielectric constant of α-MoO_3 [8].

In line with several studies mentioned previously, the deviation between the experimental slopes and the theoretical value was found to be attributed to lowering of the barrier height for the charges, where ejection of charges from the trap level is happening frequently at T$>$ 0 K (without applied voltage). Additionally, both types of charges (electron/hole) related to donor and acceptor trap levels, respectively [8], can be found in the metal oxides. This can be connected to the formation of positive charge as a hole (oxygen vacancy) and polaron. This leads to a confirmation of polaron migration in the crystal 2.6.3.

Consequently, a higher charge density obtained without applying the electric field (Poole-Frenkel field) and no leakage current in the reverse bias have been recorded. In order to have a good fit to the theoretical value using the standard dielectric constant of α-MoO_3 at higher frequency, the simulation of the I-V characteristics in this higher applied voltage region is found to be needed [8].

In order to extract the values of the trap level energy and the lowered barrier height of the as-prepared vertically aligned α-MoO_3 nanoblades on FTO substrates, the relation between $\ln(I/V)$ and $1/T$ has been plotted as can be seen in Fig. 6.8.

Additionally, the extracted trap level energy from the Arrhenius plot using Eq. (6.1) and Eq. (6.5) in this region of the applied field is given in Fig. 6.9 (a-e). The obtained values are similar to the ones obtained in the lower applied voltage region (Fig. 6.10).

This confirms the shallowest nature of the trap level, which supports our own suggestions and trap level energies given previously by a theoretical study [30]. Hence our oxygen deficiencies are

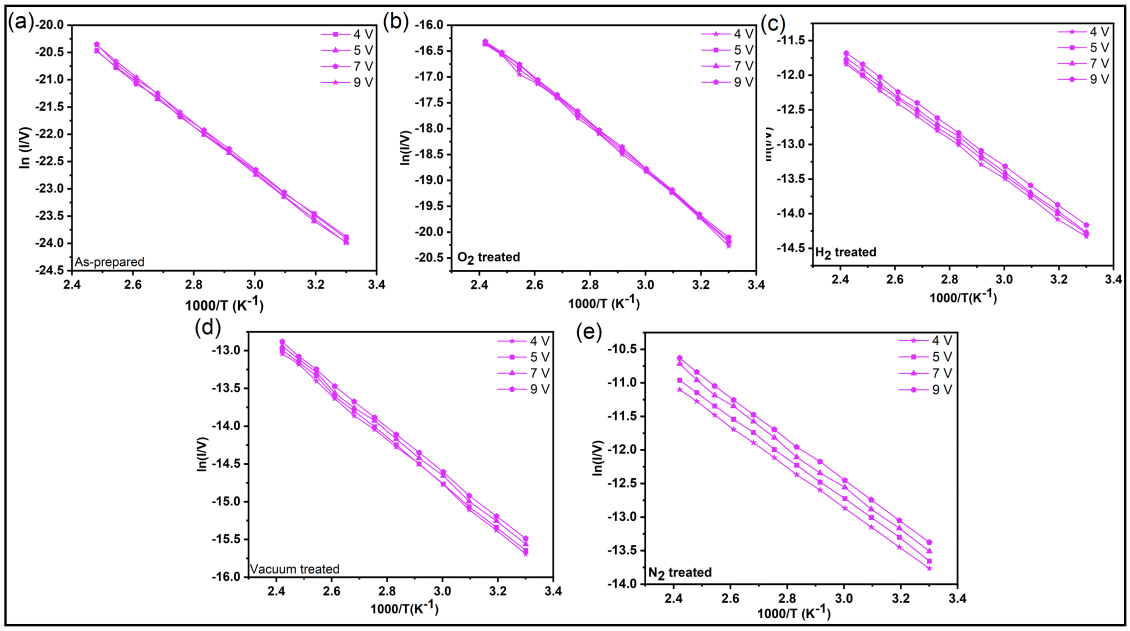

Figure 6.8: (a-e) $\ln(I/V)$ versus $1000/T$ in the high applied voltage area and in the temperature range of 303 – 403 K for as-prepared vertically aligned α-MoO_3 nanoblades on FTO substrates.

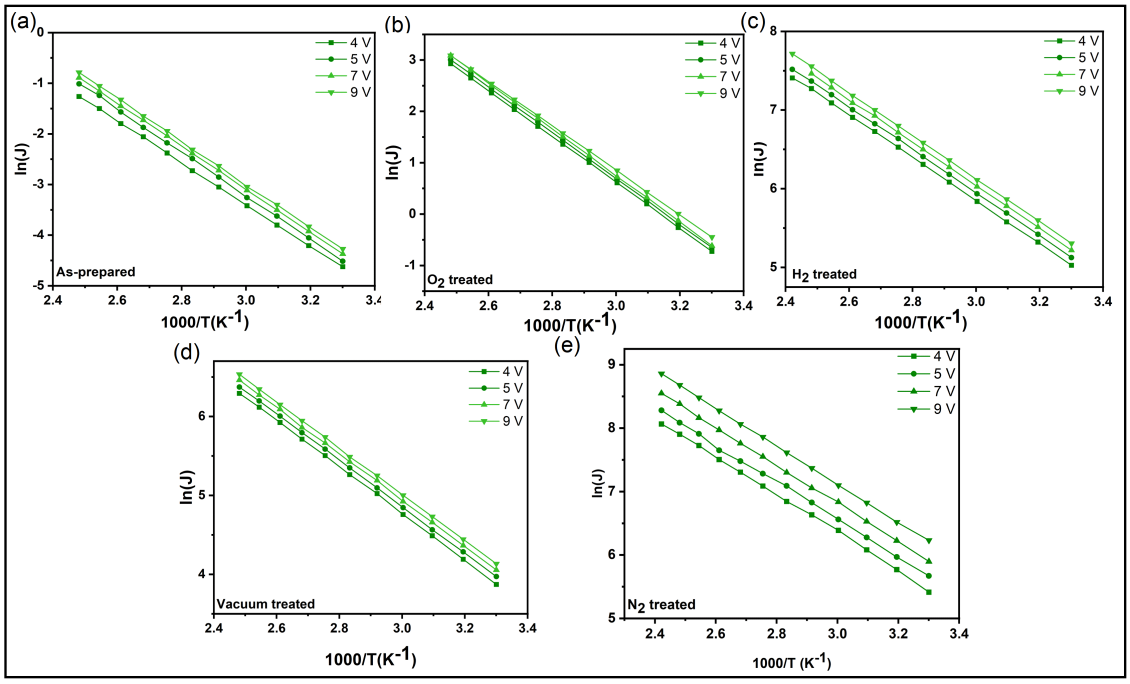

Figure 6.9: (a-e) Arrhenius plots $\ln(J)$ versus $1000/T$ in the high applied voltage area and in the temperature range of 303 – 403 K for as-prepared vertically aligned α-MoO_3 nanoblades/Au on FTO substrates.

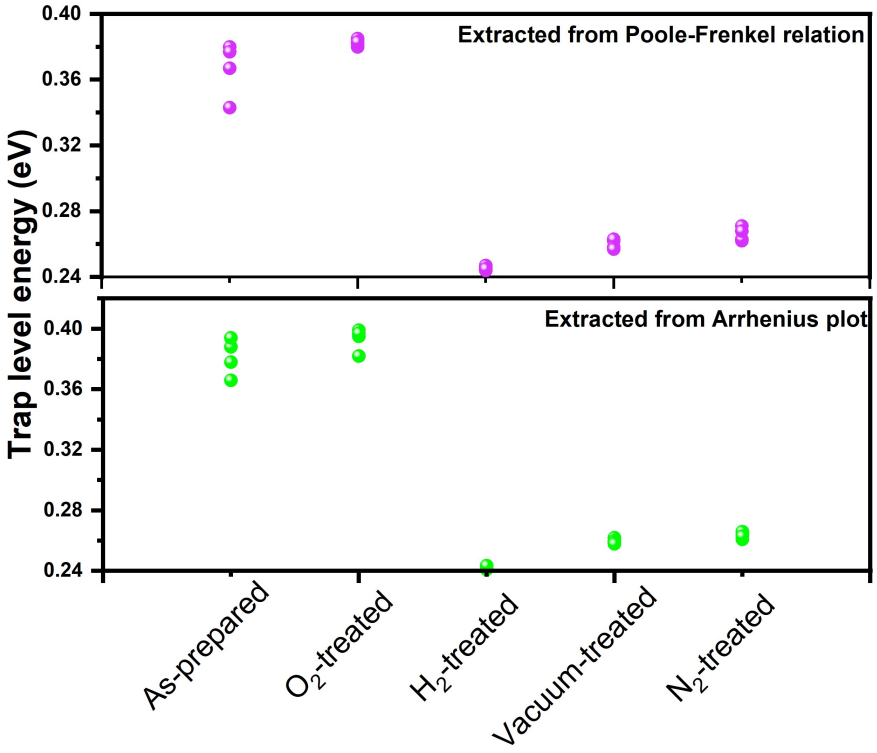

Figure 6.10: (a) Obtained activation energies for as-prepared vertically aligned α-MoO_3 nanoblades as well as for oxidized and reduced α-MoO_3 nanoblades/Au films *via* Poole-Frenkel and Arrhenius relation.

found to dominate intra-bilayers as has been discussed in the XRD analysis (see section 4.5.1). The general activation energies obtained in our study tie well with the intensive study given earlier by Deb *et al.* [180].

The results of our analysis leads us to the conclusion that we are able to alter the electrical conductivity of our α-MoO_3 vertically aligned nanoblades, from a lower conductive state for oxidized films treated under O_2 rich atmosphere, to a higher conductive state obtained by treating the films under reducing atmospheres (H_2, vacuum, N_2), as in n-type semiconductors. The reduced vertically aligned nanoblades showed higher conductivity than the oxidized nanoblades by around 100 times.

The symmetric behavior of the I-V characteristics confirm that the current transport is dominated by a bulk conduction mechanism for all conditions. Our data indicate that in the lower applied voltage region the ohmic conduction mechanism is dominant. On the other hand, in the higher applied voltage region the Poole-Frenkel conduction mechanism seems to be more important.

The activation energies show similar values in both applied field regions, which are dominated by the metal oxide trap levels. The trap levels act as centers for the conduction. The higher activation energies in the as-prepared films may be attributed to some synthesis contamination.

On the other hand, the activation energy of oxidized films (slightly higher) shows a consistent trend with previously reported theoretical calculations, where the oxygen vacancies tend to move in a zig-zag path within the bi-layer. The lower values of the activation energies in the reduced samples suggest that the oxygen vacancies are introduced and moved in two directions (x-,z-) planes as given by Ding *et al.* [30].

7. Possible Applications of α-MoO_3 Nanoblades

7.1 Chemical sensor application

7.1.1 Overview

Metal oxides are widely applied to achieve a superior sensitivity in gas detection application such as ethanol, carbon mono-and dioxide, nitrogen mono-and dioxide, and other hazard gases (target gases). Moreover, the unique properties of the nanomaterials are a suitable candidate for sensitive detection of chemical and biological species, because they exhibit great adsorption activity due to the large surface area [181].

A sensing device consists of two components: Receptor and transducer. The receptor is the metal oxide layer, which interacts with the target gas, whereas the transducer is the component, which transfers this interaction to a signal (through an electrical metal electrode). A chemical sensor is a chemiresistive device configuration, which provides a signal in a form of change in the resistivity or in the conductivity. Changes in the conductivity occur due to exposure to different gases with different concentration in humid and non-humid atmospheres [90].

In order to synthesize a sensor device, different techniques have recently been used and developed to obtain smart nanomaterial morphologies. These techniques include slurry deposition, spin coating and dielectricophoretic positioning, screen printing and ink-jet printing, near field electrospinning, flame spray pyrolysis, sputtering, e-beam evaporation, atomic layer deposition, pulsed laser deposition and glancing angle deposition. (More information can be found in [90].)

The sensor device can be classified by various parameters such as the sensor working temperature, stability beside the life-time, selectivity to a certain kind of gas, sensitivity with a detectable signal and production cost of the sensor device.

7.1.2 α-MoO_3 used as a receptor material

In α-MoO_3 as n-type material, the resistance decreases if the material has been exposed to a reducing agent and *vice versa* with oxidizing agent exposure. Besides, the previously mentioned different oxidation states and higher electronegativity can be favorable properties for sensor devices, as there properties mark a highly reactive material.

Various studies showed the great possibilities of α-MoO_3 nanomaterials to obtain optimized professional sensor device [40, 182]. In comparison with bulk films, well-ordered vertically grown nanowires on template [89], and a network of randomly spread nanowires using drop-casting [183] or vacuum filtration methods [10] on the pre-patterned substrates were found to provide better performance in the gas sensor device (see Fig. 7.1) .

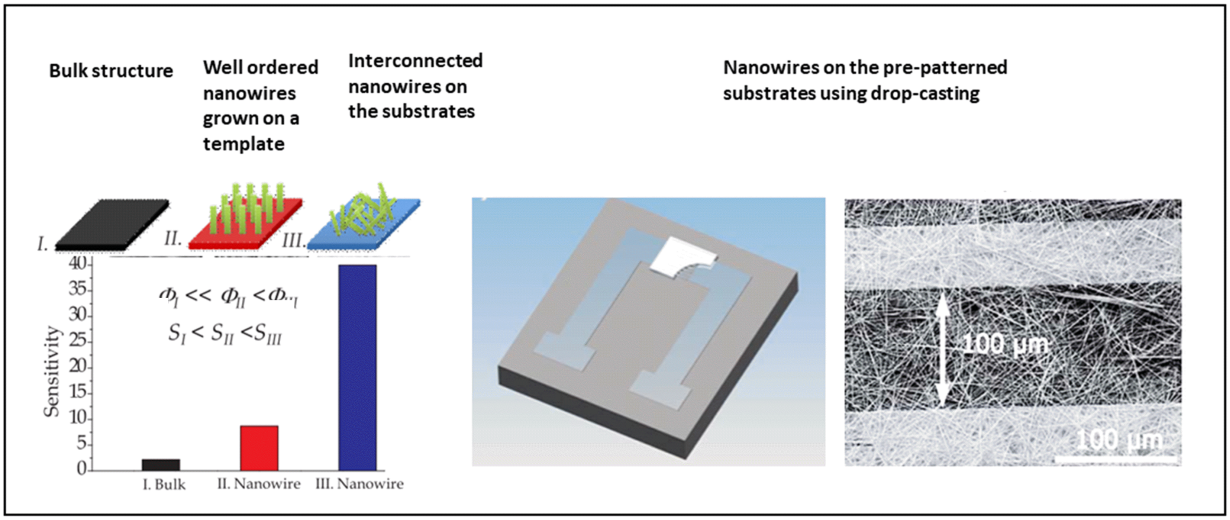

Figure 7.1: Schematic illustration that shows the influence of morphological engineering on the sensing performance, "from [9, 10]".

Therefore, our aim was to provide a proof of concept, that such a device morphology is able to offer excellent sensing performance [9]. Working temperatures of 100 and 200 °C have been applied to study the sensing properties. This provides a preliminary study on the vertically aligned nanoblades on FTO substrates using top coplanar electrodes (6.1 (d)), which have not been intensively addressed yet.

7.1.3 Working mechanism

The decisive mechanism of gas-metal oxide sensors is very controversial [39]. However, the conventional depletion layer model is the widely used [89].

In the standard depletion layer model, it is assumed that all kinds of receptors consist of large grains for bulk films and small grains for nanomaterials. The interaction between the reduced gas and the adsorbed oxygen ions on the surface of the n-type material (our case of α-MoO_3) results in returning back the free carriers to the conduction band of α-$MoO_3$and form a narrow depletion region at the surface α-MoO_3 [181].

On the contrary, for oxidizing gases, the depletion region on the surface of α-MoO_3 is found to be wide due to electron attraction by the adsorbed gas species. This interaction leads to a decrease in the free carrier concentration in the conduction band (see Fig. 7.2).

These influences of the gases can be seen as a form of tuning the electrical conductivity from lower to higher values corresponding to oxidizing and reducing gases, respectively. Hence, this model suggests that there are adsorbed oxygen molecules from the atmosphere on the surface of the metal oxide. The adsorbed species form by attracting electrons from the metal oxide's conduction band. Two types of reactions between the metal oxide's surface and atmospheric oxygen can occur, physisorption and chemisorption reaction as a weak van der Waals force and strong chemical bond, respectively. These reactions depend strongly on the working temperature of the sensor device as given in form of the following relations [9, 89]:

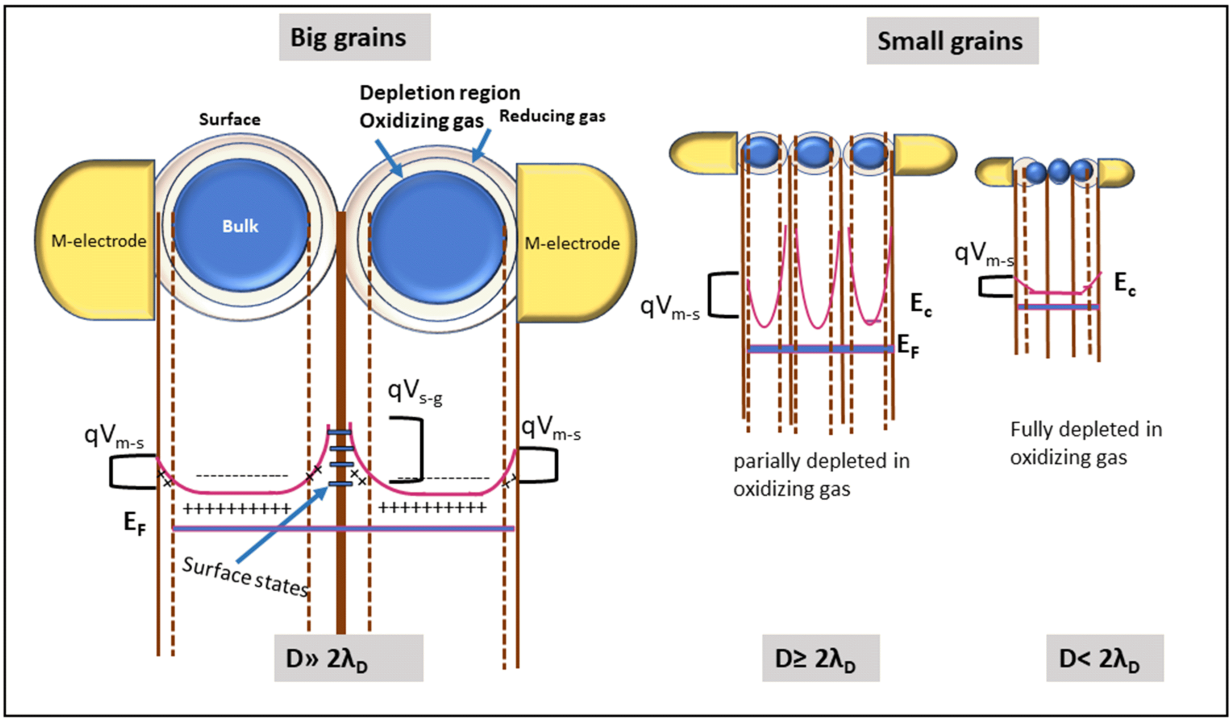

Figure 7.2: Schematic illustration of depletion layer model and nick model for large and small grains, respectively "after [188]".

$$\mathrm{O_{2\,(adsorbed)}} + \mathrm{e^-_{(surface)}} \Leftrightarrow \mathrm{O^-_{2\,(adsorbed)}} \qquad (< 100\,^{\circ}\mathrm{C} - \text{physisorption}) \tag{7.1}$$

$$\mathrm{O_{2\,(adsorbed)}} + 2\,\mathrm{e^-_{(surface)}} \Leftrightarrow 2\,\mathrm{O^-_{(adsorbed)}} \qquad (100 - 300\,^{\circ}\mathrm{C} - \text{chemisorption}) \tag{7.2}$$

$$\mathrm{O^-_{(adsorbed)}} + \mathrm{e^-_{(surface)}} \Leftrightarrow \mathrm{O^{2-}_{(adsorbed)}} \qquad (> 300\,^{\circ}\mathrm{C} - \text{chemisorption}) \tag{7.3}$$

where the target gas X ('gas-in' period) reacts with adsorbed ions on the surface according to the following relation [9]:

$$\mathrm{O^-_{2(adsorbed)}} + X'_{\mathrm{gas,\,in}} \rightarrow X_{\mathrm{gas,\,out}} + \mathrm{e^-} \tag{7.4}$$

At the terminals (M-electrodes), a fixed independent barrier height forms as a result of the metal/semiconductor junction. It is given as ($\mathrm{eV_{m-s}}$) as we can see in Fig. 7.2. Whereas, another barrier height of ($\mathrm{eV_{s-g}}$) can be formed between the grains as a result of an interaction between the grain surface and the surrounding target gas. It is known as barrier height at the grain boundaries [184].

A well-defined semiquantitative model, given by Xu *et al.* [185] for nanomaterials, states the relation between the grain size, width (W) of the depletion region, and the sensitivity (S) through the following relations [89, 91, 185]:

$$\lambda_D = \left(\frac{\epsilon k_{\mathrm{B}} T}{e^2\, n_{\mathrm{b}}}\right)^{\frac{1}{2}} \tag{7.5}$$

$$W = 2\,\lambda_{\mathrm{D}} \left(\frac{\mathrm{eV_{s-g}}}{k_{\mathrm{B}} T} \right)^{\frac{1}{2}} \tag{7.6}$$

$$\mathrm{eV_{s-g}} = \frac{e\,n_{\mathrm{s}}^2}{2\epsilon\,n_{\mathrm{b}}} \tag{7.7}$$

$$S = \frac{R_{\mathrm{a}}}{R_{\mathrm{g}}} = \left\{ (1-x)^2 + \frac{n_{\mathrm{s}}}{n_{\mathrm{b}}} \left[1 - (1-x)^2 \right] \right\}^{-1} \tag{7.8}$$

where λ_{D} is Debye length as material character, n_{b} is the free carrier concentration of the material (bulk as can be seen in Fig. 7.2), n_{s} is the carrier concentration of the charges attached to the surface of the metal oxide grains (bound to the depletion region as surface states), R_{a} is the initial resistance in air, and R_{g} is the resistance under gas exposure. Whereas, x is a factor related to the grain size through the relation $x = 2\lambda_{\mathrm{D}}/rD$, where D is the grain diameter or size and r is a constant.

- We can deduce from these equations that the widest space charge region, which dominates the whole grains, can be formed when $D < 2\lambda_{\mathrm{D}}$. In this case, no significant barrier height can be obtained between the small grains at a certain temperature, which is known as fully depleted grains. Therefore, the highest sensitive performance can be obtained [185]. Hence, the reaction between oxidizing and reducing atmospheres and the nanometal oxides causes noticeable changes in the resistance even for a short exposure time to these atmospheres.

- In case of $D \gg 2\lambda_{\mathrm{D}}$, the total resistance of the device is controlled by the inner or bulk carrier concentration. Therefore, it is less sensitive to the interacted carriers at the surface.

- For $D \geq 2\lambda_{\mathrm{D}}$, the space charge region shows neck-like conduction channels around each grain. Therefore, the resistance shows dependence not only on the grain boundaries, but also on the cross section area of every conduction channel around the grains. This leads to better sensitivity [186].

The metal-semiconductor junction barrier height ($\mathrm{eV_{m-s}}$) for all cases is independent from the sensitive performance. However, the electrode material must be highly stable, do not diffuse into the semiconductor at high temperature, do not form an oxide layer in the interface, and do not corrode due to exposure to the target gases, because this could reduce the conductivity of our sensor device. For more information see [187].

The disadvantages of Xu's model are: (1) The only valuable interaction between the target gas and the surface of the metal oxide takes a place at high temperatures due to adsorbed oxygen species from the atmosphere and attract free charges near the surface of the material (change the electrical conductivity). (2) The reaction between the target gas and the surface of the metal oxide at room temperature is a weak physisorption reaction, which leads to a flat band formation (no influence on the electrical conductivity) [188].

These suggestions by Xu's model are contradictory to the nature of metal oxides, which are highly sensitive to atmosphere. Many studies have proven that α-MoO_3 forms a very thin oxide layer on the surface due to exposure to ambient conditions (room temperature) [4,189]. This effect can be observed as a reduction in the work function of the material [190] and an increase in the Mo^{5+} concentration as shown by XPS analysis by M. T. Greiner *et al.* [73]. Nonetheless, the study by Andreas Borgschulte *et al.* [120] showed that the exposure to H_2 rich atmosphere at room

temperature causes an intercalation process of H_2 ions in the crystal and a fast reduction of Mo^{6+} to Mo^{5+}.

Therefore, contrary to the depletion layer model, Oxygen vacancies can be produced in the bulk not only on the surface of the material due to a reconstruction of the crystal oxygen, which can be understood as color center formation and polaron migration processes (see sections 2.6.1-2.6.3) [21]. This was recently confirmed by DFT and vdW-DFT calculations [7, 30]. The rate of the oxygen vacancies depends on the temperature and the exposure time in a linear proportional manner. These processes take place at the same time as the exposure to the target gas ('gas-in' stage) and the carrying gas (air- 'gas-out' stage). Therefore, When the target gas is removed and the sample is exposed to the carrying gas (air- 'gas-out' period), the oxygen-rich conditions lead to re-adsorption of oxygen at the surface, but it clearly requires more time than expected to fully heal the oxygen deficiencies during the 'gas out' stage.

7.1.4 Vertically aligned α-MoO_3 nanoblades as a CO gas sensor

Vertically aligned α-MoO_3 nanoblades on FTO substrates have been utilized to a gas sensor chamber at working temperatures of 100 and 200 °C. The electrode configuration was designed to be a co-planar configuration and is shown in Fig. 6.1 (d). Carbon monoxide (CO) (100 %) consecutively with dry air have been used as a target gas to test the sensitivity of our structure, where the latter gas is usually used as a carrying gas.

CO is a toxic gas and an environmental pollutant. The detection of CO gas is highly demanded for industrial safety environmental control, because it is generated during combustion process in engines, stoves, water, heaters, generators and lanterns [191]. CO is a colorless and tasteless gas that leads to severe human health problems in the human organism [191].

CO acts as a reducing agent that leads to an increase in the electron concentration when interacting with the nanoblades surface. When α-MoO_3 is thermally treated, oxygen vacancies and polaron migration can occur as has been discussed in our study and in previously reported studies [53, 192, 193].

Fig. 7.3 (a) shows the oxygen vacancy formation and diffusion through the surface, where additionally adsorbed oxygen ions attract electrons from the surface. This behavior is described by the relations in Eq. 7.1. As soon as the target is exposed to the CO gas, it interacts with the adsorbed oxygen ions and releases back free electrons. This leads to an increase in the free carrier concentration and in the conductivity, as can be seen in the following relations [181]:

$$CO_{(gas)} \rightarrow CO_{(adsorbed)} \tag{7.9}$$

$$2\,CO_{(adsorbed)} + O_2^- \rightarrow 2\,CO_{2\,(gas)} + e^- \qquad (< 100\,^{o}C) \tag{7.10}$$

$$CO_{(adsorbed)} + O^-_{(adsorbed)} \rightarrow CO_{2\,(gas)} + e^- \qquad (100 - 300\,^{o}C) \tag{7.11}$$

$$CO_{(adsorbed)} + O^{2-} \rightarrow CO_{2\,(gas)} + 2\,e^- \qquad (< 300\,^{o}C) \tag{7.12}$$

The gas sensing experiments were carried out at working temperatures of 100 and 200 °C, where the atmosphere was changed every 50 s (dry air and CO consecutively) at a constant applied voltage and gas flow rate of 2 V and 500 mL/min, respectively. As depicted in Fig. 7.3 (b), vertically aligned α-MoO_3 nanoblades show a rather fast response to CO gas.

Researchers commonly evaluate the sensitivity as the ratio of the changes of the resistance ($R_a - R_g$) to the resistance in gas (R_g) as follows [39]:

$$S = \frac{\Delta R}{R_g} = \frac{R_a - R_g}{R_g} \tag{7.13}$$

The sensitivity has been calculated for the two sensor working temperatures of 100 and 200 °C and are found to be $(25 \pm 7)\,\%$ and $(51 \pm 2)\,\%$, respectively. Fig. 7.4 shows a fast response to the target gas exposure within a time of ≈ 10 seconds. Here it is worth to notice that, the fluctuation in the sensing curve was caused by suboptimal closing of the valves during the measurement (gas on-gas off). Furthermore, it gives a clear proof in favor of our criticism to the depletion layer model, that a long time is needed to fully depleted the structure (bulk and surface) during the 'gas-out' stage and rich the highest possible current flow during CO 'gas-in' stage.

Our vertically aligned α-MoO_3 nanoblades show a higher sensitivity and faster response in comparison to previously reported gas sensing performances [194, 195]. The higher performance can be attributed to the nature of our nanoblades, which presents a higher surface area. Besides, the interconnected structure facilitates the movement of charges, which is consistent with our electrical measurements. See Table 6.3.1.

Future investigations on the vertically aligned α-MoO_3 grown directly on different substrates could associate the higher sensitivity performance and low working temperature. Therefore, further work is certainly needed to disentangle the complexities of applying a vertically aligned α-MoO_3 nanostructure with top electrodes for modified sensor devices.

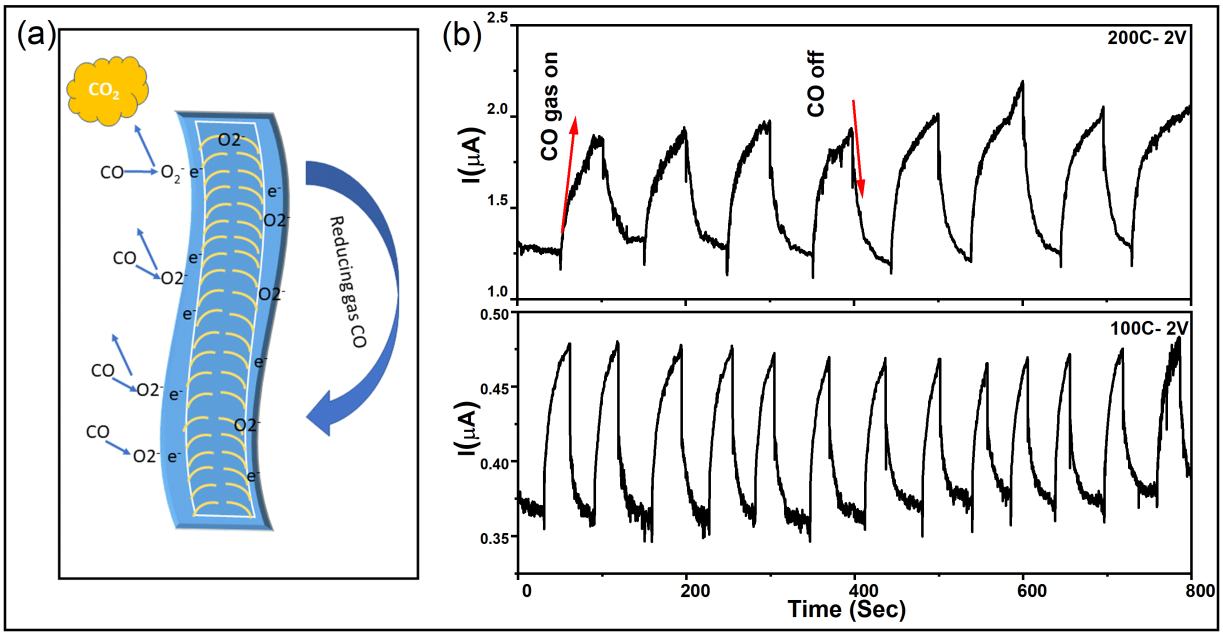

Figure 7.3: (a) Schematic illustration of the interaction between the vertically aligned α-MoO_3 nanoblades with CO gas. (b) Current versus time (air and CO gas consecutively exposure) at a working temperatures of 100 and 200 °C and a constant applied voltage of 2 V.

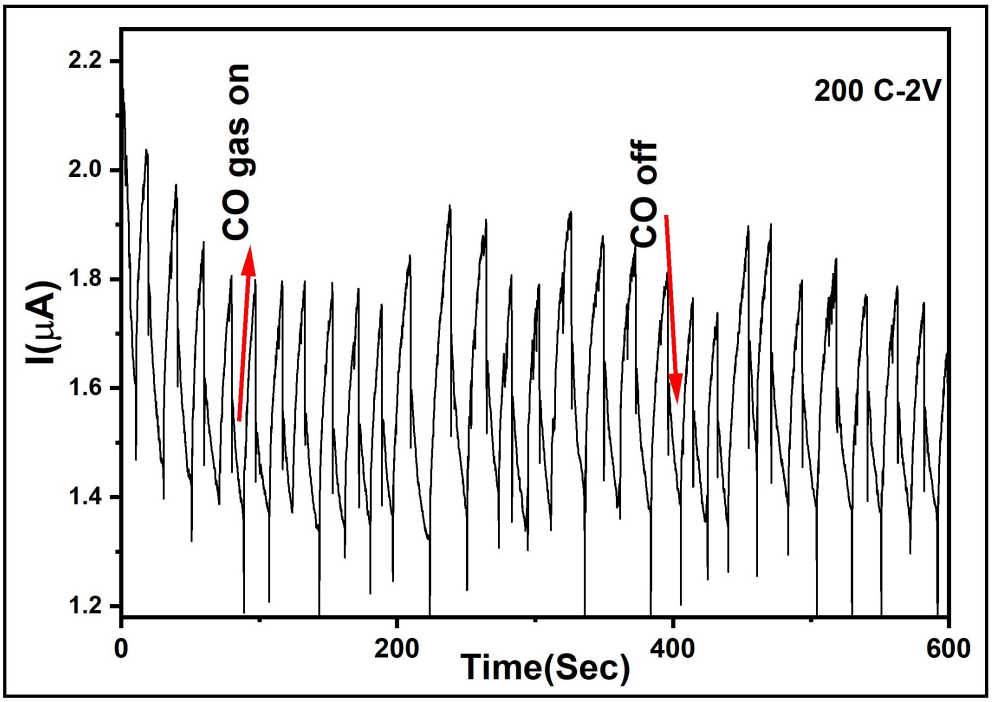

Figure 7.4: Current versus exposure time of ≈ 10 seconds to air and CO gas consecutively at 200 °C at a constant applied voltage of 2 V.

7.2 Supercapacitor application

7.2.1 Overview

[1]Recent development in the field of hybrid electric vehicles and portable electronic devices led to considerable attention for the design of high-performance eco-energy storage devices such as supercapacitors [34, 196]. Supercapacitors are crossing-bridge devices between conventional capacitors and rechargeable batteries owing to their high power density (> 500 Wkg^{-1}), a long cycling life ($> 10^5$ cycles), and stability in comparison to batteries [197, 198].

The charge storage mechanism of supercapacitors can be classified into two types, namely electrical double layer capacitors (EDLCs; non-faradaic) and pseudocapacitors (faradaic). Carbon-based materials are extensively used in EDLCs, which exhibit charge accumulation at the interface between electrode and electrolyte. In pseudocapacitors, on the contrary, faradaic redox reactions happen at the electrode surface [199]. Combining the fast and reversible faradaic processes along with non-faradaic electric double layer formation allows for a higher storage capacity of pseudocapacitors. This process shows that charging is not limited by bulk ion diffusion as it is in batteries [200].

Transition metal oxides, hydroxides and conductive polymers are most widely used as pseudocapacitive electrode materials. However, the poor electrical conductivities and slower faradaic reaction kinetics hinder their performance at high current densities [201].

α-MoO_3 has been reported to have a high theoretical specific capacitance of 1111 $mAhg^{-1}$ [202], in comparison to a graphite capacitance of 372 $mAhg^{-1}$ [203]. The main limitations of using α-MoO_3 as electrode material are the low electrical conductivity and the big loss in the capacity during the initial cycles [202].

Different strategies can be used to overcome those issues. Variety of the oxidation states is related to the oxygen deficiency in the crystals, which plays a significant role in tuning the conductivity and enhancing the electrochemical activity [34]. Moreover, morphological engineering such as interconnected arrays of the binder free metal oxide nanostructures grown on conductive substrates, leads to an enhancement in the charge/ion transport and electrochemical activity [198]. Additionally, α-MoO_3 hybridized with carbon materials reveals an enhancement in the stability, thermal and electrical conductivity, and device performance [29, 34, 196].

Hydrothermal carbonization as a stand-alone process with different starting raw materials for development of activated carbon material with different porosities has been intensively reported to have high chemical activation ability [204, 205]. The hydrothermal carbon has been functionalized and applied in different applications such as water treatment, catalysis, agricultural uses, and in energy storage applications as in supercapacitors [206].

In our current study, we initiated a strategy to prepare carbon coated vertically aligned nanostructure films independently from the hydrothermal reaction followed by thermal treatment, to avoid inadequate substances and inefficient material growth mechanisms. To the best of our knowledge, the performance of hybrid binder free carbon coated reduced vertically aligned α-MoO_3 nanoblades as electrode structure in supercapacitors has not been intensively addressed in the literature.

In this study, a feasible procedure has been proposed to prepare hybrid carbonized vertically aligned α-MoO_3 nanoblades by decomposition of glucose as a carbohydrate on the annealed vertically aligned α-MoO_3 nanoblades under reducing conditions (H_2, N_2, vacuum) on FTO substrates.

[1]Sections 2.2.1-2.2.4 were written by me and revised by Dr. R. Ananthakumar.

7.2.2 Carbonization procedure of reduced vertically aligned α-MoO_3 nanoblades on FTO substrates

The carbonization process has been executed by placing the reduced vertically aligned α-MoO_3 nanoblades on FTO in a solution of 1 M concentration of glucose (99.5 %, Sigma Aldrich) in acetic acid ($\geq$ 99.7 %, Sigma Aldrich) for 12 h. Following this, the substrates were heated up to 450 °C for 1 h in Ar atmosphere in a digital controlled oven with a heating rate of 10 K/min, as can be seen in Fig. 7.5.

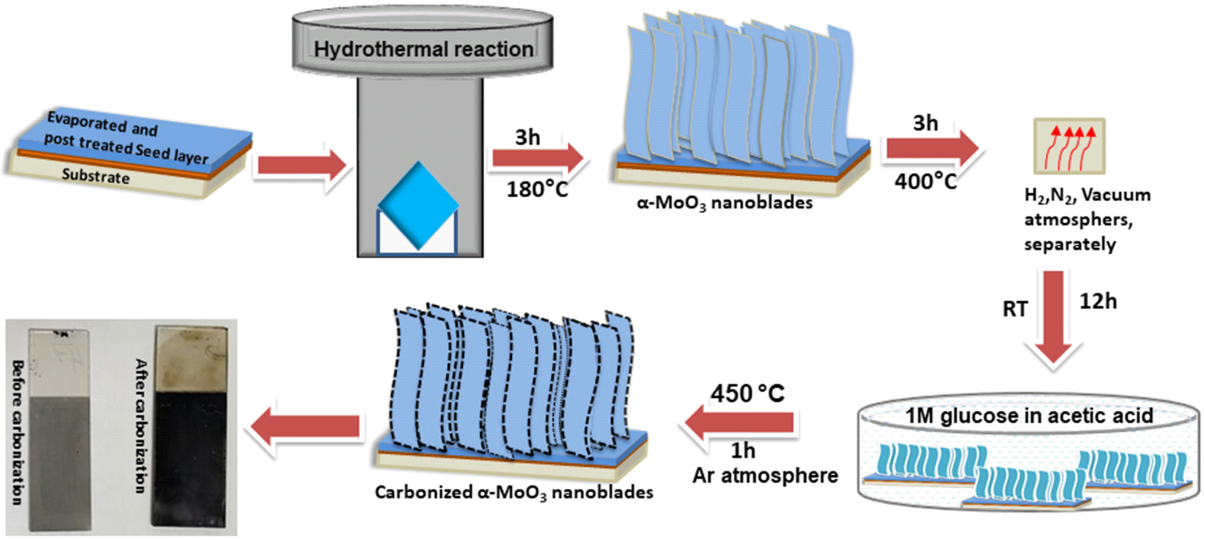

Figure 7.5: Schematic of the preparation procedure of carbon coated reduced vertically aligned α-MoO_3 nanoblades on FTO substrates.

It is worth to mention that, glucose is not only needed for the carbonization process in order to obtain hybrid carbonized α-MoO_3 nanoblades, but also plays a crucial role by stabilizing the nanoblades as a binding material on the substrates, making them suitable for aqueous electrolyte cells [207].

The binder free method eliminates the implications of unnecessary use of non-conducting binders. Furthermore, the carbon coating on α-MoO_3 nanoblades is able to act as a conducting agent, which significantly enriches the electrical conductivity of the hybrid structure. Hence, it provides firm attachment between the active material and the substrate. This leads to good electrode/electrolyte interaction, a low diffusion ion path length, low material degradation, and high electrical conductivity [208–210].

7.2.3 Structural characterization of carbonized reduced vertically aligned α-MoO_3 nanoblades

As can be seen from Fig. 7.6, the carbon coated reduced vertically aligned α-MoO_3 nanoblades show no change in the morphology of the nanoblades after the carbonization process in comparison to the un-carbonized structure (see Fig. 4.16). However, in a higher magnification FE-SEM picture (Fig. 7.6 (d)) the nanoblades appear to be covered with very thin 2D sheets, which suggests the formation of a porous carbon layer, in addition to the color conversion to dark black after the carbonization process in Fig. 7.5. An elemental mapping analysis *via* energy-dispersive X-ray spectroscopy (EDS) of the carbonized interconnected reduced vertically aligned α-MoO_3 nanoblades is shown in Fig. 7.7. The films are well carbonized with a homogeneous coverage on the nanoblades surface. A single nanoblade in Fig. 7.8 shows a high intensity of the element carbon (C).

Carbonization of the vertically aligned α-MoO_3 nanoblades is produced *via* decomposition of glucose material as a carbohydrate compound in acetic acid (organic solvent) [211]. Our observation from Fig. 7.6 (d) conforms with previous results of the carbonization at high temperatures using glucose and demonstrates a porous structure of the carbon layer, which has been found to be attached to the α-MoO_3 nanoblades. Furthermore, the effect of using acetic acid promotes the dehydration process extensively, which leads to the production of activated carbons [206].

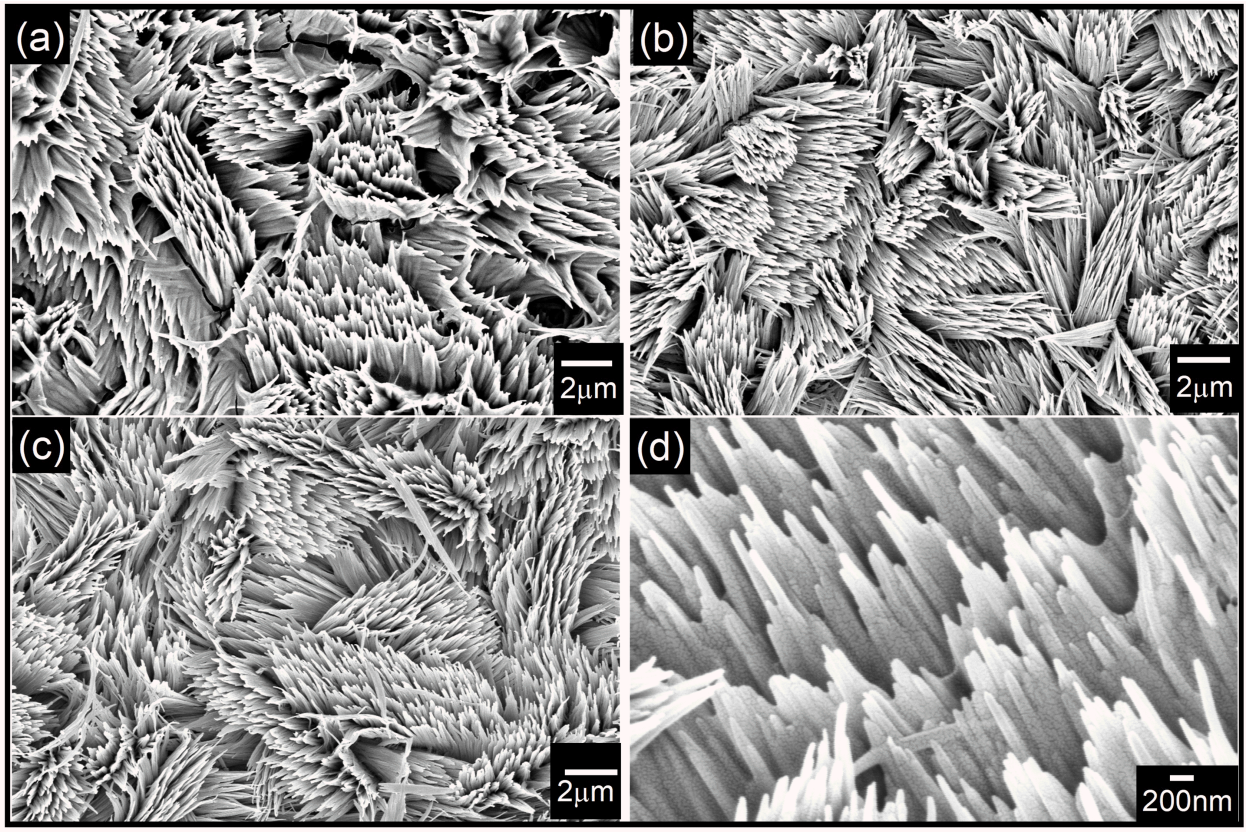

Figure 7.6: (a-c) FE-SEM micrographs show the carbon coated reduced vertically aligned α-MoO_3 nanoblades on FTO substrates, reduced under H_2, N_2, and vacuum, respectively. (d) A higher magnification FE-SEM shows that a very thin porous layer of carbon covers the nanoblades.

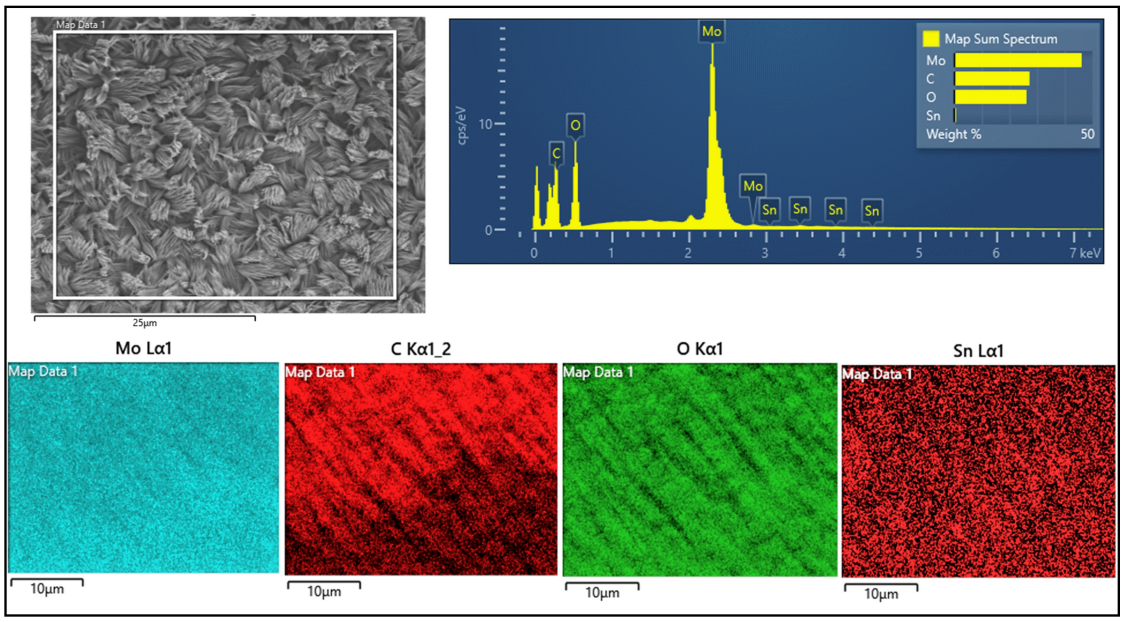

Figure 7.7: EDS mapping and spectrum of carbon coated reduced vertically aligned α-MoO_3 nanoblades on FTO substrates.

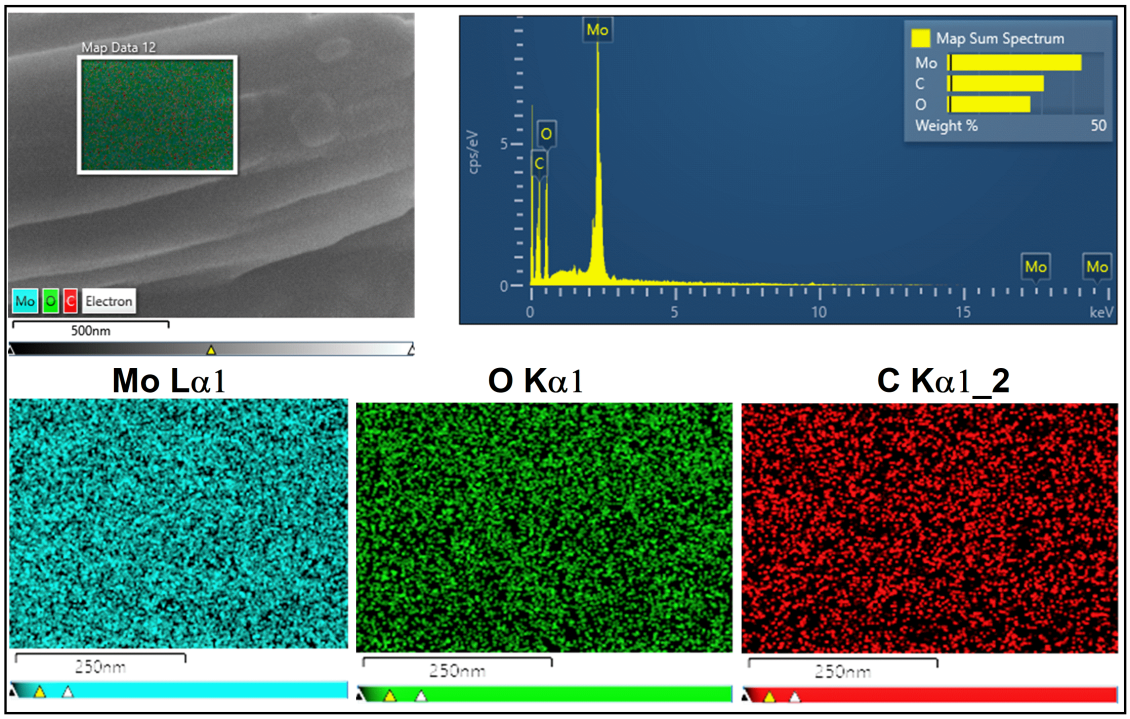

Figure 7.8: EDS mapping and spectrum of a single carbon coated reduced α-MoO_3 nanoblade.

The XRD diffraction patterns in Fig. 7.9 (a) exhibit three well marked diffraction peaks at 2θ around 12.7°, 25.7° and 38.9°. These peaks can be indexed to the orthorhombic crystal planes (020), (040) and (060) of carbon coated vertically aligned α-MoO_3 nanoblades in consistency with JCPDS 00-005-508, space group *pbnm*.

The absence of some peaks (un-carbonized films see Fig. 4.18) may be due to a thicker coverage of the embedded structure in a porous graphitic carbon layer. The broad peak at 2θ around 26.1° (Fig. 7.9 (b)) is associated with the characteristic peak of the (002) plane in hexagonal graphite (JCPDS 65-6212). This broad peak suggests the formation of reduced graphene oxide (rGO) with amorphous features, since the peak around 11.5° corresponding to graphene oxide is missing [212–214].

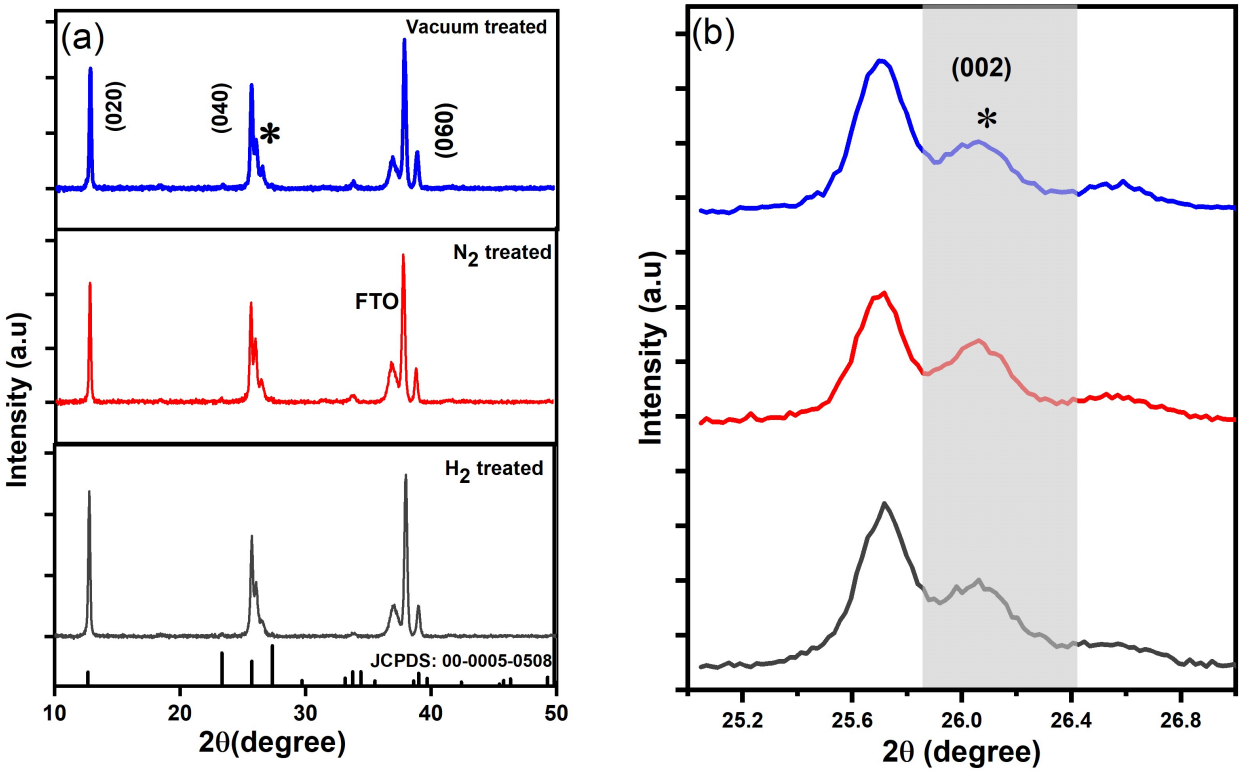

Figure 7.9: (a) XRD diffraction patterns of carbonized reduced vertically aligned α-MoO_3 nanoblades on FTO substrates (orthorhombic, JCPDS card 00-0005-0508). (b) Indication ($*$) of broad graphitic carbon diffraction pattern.

Raman spectra[2] (Fig. 7.10) of the carbon coated reduced vertically aligned α-MoO_3 nanoblades on FTO substrates show characteristic peaks of orthorhombic α-MoO_3 [215]. These are consistent with our non-carbonized reduced vertically aligned α-MoO_3 nanoblades on FTO (see Fig. 4.7).

The characteristic peaks around 1366 and 1600 cm^{-1} correspond to D and G bands, which confirms a carbonized hybrid structure. The D band is related to the disordered structure of sp^3 bonded carbon. The lack of long-range order in amorphous and quasi-crystalline forms of carbon materials allows zone-edge modes to be active.

The G band is related to the stretching mode of sp^2 bonded carbon in the basal plane of

[2]Raman sepectra were recorded by Dr. Peyman Zirak Yousefabadi, analyzed and written by me.

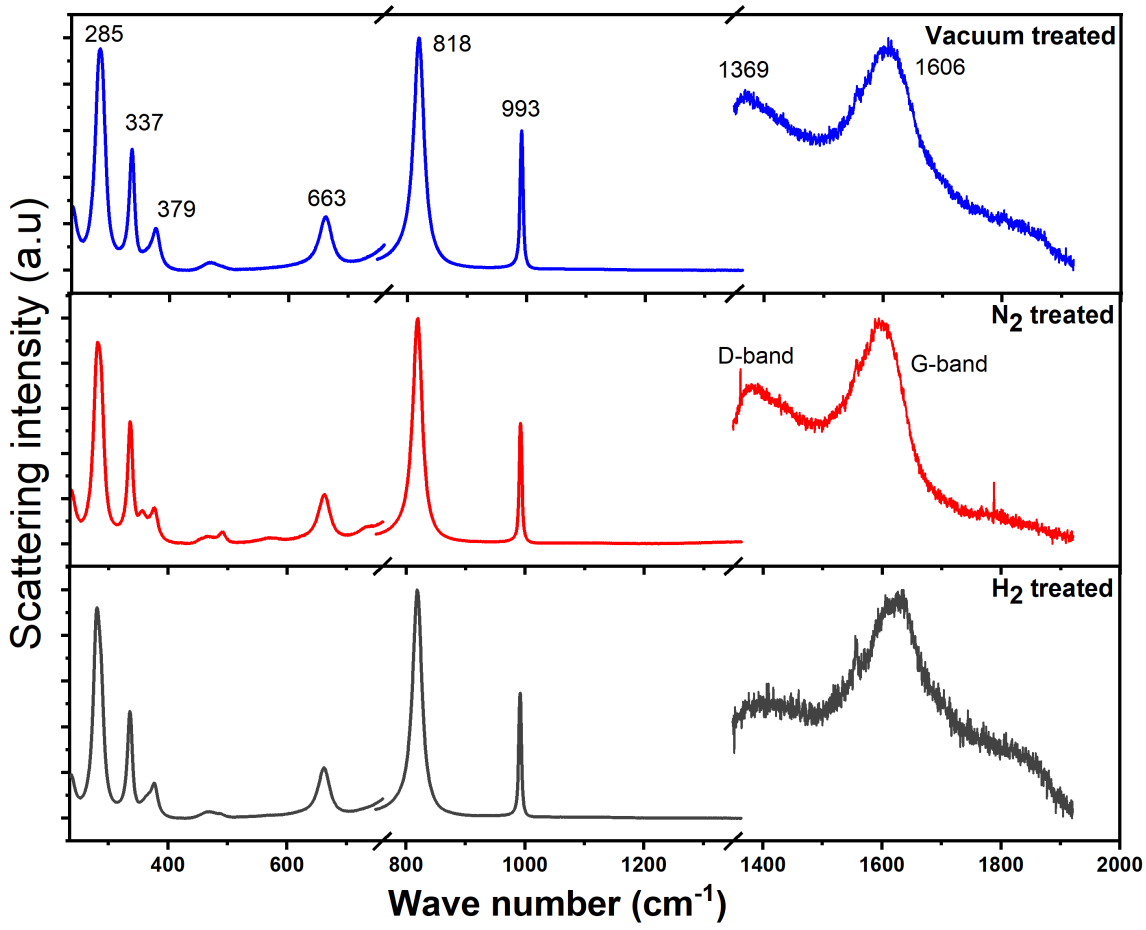

Figure 7.10: Raman spectra of carbon coated reduced vertically aligned α-MoO_3 nanoblades on FTO substrates, recorded using a 488 nm excitation source.

the crystalline graphite. The integral intensity ratio I_D/I_G of carbon coated reduced vertically aligned α-MoO_3 nanoblades is found to be 0.58, 0.7, 0.85 for N_2, H_2 and vacuum treated samples, respectively. The increase in the ratio reflects an increase in defects [216], in favor of the vacuum treated samples. This implies a decrease in the average size of the sp^2 domains and a higher rate of conversion to reduced graphen oxides (rGO) with an amorphous structure. It also suggests that for the hydrogen and N_2 treated samples, more time is needed to dehydrate the glucose and achieve a higher conversion to graphitized rGO [213]. Moreover, since the carbonization process is a dehydration process, we speculate that more time is needed to dehydrate the H_2 treated samples at high temperatures under Ar atmosphere.

7.2.4 Working mechanism

The main components of an industrial capacitor are two metal electrodes with dielectric material placed between them. The charging process of the capacitor is enforced by applying an external potential between the two metal electrodes. As a result, charges are attracted by the electrode of opposite polarity. For the discharging process, the device is connected to a load resistance in order to deliver the stored energy [217].

The capacitance (C) of a capacitor constructed of two parallel plates is calculated according to the following equation [218]:

$$C = \frac{\epsilon A}{d} \qquad [C] = \mathrm{F} = \frac{\mathrm{As}}{\mathrm{V}} \tag{7.14}$$

where ϵ is the absolute permittivity of the dielectric material, A is the area of one plate, and d is the plate distance.

The specific capacitance (C_s) is the capacitance per active area of the material. This quantity offers a better comparison of the capacitance for industrial and applied purposes and is calculated using the following equation:

$$C_\mathrm{s} = \frac{C}{A} \qquad [C_\mathrm{s}] = \mathrm{F\,cm^{-2}} \tag{7.15}$$

Two techniques can be used to evaluate the specific capacitance:

Cyclic voltammetry (CV): A potential is applied to the working electrode with respect to a fixed potential of the reference electrode. The potential range is limited by the electrolyte stability. The current versus the applied potential is recorded in backwards and forwards scanning directions with a certain scan rate (steps of applied potential in a given time). The capacitance is calculated using the following equation [29]:

$$C = \frac{\int I\,dQ}{2\,V_\mathrm{s}\,\Delta Q} \tag{7.16}$$

where $\int I\,dQ$ is the area under the CV curve, V_s is the potential scan rate, and ΔQ is the range of the applied potential. Subsequently, the specific capacitance can be calculated using Eq. 7.14.

Galvanostatic charge–discharge (GCD): In this technique, the working electrode is charged to a certain potential using a constant current density, and the discharge process is recorded as the potential versus the time. For a pseudocapacitor (our case), the capacitance is given by the following equation [217]:

$$C = \frac{\Delta t\,I}{\Delta Q} \tag{7.17}$$

where Δt is the total duration of the discharging process. Eq. 7.14 is used to determine the specific capacitance.

Most supercapacitor materials show non-ideal supercapacitive behavior, which is attributed to the internal resistance. The device resistance is given as the equivalent series resistance (R_ESR), which includes the electrolyte resistance, the active materials, electrode resistance, and other connection resistances of the device. The resistance affects the specific power (P) delivered by the cell as given by the following equation [217]:

$$P = \frac{(\Delta Q)^2}{4AR_{\mathrm{ESR}}} \tag{7.18}$$

Electrical impedance spectroscopy (EIS) is used to determine R_{ESR}. By applying an alternating current with a frequency range of 0.01 Hz – 1 MHz and recording a Nyquist plot of the imaginary resistance (Z'') versus the real resistance (Z'), R_{ESR} can be calculated directly from the interception. Additionally, this measurement gives information about the stability of the capacitors, which can be measured before and after the charging-discharging cycles.

The supercapacitor stability is a very important factor for commercialization the device. In order to test the device stability, 1000 to 10,000 cycles (charging-discharging cycle) at a constant current density are recorded. This stability test offers information about corrosion, degradation and the device life-time. This gives the retention percentage of the capacitance within the cycles and indicates how large the drop of the capacitive performance after a time period of charging-discharging cycles is [217].

7.2.5 Electrochemical characterizations of carbonized reduced vertically aligned α-MoO_3 nanoblades

The electrochemical properties [3] of carbon coated reduced vertically aligned α-MoO_3 nanoblades on FTO substrates were examined by cyclic voltammetry (CV) and galvanostatic charge/discharge (GCD) in 0.5 M Li_2SO_4 electrolyte as a negative electrode. The CV was performed for scan rates from 5 to 125 mVs^{-1} and in the potential window of -0.8 to 0 V. See Fig. 7.11.

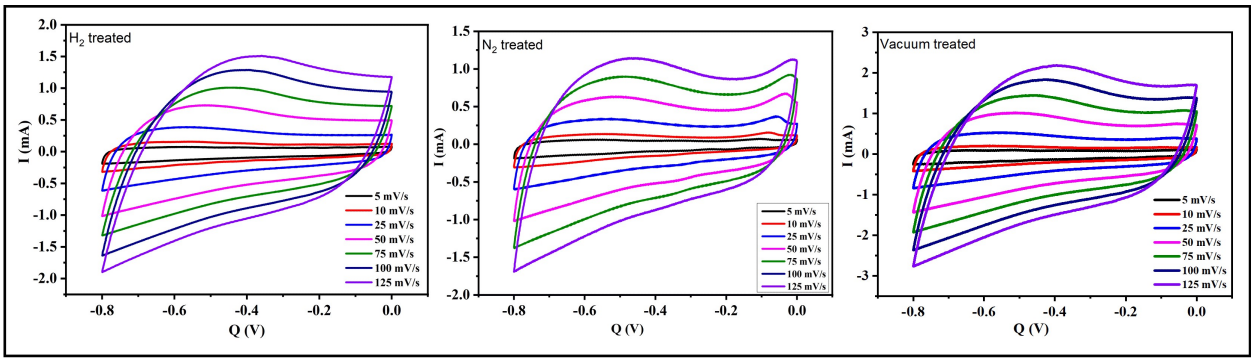

Figure 7.11: (a) CV plots of carbon coated reduced vertically aligned α-MoO_3 nanoblades treated under H_2, N_2, and vacuum, respectively.

All three electrodes showed pseudocapacitive behavior. Fig. 7.12 shows CV plots at a scan rate of 50 mVs^{-1} and GCD plots at a current density of 0.5 $mAcm^{-2}$, as well as the corresponding specific capacitances. The electrochemical performances obtained by CV and GCD show similar trends.

According to the CV plots in Fig. 7.12, carbon coated reduced vertically aligned α-MoO_3 nanoblades exhibit a higher performance for vacuum treated films, followed by N_2 and H_2, respectively. The carbon coated vacuum treated vertically aligned α-MoO_3 nanoblades show reversible faradaic redox peaks, along with a partially rectangular shape (see Fig. 7.11). This behavior is

[3] Section 2.2.5 was written by Ms. Ankita Mohanty, Dr. R. Ananthakumar and me, the measurements, Data plotting and calculation were done by Ms. Ankita Mohanty.

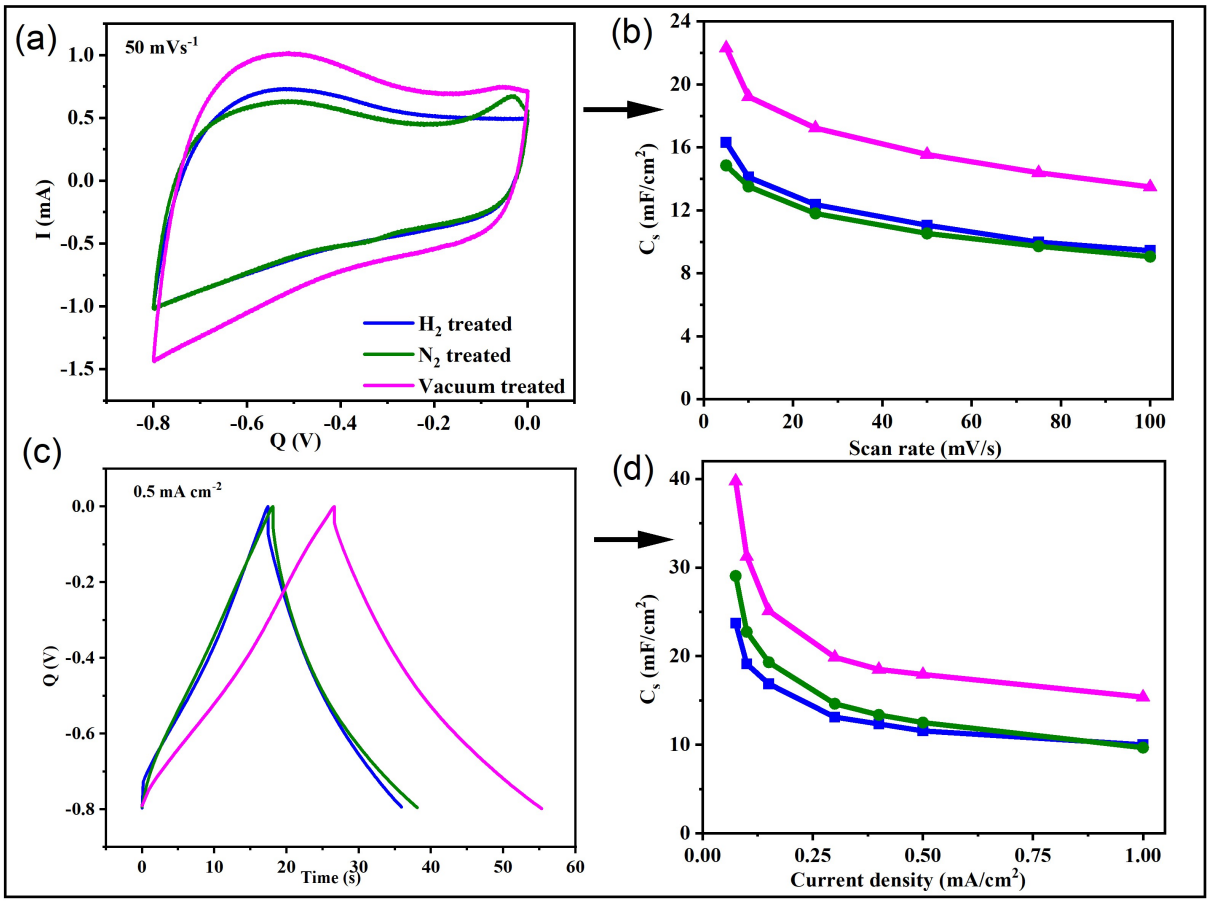

Figure 7.12: (a) CV plots at a scan rate of 50 mVs^{-1} of carbon coated reduced vertically aligned α-MoO_3 nanoblades. (b) Specific capacitance (C_s) versus scan rate calculated from the CV plots. (c) GCD plots at a current density of 0.5 $mAcm^{-2}$. (d) Specific capacitance (C_s) versus current density calculated from the GCD plots.

attributed to the mixed electric double layer capacitance (due to the presence of carbon) and pseudocapacitive behavior (ion intercalation/deintercalation along with redox reaction among Mo^{5+} and Mo^{6+}) [219]. It can also be seen that with an increase in the scan rate, the area of the CV plots is also increasing, which is referring to a good reversibility of the electrode.

As an excellent two-dimensional transition metal oxide, α-MoO_3 holds a magnificent position in the field of electrochemically active materials. The high oxidation states of α-MoO_3 make it feasible for multiple oxidation-reduction processes, leading to great pseudocapacitive behavior [220, 221]. The reduction process of the α-MoO_3 nanoblades leads to the formation of excess oxidation states in the crystal, which in the form of Mo^{5+} in addition to the original Mo^{6+}, as has been demonstrated by the inter-valence charge transfer model (IVCT). This effect leads to partial filling in the 4d-Mo band, which leads to an excess of oxygen deficiencies [58].

Additionally, the carbonization process of the reduced α-MoO_3 nanoblades electrode offers better electrical conductivity and admirable interfacial contact between α-MoO_3 nanoblades and carbon, and leads to rapid transportation of electrons throughout the entire electrode matrix. Therefore, binder free carbonized reduced vertically aligned α-MoO_3 nanoblades electrodes are

expected to deliver excellent supercapacitor performance.

Carbon coated vertically aligned α-MoO_3 nanoblades treated under N_2 rich atmosphere were expected to give a higher output compared to the other treatment conditions, owing to the expected addition of wettability to electrode. However, their performance was poor compared to vacuum treated samples.

A maximum specific capacitance of 22.3 $mFcm^{-2}$ at a scan rate of 5 mVs^{-1} was found for carbon coated vertically aligned α-MoO_3 nanoblades treated under vacuum. This electrode maintained a rate capability of 56.9 % after a scan rate of 125 mVs^{-1}, and a specific capacitance of 12.7 $mFcm^{-2}$. The maximum specific capacitance obtained *via* GCD was 39.75 $mFcm^{-2}$ at a current density of 0.075 $mAcm^{-2}$, as can be seen in Fig. 7.12 (d).

EIS was employed to analyze the conductivity of the electrode materials. The experiment was

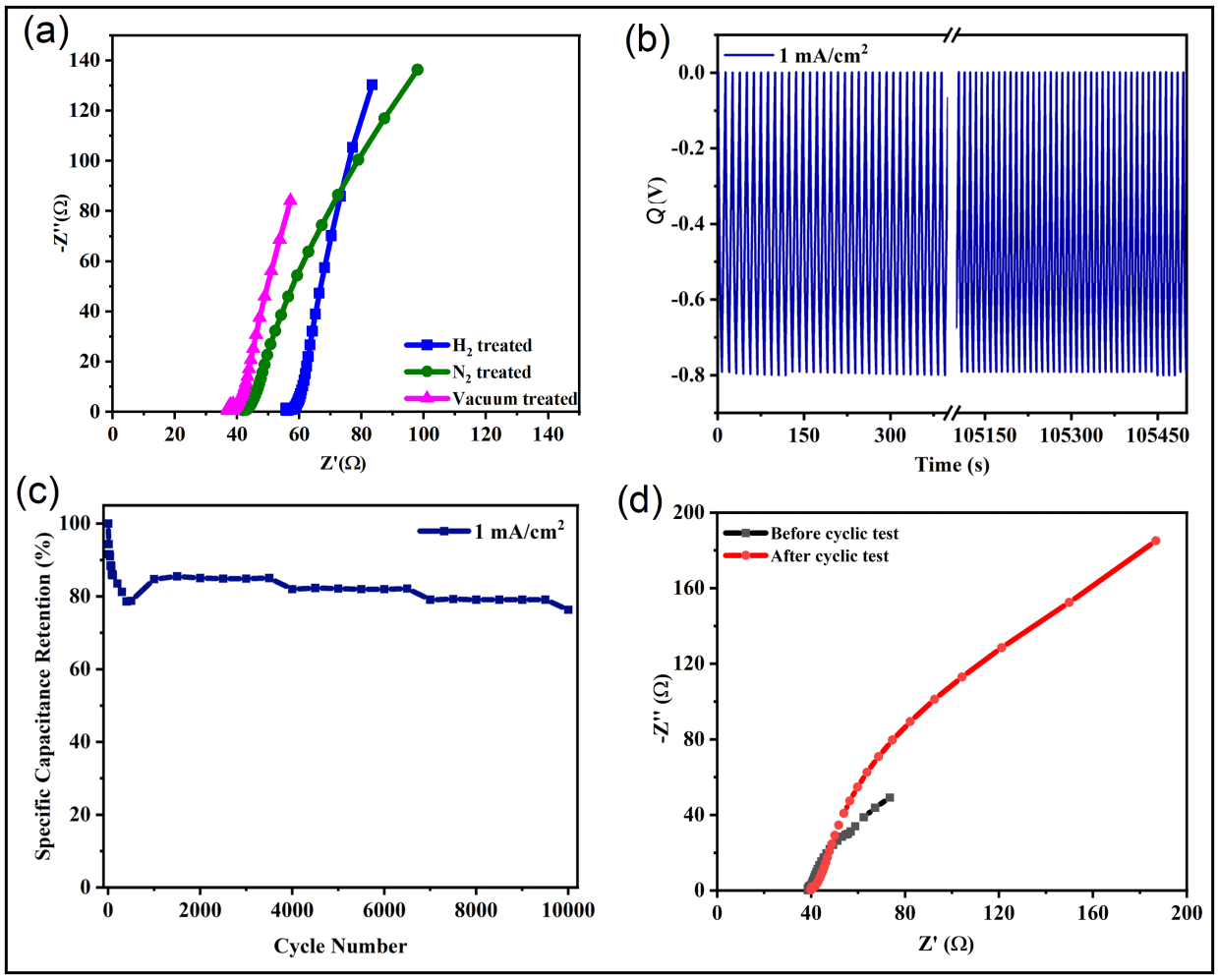

Figure 7.13: (a) Nyquist plot of carbon coated reduced vertically aligned α-MoO_3 nanoblades treated under H_2, N_2, and vacuum, respectively. (b) Cyclic stability test (potential versus time). (c) Specific capacitance retention with respect to cycle number for 10,000 cycles at a current density of 1 mA/cm^2 of vacuum treated carbonized vertically aligned α-MoO_3 nanoblades. (d) Nyquist plot before and after the cyclic test of vacuum treated carbonized vertically aligned α-MoO_3 nanoblades.

performed by using alternating current with frequencies in the range of 0.1 Hz to 100 kHz for carbon coated reduced vertically aligned α-MoO_3 nanoblades on FTO.

Following the same trend as in CV and GCD measurements, the vacuum treated electrodes show the lowest solution resistance around 37 Ω, while the H_2 treated electrodes show the highest resistance. The charge transfer resistance plus the solution resistance was calculated to be 38.7 Ω, 43.2 Ω, and 58.2 Ω for vacuum, N_2, and H_2 treated nanoblades on FTO electrodes, respectively.

It is worth to mention that, the trend observed for the conductivity is not in a good agreement with our solid films electrical conductivities (see Table. 6.3.1). The results obtained from electrochemical cell suggest that reducing the nanoblades under H_2 and N_2 rich atmospheres introduces more impurities, as intercalation of adsorbed protons (H^+ from H_2 and active N^- from N_2) can hinder the intercalation/deintercalation process, and lead to a lower performance. Moreover, it is providing a good fit to the obtained results from Raman spectra, that higher conversion to carbon is found in the vacuum annealed carbonized reduced interconnected vertically aligned α-MoO_3 nanoblades on FTO.

These results lead us to execute a stability test on the best performing electrode. Fig. 7.13 (b) shows a plot of the potential versus the time for the vacuum treated vertically aligned α-MoO_3 nanoblades for 10,000 charge-discharge cycles at a current density of 1 $mAcm^{-2}$. The specific capacitance retained up to 76.4 % of its original value even after 10,000 cycles (see Fig. 7.13 (c)).

Moreover, the electrical conductivity was calculated for vacuum treated carbon coated vertically aligned α-MoO_3 nanoblades before and after the cycling test, as shown in Fig. 7.13 (d). The solution resistance was almost unchanged after the cycle measurements, with values of 38.5 Ω and 39.8 Ω, respectively. The Warburg impedance before the cyclic test was lower compared to the value after the cycling test, as the Warburg length was shorter before the cyclic test. This refers to the fact that after the cyclic test, the kinetics of ion transportation were slower due to the structural distortion of the electrode material caused by the high number of charge-discharge cycles.

Therefore, vacuum treated carbon coated vertically aligned α-MoO_3 nanoblades on FTO electrodes have been proved to be excellent negative electrodes for supercapacitor applications.

Conclusions The following conclusions can be drawn from our studies of our structures in supercapacitor applications:

- The mixed oxidation states of Mo (Mo^{6+}, Mo^{5+}) provide good pseudocapacitive behavior. α-MoO_3 as a layered material facilitates the intercalation/deintercalation process, which is advantageous for the supercapacitor performance.

- Carbon coating of the α-MoO_3 nanoblades structure not only contributes a double layer capacitance to the overall energy storage. It can also act as a conducting agent, which greatly enhances the electrical conductivity of the hybrid structure. Thus the resulting fast electron transfer throughout the whole electrode matrix leads to an overall improvement of the electrochemical performance.

- The binder free method avoids the use of a non-conducting binding agent. In this way it enhances the electrical conductivity and provides firm adhesion between the electrode and the current collector. Furthermore, the degradation of the electrode material is reduced, proving good rate capability to the supercapacitor system.

- As the field of research into negative electrode materials for supercapacitor applications is quite sparse, vacuum treated carbon coated vertically aligned α-MoO_3 nanoblades on FTO

electrodes may constitute a new horizon for the next level of negative electrode materials in supercapacitor applications.

8. Conclusion and outlook

8.1 Summary

In summary, we have achieved a novel, facile, fast and highly reproducible strategy to grow vertically aligned, crystalline α-MoO_3 nanoblades on various conducting and non-conducting substrates using hydrothermal technique. The synthesis procedure consists of two steps: Seed layer preparation in the first step followed by growth of highly anisotropic nanoblades in the second step. The reaction time could be reduced 50-fold compared to literature methods for dispersed α-MoO_3 nanostructures. The synthesis procedure allows simple, fast, and large-scale fabrication of vertically aligned nanostructures on different substrates. Reaction time and precursor concentration were found to be the principal parameters for control of the shape and aspect ratio of the nanoblades, with a phase transition from orthorhombic α-MoO_3 to hexagonal h-MoO_3 occurring at high precursor and acid concentrations. The developed procedure resulted in vertically aligned nanostructure α-MoO_3 with a high surface area that is favorable for several devices such as gas sensors, supercapacitors and others.

Vertically aligned α-MoO_3 nanoblades have been introduced to oxidizing and reducing atmospheres at high temperature of 450 °C. The electronic properties can be altered due to changes in the concentration of oxygen vacancies inside the crystal. The oxygen vacancies have been investigated using various techniques such as electron paramagnetic resonance, x-ray diffraction, UV-visible spectrophotometer, scanning and high-resolution transition electron microscopes. Our results demonstrate experimentally the formation of oxygen vacancies within the bilayer of the crystal structure, which is consistent with previously reported theoretical and computational studies. The content of the oxygen deficiency in α-MoO_3 nanoblades as a result of the post-treatment under oxidizing and reducing atmospheres has been evaluated using the EPR technique.

The electronic properties have been studied using top co-planar electrodes. The material shows n-type behavior under reducing atmospheres and degenerated n-type behavior under oxidizing atmosphere. This has been explained using color-center formation models and polaron migration. The electrical conductivity is found to be in the range of $7 \times 10^{-6} - 1 \times 10^{-2}$ $\mathrm{S\,m^{-1}}$ for oxidized to reduced α-MoO_3 nanoblades, respectively. This is two orders of magnitude higher ($\times 10^2$) than previously reported values for similar morphologies.

Finally, the vertically aligned α-MoO_3 nanoblades were tested for gas sensing and in electrochemical supercapacitors. They showed a fast response towards CO gas. Applying the new vertically aligned nanostructures to sensor devices cast a new light on such low-cost substrates with a high surface area of very dense nanostructure.

Additionally, hybrid carbonized reduced vertically aligned α-MoO_3 nanoblades have been done *via* a separate carbonization process to be introduced to a supercapacitor application as a negative electrode. The carbonized reduced vertically aligned α-MoO_3 nanoblades show a significant pseudocapacitive performance with a high specific capacitance and higher stability. Hence, the new

morphological design creates a path towards the development of next-generation supercapacitor negative electrode material.

8.2 Outlook

In this thesis, we have discussed in detail the α-MoO_3 nanostructure properties and their significant properties, which are favorable for a wide range of applications. However, additional studies can be achieved with high crystallinity and stability nature of these nanostructures in mind. These are summarized in the following points:

Chromogenic properties. As we already mentioned, different growth parameters during the synthesis procedure can be varied, which leads to different morphologies and dimensions as can be seen in Fig. 8.1. It is potentially highly interesting to study the chromogenic effect on different phases of MoO_3 as we can see in the figures (c), (d), (e) for the alpha phase, mixed phases, and the hexagonal phase, respectively.

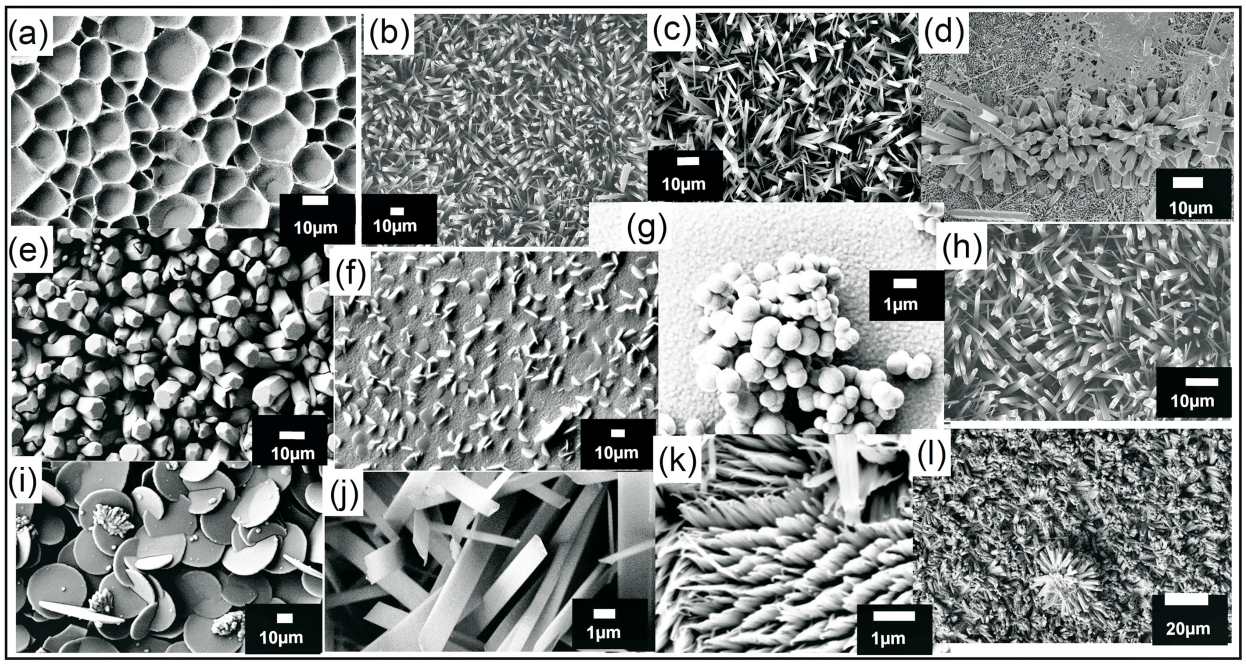

Figure 8.1: Different nanostructures of the direct growth of different MoO_3 phases.

Electrode configuration. To follow our study, the electronic properties can be studied closely using modified electrode configurations because the literature on the electrical connection methods for such structures is not consistent. See Fig. 8.2 (a), which shows stable I-V characteristics for both electrode configurations. However, as discussed in chapter 6, the top-bottom electrodes needs a further modification to obtain a reproducible values.

Oxygen vacancy characterization. In addition to that, studies on the role of oxygen vacancies in α-MoO_3 nanoblades produced by different temperatures (thermochromic effect) and vacancies

produced by UV illumination (photochromic effect) under various atmospheres need to be continued. As a preliminary study, Fig. 8.2 (b) shows the drastic increase in the electrical conductivity of α-MoO_3 nanoblades treated at different temperatures under H_2 rich atmosphere. Moreover, it is interesting to study the electrical conductivity of different MoO_3 phases to have better control for potential applications.

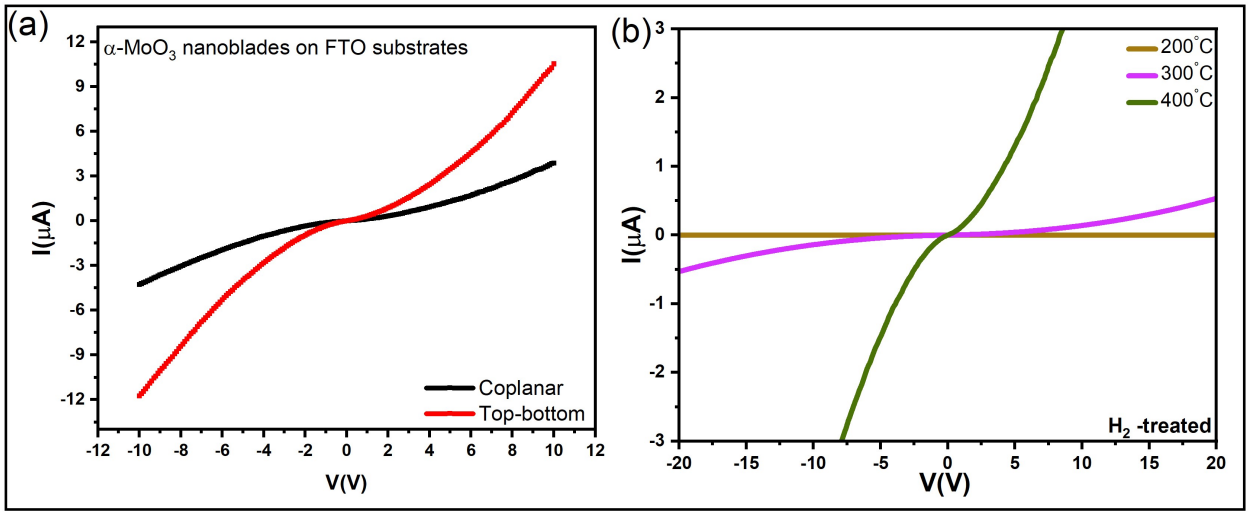

Figure 8.2: (a) I-V characteristics of α-MoO_3 nanoblades connected through coplanar Au electrodes and top-bottom electrical measurements. (b) Effect of H_2 treatment at different temperatures on the electrical conductivity.

Application in photodetectors. A closer look at the literature on photodetector efficiency for such structures remains to be addressed. This can provide a wide range of responses to different areas of the excitation energies. As we can see in home-made workstation in Fig. 3.1, the window can be used as a top illumination window for different excitation wavelengths to study the photodetection performance under different atmospheres and a direct transformation to an electrical signal [37].

Catalytic applications. Since MoO_3 is applied as photocatalyst and in water degradation applications, doping of the material with a metal offers the potential for higher free carrier concentration, higher electrical conductivity, better ion intercalation/deintercalation, higher photon conversion efficiency and lower optical band gap [222, 223]. In principle, doping can hinder the recombination of photogenerated electron-hole pairs [118].

As a trial, doping with ruthenium has been achieved. This can be seen in Fig. 8.3 (b). The doping happens through substitution of Mo atoms in the crystal, which is evident from the right shift in the XRD peaks without appearance of new peaks (The atomic radii of Mo and Ru are 190 and 178 pm, respectively.). Ru-doped α-MoO_3 shows a red shift in the optical band gap and a higher electrical conductivity in comparison to undoped α-MoO_3 nanoblades, as can be seen in Fig. 8.3 (c-d), respectively.

Application in supercapacitors. For use as a negative electrode in the supercapacitor application, there is a gap between the experimental and theoretical specific capacitance of α-MoO_3. This

gap can be narrowed down through different modification processes, such as doping the material to improve the ion intercalation/deintercalation. Therefore, Ru-doped α-MoO_3 nanostructures can offer a higher specific capacity and better stability.

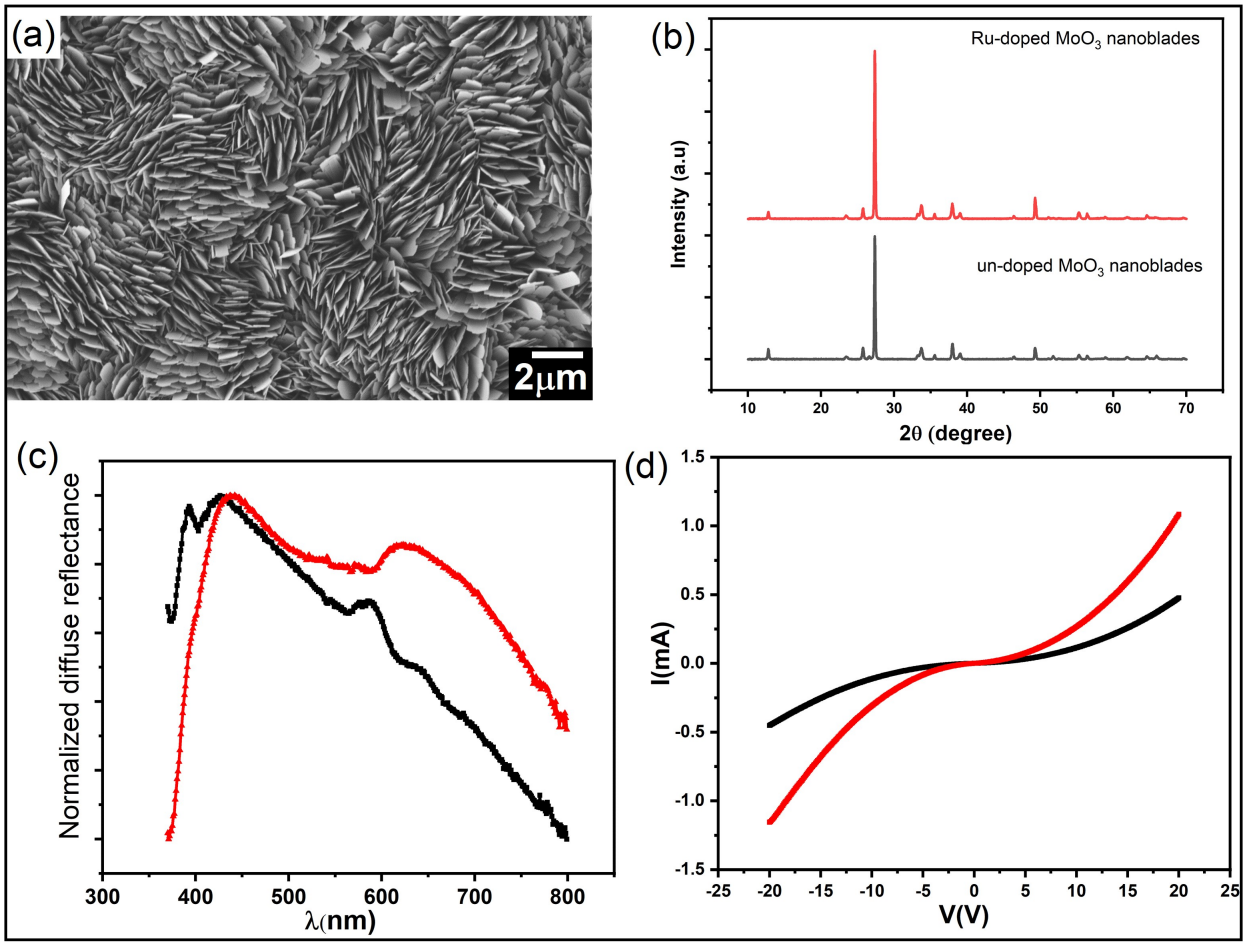

Figure 8.3: (a) Ru-doped α-MoO_3 nanoblades (2 %). (b) X-ray diffraction patterns of Ru-doped and undoped α-MoO_3 nanoblades. (c) A normalized diffuse reflectance vs. incident wavelength of Ru-doped and undoped α-MoO_3 nanoblades. (d) I-V characteristics of Ru-doped and undoped α-MoO_3 nanoblades.

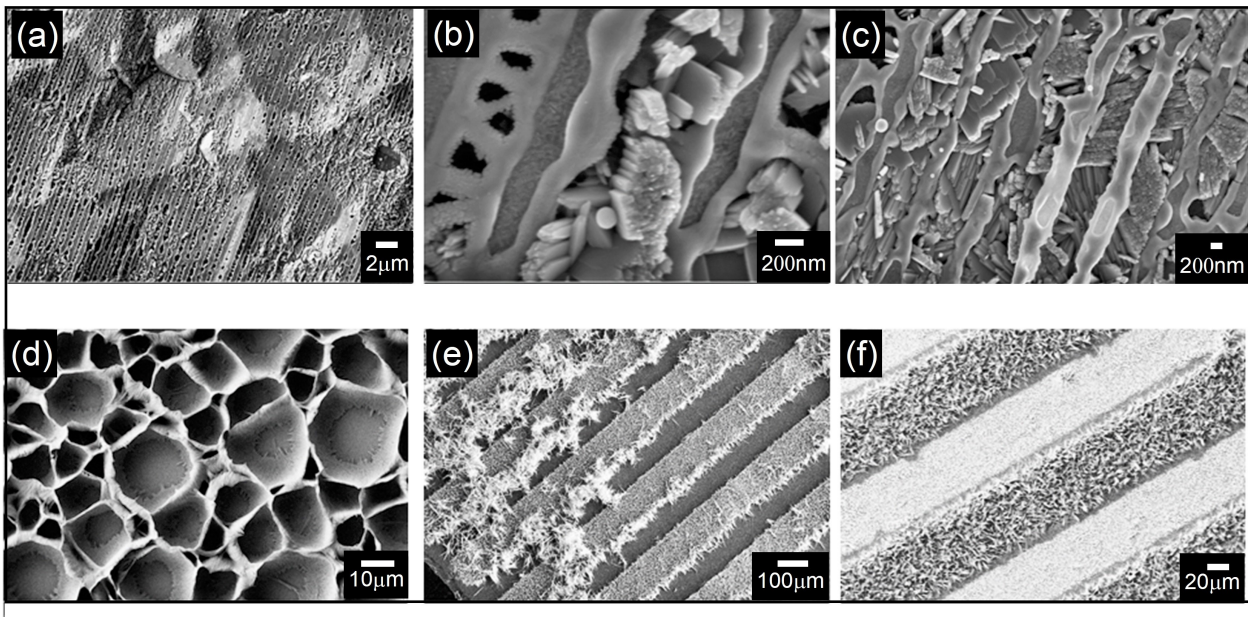

Figure 8.4: (a-c) α-MoO_3 nanoblades grown on pre-patterned seeded substrates *via* direct laser interference. (d) α-MoO_3 nanoblades on etched substrates using H_2SO_4 followed with seed layer deposition using sputtering. (e-f) α-MoO_3 nanoblades grown on pre-patterned substrates by the seed layer using an evaporation mask.

Application in hybrid solar cells. In solar cell applications, it is favorable to have a high conductivity and a tunable work function [21]. This can be achieved, as we discussed in our study, by treating the material in different atmospheres [4, 189, 224].

A MoO_3 layer has been used as a hole transport layer in solar cells [225]. It yields a significant speed advantage in the direction of higher efficient solar cells and can be realized *via* an interdigitated or quasi-interdigitated back electrode when growing different MoO_3 nanostructures with a high surface area on pre-patterned substrates. Such a solar cell configuration shows a lower recombination loss through control of the layers separation to fit the diffusion length of the electron-hole pairs [226].

Fig. 8.4 (a-c) show nanoscale patterns (distance between the fingers around 500 nm) on the seeded substrates, which have been created using a direct laser interference pattering (532 nm pulsed laser beam of 10 Hz). (These experiments have been done together with Prof. Johannes Boneberg). The aim here is to develop a fast method for controlled nano-interdistance patterns in the framework for efficient interdigitated and quasi-interdigitated solar cells.

Other patterns (see Fig. 8.4 (d)) have been achieved using an etching process on the substrates using H_2SO_4. This was followed by sputtering an MoO_3 layer, ambient annealing at 450 °C, and then the hydrothermal procedure. Fig 8.4 (e-f) show micro-interdistance patterns created by deposition of the seed layer through an interdigitated evaporation mask.

Bibliography

[1] S. Z. Noby, K. K. Wong, A. Ramadoss, S. Siroky, M. Hagner, K. Boldt, and L. Schmidt-Mende, "Rapid synthesis of vertically aligned α-MoO_3 nanostructures on substrates," *RSC Advances*, vol. 10, no. 40, pp. 24119–24126, 2020.

[2] A. J. Millis, "Transition metal oxides." 5th MaNEP Winter School, Website, 2013. Online available under `http://www.manep-nccr.ch/en/events/saasfee13/pdf/Millis-1.pdf`; accessed August 2020).

[3] M. S. Chavali and M. P. Nikolova, "Metal oxide nanoparticles and their applications in nanotechnology," *SN Applied Sciences*, vol. 1, no. 6, 2019.

[4] M. T. Greiner, L. Chai, M. G. Helander, W.-M. Tang, and Z.-H. Lu, "Metal/metal-oxide interfaces: How metal contacts affect the work function and band structure of MoO_3," *Advanced Functional Materials*, vol. 23, no. 2, pp. 215–226, 2013.

[5] M. Labanowska, "Paramagnetic defects in MoO_3 – revisited," *Physical Chemistry Chemical Physics*, vol. 1, no. 23, pp. 5385–5392, 1999.

[6] K. Dyrek and M. Labanowska, "Electron-paramagnetic resonance investigation of the paramagnetic centers in polycrystalline MoO_3," *Journal of the Chemical Society-Faraday Transactions*, vol. 87, no. 7, pp. 1003–1009, 1991.

[7] K. Inzani, T. Grande, F. Vullum-Bruer, and S. M. Selbach, "A van der waals density functional study of MoO_3 and its oxygen vacancies," *The Journal of Physical Chemistry C*, vol. 120, no. 16, pp. 8959–8968, 2016.

[8] H. Schroeder, "Poole-Frenkel-effect as dominating current mechanism in thin oxide films – an illusion?!," *Journal of Applied Physics*, vol. 117, no. 21, 2015.

[9] S. Choopun, N. Hongsith, and E. Wongrat, *Metal-Oxide Nanowires for Gas Sensors*, book section Chapter 1. IntechOpen, 2012.

[10] H.-Y. Li, L. Huang, X.-X. Wang, C.-S. Lee, J.-W. Yoon, J. Zhou, X. Guo, and J.-H. Lee, "Molybdenum trioxide nanopaper as a dual gas sensor for detecting trimethylamine and hydrogen sulfide," *RSC Advances*, vol. 7, no. 7, pp. 3680–3685, 2017.

[11] C. N. R. Rao, "Transition-metal oxides," *Annual Review of Physical Chemistry*, vol. 40, pp. 291–326, 1989.

[12] M. M. Rojo, O. C. Calero, A. F. Lopeandia, J. Rodriguez-Viejo, and M. Martin-Gonzalez, "Review on measurement techniques of transport properties of nanowires," *Nanoscale*, vol. 5, no. 23, pp. 11526–44, 2013.

[13] Q. Yang, Z. Lu, J. Liu, X. Lei, Z. Chang, L. Luo, and X. Sun, "Metal oxide and hydroxide nanoarrays: Hydrothermal synthesis and applications as supercapacitors and nanocatalysts," *Progress in Natural Science: Materials International*, vol. 23, no. 4, pp. 351–366, 2013.

[14] C. Rao, G. Rao, and U. S. N. B. of Standards, *Transition Metal Oxides: Crystal Chemistry, Phase Transition, and Related Aspects*, vol. 49 of *NSRDS-NBS*. U.S. Department of Commerce, National Bureau of Standards, 1974.

[15] P. E. Bruce A. Averill, *General Chemistry: Principles, Patterns, and Applications*, ch. The d-Block Elements. The Saylor Foundation, 2012.

[16] P. E. Bruce Averill, *General Chemistry Principles, Patterns, and Applications*, vol. 1.0. Saylor Foundation, 2011.

[17] Y. Song, J. Zhao, Y. Zhao, Z. Huang, Y. Li, and G. Wu, "Synthesis of α-MoO_3 nanobelts with preferred orientation and good photochromic performance," *CrystEngComm*, vol. 18, no. 34, pp. 6502–6512, 2016.

[18] M. Niederberger, F. Krumeich, H. J. Muhr, M. Muller, and R. Nesper, "Synthesis and characterization of novel nanoscopic molybdenum oxide fibers," *Journal of Materials Chemistry*, vol. 11, no. 7, pp. 1941–1945, 2001.

[19] X.-L. Li, J.-F. Liu, and Y.-D. Li, "Low-temperature synthesis of large-scale single-crystal molybdenum trioxide (MoO_3) nanobelts," *Applied Physics Letters*, vol. 81, p. 4832, Dec. 2002.

[20] J. Zhou, S. Z. Deng, N. S. Xu, J. Chen, and J. C. She, "Synthesis and field-emission properties of aligned MoO_3 nanowires," *Applied Physics Letters*, vol. 83, no. 13, pp. 2653–2655, 2003.

[21] Y. Gong, Y. Dong, B. Zhao, R. Yu, S. Hu, and Z. Tan, "Diverse applications of MoO_3 for high performance organic photovoltaics: fundamentals, processes and optimization strategies," *Journal of Materials Chemistry A*, 2020.

[22] L. X. Song, J. Xia, Z. Dang, J. Yang, L. B. Wang, and J. Chen, "Formation, structure and physical properties of a series of α-MoO_3 nanocrystals: from 3D to 1D and 2D," *CrystEngComm*, vol. 14, no. 8, pp. 2675–2682, 2012.

[23] D. D. Yao, J. Z. Ou, K. Latham, S. Zhuiykov, A. P. O'Mullane, and K. Kalantar-zadeh, "Electrodeposited α- and β-phase MoO_3 films and investigation of their gasochromic properties," *Crystal Growth & Design*, vol. 12, no. 4, pp. 1865–1870, 2012.

[24] P. Martin-Ramos, I. A. Fernandez-Coppel, M. Avella, and J. Martin-Gil, "α-MoO_3 crystals with a multilayer stack structure obtained by annealing from a lamellar MoS_2/g-C_3N_4 nanohybrid," *Nanomaterials (Basel)*, vol. 8, no. 7, 2018.

[25] A. K. M.C. Rao, K. Ravindranadh and M. Shekhawat, "Structural stoichiometry and phase transitions of MoO_3 thin films for solid state microbatteries," *Research Journal of Recent Sciences*, vol. 2(4), pp. 67–73, 2013.

[26] D. D. Yao, J. Z. Ou, K. Latham, S. Zhuiykov, A. P. O'Mullane, and K. Kalantar-zadeh, "Electrodeposited α- and β-phase MoO_3 films and investigation of their gasochromic properties," *Crystal Growth & Design*, vol. 12, no. 4, pp. 1865–1870, 2012.

[27] H. Hu, C. Deng, J. Xu, K. Zhang, and M. Sun, "Metastable h- MoO_3 and stable α-MoO_3 microstructures: controllable synthesis, growth mechanism and their enhanced photocatalytic activity," *Journal of Experimental Nanoscience*, vol. 10, no. 17, pp. 1336–1346, 2015.

[28] P. A. Spevack and N. S. Mcintyre, "Thermal reduction of MoO_3," *Journal of Physical Chemistry*, vol. 96, no. 22, pp. 9029–9035, 1992.

[29] A. Pathak, A. S. Gangan, S. Ratha, B. Chakraborty, and C. S. Rout, "Enhanced pseudocapacitance of MoO_3-reduced graphene oxide hybrids with insight from density functional theory investigations," *The Journal of Physical Chemistry C*, vol. 121, no. 35, pp. 18992–19001, 2017.

[30] H. Ding, H. Lin, B. Sadigh, F. Zhou, V. Ozoliņš, and M. Asta, "Computational investigation of electron small polarons in α-MoO_3," *The Journal of Physical Chemistry C*, vol. 118, no. 29, pp. 15565–15572, 2014.

[31] R. S. Datta, F. Haque, M. Mohiuddin, B. J. Carey, N. Syed, A. Zavabeti, B. Zhang, H. Khan, K. J. Berean, J. Z. Ou, N. Mahmood, T. Daeneke, and K. Kalantar-zadeh, "Highly active two dimensional α-$MoO_{(3-x)}$ for the electrocatalytic hydrogen evolution reaction," *Journal of Materials Chemistry A*, vol. 5, no. 46, pp. 24223–24231, 2017.

[32] J. B. Zhou, N. Lin, L. B. Wang, K. L. Zhang, Y. C. Zhu, and Y. T. Qian, "Synthesis of hexagonal MoO_3 nanorods and a study of their electrochemical performance as anode materials for lithium-ion batteries," *Journal of Materials Chemistry A*, vol. 3, no. 14, pp. 7463–7468, 2015.

[33] H. Sinaim, D. Ham, J. S. Lee, A. Phuruangrat, S. Thongtem, and T. Thongtem, "Free-polymer controlling morphology of α-MoO_3 nanobelts by a facile hydrothermal synthesis, their electrochemistry for hydrogen evolution reactions and optical properties," *Journal of Alloys and Compounds*, vol. 516, pp. 172–178, 03 2012.

[34] J. Yang, X. Xiao, P. Chen, K. Zhu, K. Cheng, K. Ye, G. Wang, D. Cao, and J. Yan, "Creating oxygen-vacancies in MoO_3 nanobelts toward high volumetric energy-density asymmetric supercapacitors with long lifespan," *Nano Energy*, vol. 58, pp. 455–465, 2019.

[35] S. N. Lou, N. Yap, J. Scott, R. Amal, and Y. H. Ng, "Influence of MoO_3(110) crystalline plane on its self-charging photoelectrochemical properties," *Sci Rep*, vol. 4, p. 7428, 2014.

[36] S. N. Lou, Y. H. Ng, C. Ng, J. Scott, and R. Amal, "Harvesting, storing and utilising solar energy using MoO_3: modulating structural distortion through ph adjustment," *ChemSusChem*, vol. 7, no. 7, pp. 1934–41, 2014.

[37] D. Xiang, C. Han, J. Zhang, and W. Chen, "Gap states assisted MoO_3 nanobelt photodetector with wide spectrum response," *Scientific Reports*, vol. 4, p. 4891, 2014.

[38] N. Illyaskutty, S. Sreedhar, G. Sanal Kumar, H. Kohler, M. Schwotzer, C. Natzeck, and V. P. M. Pillai, "Alteration of architecture of MoO_3 nanostructures on arbitrary substrates: growth kinetics, spectroscopic and gas sensing properties," *Nanoscale*, vol. 6, no. 22, pp. 13882–13894, 2014.

[39] D. Kwak, M. Wang, K. J. Koski, L. Zhang, H. Sokol, R. Maric, and Y. Lei, "Molybdenum trioxide (α-MoO_3) nanoribbons for ultrasensitive ammonia (NH_3) gas detection: Integrated experimental and density functional theory simulation studies," *ACS Appl Mater Interfaces*, vol. 11, no. 11, pp. 10697–10706, 2019.

[40] L. Zhang, Z. Liu, L. Jin, B. Zhang, H. Zhang, M. Zhu, and W. Yang, "Self-assembly gridding α-MoO_3 nanobelts for highly toxic H_2S gas sensors," *Sensors and Actuators B: Chemical*, vol. 237, pp. 350–357, 2016.

[41] S. Yang, Z. Wang, Y. Hu, X. Luo, J. Lei, D. Zhou, L. Fei, Y. Wang, and H. Gu, "Highly responsive room-temperature hydrogen sensing of α-MoO_3 nanoribbon membranes," *ACS Applied Materials & Interfaces*, vol. 7, no. 17, pp. 9247–9253, 2015.

[42] F. Ji, X. Ren, X. Zheng, Y. Liu, L. Pang, J. Jiang, and S. F. Liu, "2D- MoO_3 nanosheets for superior gas sensors," *Nanoscale*, vol. 8, no. 16, pp. 8696–703, 2016.

[43] P. Martín-Ramos, I. A. Fernández-Coppel, M. Avella, and J. Martín-Gil, "α-MoO_3 crystals with a multilayer stack structure obtained by annealing from a lamellar MoS_2/g-C_3N_4 nanohybrid," *Nanomaterials (Basel, Switzerland)*, vol. 8, no. 7, p. 559, 2018.

[44] S. Balendhran, J. Deng, J. Z. Ou, S. Walia, J. Scott, J. Tang, K. L. Wang, M. R. Field, S. Russo, S. Zhuiykov, M. S. Strano, N. Medhekar, S. Sriram, M. Bhaskaran, and K. Kalantar-zadeh, "Enhanced charge carrier mobility in two-dimensional high dielectric molybdenum oxide," *Advanced Materials*, vol. 25, no. 1, pp. 109–114, 2013.

[45] W. Pan, R. Tian, H. Jin, Y. Guo, L. Zhang, X. Wu, L. Zhang, Z. Han, G. Liu, J. Li, G. Rao, H. Wang, and W. Chu, "Structure, optical, and catalytic properties of novel hexagonal metastable h-MoO_3 nano- and microrods synthesized with modified liquid-phase processes," *Chemistry of Materials*, vol. 22, no. 22, pp. 6202–6208, 2010.

[46] M. Benelmekki and A. Erbe, *Frontiers of Nanoscience*, vol. 14, book section Nanostructured thin films– background, preparation and relation to the technological revolution of the 21st century, pp. 1–34. Elsevier, 2019.

[47] I. V. Frishberg, *Handbook of Non-Ferrous Metal Powders (Second Edition)*, book section Gas-Phase Method of Metal Powder Production, pp. 187–200. Oxford: Elsevier, 2019.

[48] J. Zhang, "Fractal growth of MoO_3 crystals during vapor-phase deposition," *physica status solidi (a)*, vol. 119, no. 1, pp. 41–46, 1990.

[49] R. K. Upadhyay and L. A. Kumaraswamidhas, *Handbook of Materials Failure Analysis*, book section Bearing failure issues and corrective measures through surface engineering, pp. 209–233. Butterworth-Heinemann, 2018.

[50] S. S. Withanage, H. Kalita, H.-S. Chung, T. Roy, Y. Jung, and S. I. Khondaker, "Uniform vapor-pressure-based chemical vapor deposition growth of MoS_2 using MoO_3 thin film as a precursor for coevaporation," *ACS Omega*, vol. 3, no. 12, pp. 18943–18949, 2018.

[51] D. Hanlon, C. Backes, T. M. Higgins, M. Hughes, A. O'Neill, P. King, N. McEvoy, G. S. Duesberg, B. Mendoza Sanchez, H. Pettersson, V. Nicolosi, and J. N. Coleman, "Production of molybdenum trioxide nanosheets by liquid exfoliation and their application in high-performance supercapacitors," *Chemistry of Materials*, vol. 26, no. 4, pp. 1751–1763, 2014.

[52] F. Seitz, "Color centers in alkali halide crystals.II," *Rev. Mod. Phys.*, vol. 26, pp. 7–94, Jan 1954.

[53] S. K. Deb and J. A. Chopoorian, "Optical properties and color-center formation in thin films of molybdenum trioxide," *Journal of Applied Physics*, vol. 37, no. 13, pp. 4818–4825, 1966.

[54] C. C. Chang, P. W. Chi, P. Chandan, and C. K. Lin, "Electrochemistry and rapid electrochromism control of MoO_3/V_2O_5 hybrid nanobilayers," *Materials (Basel)*, vol. 12, no. 15, 2019.

[55] M. A. Arvizu, M. Morales-Luna, S. A. Tomás, P. Rodríguez, and O. Zelaya-Angel, "Photochromism and thermochromism of MoO_3 thin films doped with ZnSe," *AIP Conference Proceedings*, vol. 1420, no. 1, pp. 151–156, 2012.

[56] R. J. Colton, A. M. Guzman, and J. W. Rabalais, "Photochromism and electrochromism in amorphous transition metal oxide films," *Accounts of Chemical Research*, vol. 11, no. 4, pp. 170–176, 1978.

[57] P. M. S. Monk, T. Ali, and R. D. Partridge, "The effect of doping electrochromic molybdenum oxide with other metal oxides: Correlation of optical and kinetic properties," *Solid State Ionics*, vol. 80, no. 1, pp. 75–85, 1995.

[58] T. He and J. Yao, "Photochromism of molybdenum oxide," *Journal of Photochemistry and Photobiology C: Photochemistry Reviews*, vol. 4, no. 2, pp. 125–143, 2003.

[59] J. N. Yao, B. H. Loo, K. Hashimoto, and A. Fujishima, "Photochromic and electrochromic behavior of electrodeposited MoO_3 thin films," *Journal of Electroanalytical Chemistry and Interfacial Electrochemistry*, vol. 290, no. 1, pp. 263–267, 1990.

[60] H. Simchi, B. E. McCandless, T. Meng, J. H. Boyle, and W. N. Shafarman, "Characterization of reactively sputtered molybdenum oxide films for solar cell application," *Journal of Applied Physics*, vol. 114, no. 1, p. 013503, 2013.

[61] C. G. Granqvist, *Handbook of Inorganic Electrochromic Materials*. Amsterdam: Elsevier Science B.V., 1995.

[62] M. Rouhani, S. Gorelik, J. Hobley, S. J. Wang, E. L. Williams, and Y. L. Foo, "Delayed onset of photochromism in molybdenum oxide films caused by photoinduced defect formation," *Science and technology of advanced materials*, vol. 12, no. 5, pp. 055010–055010, 2011.

[63] R. Casler, P. Pringsheim, and P. Yuster, "Stability of color centers in alkali halides," *The Journal of Chemical Physics*, vol. 18, no. 6, pp. 887–891, 1950.

[64] H. Pick, "Über den Einfluß der Temperatur auf die Erregung von Farbzentren," *Annalen der Physik*, vol. 423, no. 4, pp. 365–376, 1938.

[65] H. Pick, "The quantitative deflection of optical break down in the F-band in alkali halogenide crystals," *Annalen der Physik*, vol. 37, no. 5/6, pp. 421–428, 1940.

[66] D. A. R. D. W. Lynch, "Study of the F' center in several alkali halides," *Physical Review*, vol. 174, no. 3, pp. 1050–1059, 1968.

[67] B. W. Faughnan, R. S. Crandall, P. M. Heyman, *et al.*, "Electrochromism in WO_3 amorphous films," *Rca Rev*, vol. 36, no. 1, pp. 177–197, 1975.

[68] J. P. Lehan, P. C. Yu, D. L. Backfisch, and J. P. Chambers, "Predictive model of the optical response of amorphous WO_3 to ion intercalation," *Journal of Applied Physics*, vol. 92, no. 7, pp. 3608–3614, 2002.

[69] L. Landau, "Über die Bewegung der Elektronen in Kristallgitter," *Phys. Z. Sowjetunion*, vol. 3, pp. 644–645, 1933.

[70] S. K. Deb, "Opportunities and challenges in science and technology of WO_3 for electrochromic and related applications," *Solar Energy Materials and Solar Cells*, vol. 92, no. 2, pp. 245–258, 2008.

[71] M. Rouhani, *Photochromism of Molybdenum Oxide*. PhD thesis, National university of Singapore, 2013.

[72] S. Deb, "Optical and photoelectric properties and colour centres in thin films of tungsten oxide," *Philosophical Magazine*, vol. 27, no. 4, pp. 801–822, 1973.

[73] M. T. Greiner, L. Chai, M. G. Helander, W. M. Tang, and Z. H. Lu, "Transition metal oxide work functions: The influence of cation oxidation state and oxygen vacancies," *Advanced Functional Materials*, vol. 22, no. 21, pp. 4557–4568, 2012.

[74] M. T. Greiner, M. G. Helander, W.-M. Tang, Z.-B. Wang, J. Qiu, and Z.-H. Lu, "Universal energy-level alignment of molecules on metal oxides," *Nature Materials*, vol. 11, no. 1, pp. 76–81, 2012.

[75] A. H. Nethercot, "Prediction of Fermi energies and photoelectric thresholds based on electronegativity concepts," *Physical Review Letters*, vol. 33, no. 18, pp. 1088–1091, 1974.

[76] M. M. Y. A. Alsaif, A. F. Chrimes, T. Daeneke, S. Balendhran, D. O. Bellisario, Y. Son, M. R. Field, W. Zhang, H. Nili, E. P. Nguyen, K. Latham, J. van Embden, M. S. Strano, J. Z. Ou, and K. Kalantar-zadeh, "High-performance field effect transistors using electronic inks of 2D molybdenum oxide nanoflakes," *Advanced Functional Materials*, vol. 26, no. 1, pp. 91–100, 2016.

[77] S. Balendhran, J. Deng, J. Z. Ou, S. Walia, J. Scott, J. Tang, K. L. Wang, M. R. Field, S. Russo, S. Zhuiykov, M. S. Strano, N. Medhekar, S. Sriram, M. Bhaskaran, and K. Kalantar-zadeh, "Enhanced charge carrier mobility in two-dimensional high dielectric molybdenum oxide," *Advanced Materials*, vol. 25, no. 1, pp. 109–114, 2013.

[78] J. Liu, L. He, L. Wang, Y. Man, L. Huang, Z. Xu, D. Ge, J. Li, C. Liu, and L. Wang, "Significant enhancement of the adhesion between metal films and polymer substrates by UV-Ozone surface modification in nanoscale," *ACS Appl Mater Interfaces*, vol. 8, no. 44, pp. 30576–30582, 2016.

[79] S. Stoll and A. Schweiger, "Easyspin, a comprehensive software package for spectral simulation and analysis in EPR," *J Magn Reson*, vol. 178, no. 1, pp. 42–55, 2006.

[80] R. Kumar, "Characterizations of MoO_3 thin films synthesized by reactive thermal evaporation technique," *AIP Conference Proceedings*, vol. 1860, no. 1, p. 020011, 2017.

[81] S. Ashraf, C. S. Blackman, G. Hyett, and I. P. Parkin, "Aerosol assisted chemical vapour deposition of MoO_3 and MoO_2 thin films on glass from molybdenum polyoxometallate precursors; thermophoresis and gas phase nanoparticle formation," *Journal of Materials Chemistry*, vol. 16, no. 35, pp. 3575–3582, 2006.

[82] P. Balasubramanian, M. Annalakshmi, S.-M. Chen, and T.-W. Chen, "Sonochemical synthesis of molybdenum oxide (MoO_3) microspheres anchored graphitic carbon nitride (g-C_3N_4) ultrathin sheets for enhanced electrochemical sensing of furazolidone," *Ultrasonics Sonochemistry*, vol. 50, pp. 96–104, 2019.

[83] L. Cai, C. J. McClellan, A. L. Koh, H. Li, E. Yalon, E. Pop, and X. Zheng, "Rapid flame synthesis of atomically thin MoO_3 down to monolayer thickness for effective hole doping of WSe_2," *Nano Letters*, vol. 17, no. 6, pp. 3854–3861, 2017.

[84] K. Sakaushi, J. Thomas, S. Kaskel, and J. Eckert, "Aqueous solution process for the synthesis and assembly of nanostructured one-dimensional α-MoO_3 electrode materials," *Chemistry of Materials*, vol. 25, no. 12, pp. 2557–2563, 2013.

[85] W. J. Dong, J. Ham, G. H. Jung, J. H. Son, and J. L. Lee, "Ultrafast laser-assisted synthesis of hydrogenated molybdenum oxides for flexible organic solar cells," *Journal of Materials Chemistry A*, vol. 4, no. 13, pp. 4755–4762, 2016.

[86] S. A. Khalate, R. S. Kate, H. M. Pathan, and R. J. Deokate, "Structural and electrochemical properties of spray deposited molybdenum trioxide (α-MoO_3) thin films," *Journal of Solid State Electrochemistry*, vol. 21, no. 9, pp. 2737–2746, 2017.

[87] J. M. Romo-Herrera, M. Terrones, H. Terrones, S. Dag, and V. Meunier, "Covalent 2D and 3D networks from 1D nanostructures: Designing new materials," *Nano Letters*, vol. 7, no. 3, pp. 570–576, 2007.

[88] S. J. Pearton and F. Ren, "Wide bandgap semiconductor one-dimensional nanostructures for applications in nanoelectronics and nanosensors," *Nanomaterials and Nanotechnology*, vol. 3, p. 1, 2013.

[89] R. Ahmad, S. M. Majhi, X. Zhang, T. M. Swager, and K. N. Salama, "Recent progress and perspectives of gas sensors based on vertically oriented ZnO nanomaterials," *Adv Colloid Interface Sci*, vol. 270, pp. 1–27, 2019.

[90] N. Barsan and K. Schierbaum, *Gas Sensors Based on Conducting Metal Oxides*. Elsevier, 2019.

[91] A. Ponzoni, C. Baratto, N. Cattabiani, M. Falasconi, V. Galstyan, E. Nunez-Carmona, F. Rigoni, V. Sberveglieri, G. Zambotti, and D. Zappa, "Metal oxide gas sensors, a survey of selectivity issues addressed at the sensor lab, Brescia (Italy)," *Sensors (Basel)*, vol. 17, no. 4, 2017.

[92] I. Gonzalez-Valls and M. Lira-Cantu, "Vertically-aligned nanostructures of ZnO for excitonic solar cells: a review," *Energy Environ. Sci.*, vol. 2, no. 1, pp. 19–34, 2009.

[93] J. Zhou, S. Z. Deng, N. S. Xu, J. Chen, and J. C. She, "Synthesis and field-emission properties of aligned MoO_3 nanowires," *Applied Physics Letters*, vol. 83, no. 13, pp. 2653–2655, 2003.

[94] B. Yan, Z. Zheng, J. Zhang, H. Gong, Z. Shen, W. Huang, and T. Yu, "Orientation controllable growth of MoO_3 nanoflakes: Micro-raman, field emission, and birefringence properties," *The Journal of Physical Chemistry C*, vol. 113, no. 47, pp. 20259–20263, 2009.

[95] S. Boubenia, A. S. Dahiya, G. Poulin-Vittrant, F. Morini, K. Nadaud, and D. Alquier, "A facile hydrothermal approach for the density tunable growth of ZnO nanowires and their electrical characterizations," *Scientific Reports*, vol. 7, no. 1, p. 15187, 2017.

[96] M. Iraj, F. D. Nayeri, E. Asl-Soleimani, and K. Narimani, "Controlled growth of vertically aligned TiO_2 nanorod arrays using the improved hydrothermal method and their application to dye-sensitized solar cells," *Journal of Alloys and Compounds*, vol. 659, pp. 44–50, 2016.

[97] Z. Rujia, Z. Zhang, L. Jiang, K. Xu, Q. Tian, S. Xue, J. Hu, Y. Bando, and D. Golberg, "Heterostructures of vertical, aligned and dense SnO_2 nanorods on graphene sheets: in situ TEM measured mechanical, electrical and field emission properties," *Journal of Materials Chemistry*, vol. 22, no. 36, pp. 19196–19201, 2012.

[98] M. Todeschini, A. Bastos da Silva Fanta, F. Jensen, J. B. Wagner, and A. Han, "Influence of Ti and Cr adhesion layers on ultrathin Au films," *ACS Applied Materials & Interfaces*, vol. 9, no. 42, pp. 37374–37385, 2017.

[99] N. Schönberg, W. G. Overend, A. Munthe-Kaas, and N. A. Sörensen, "X-ray studies on vanadium and chromium oxides with low oxygen content," *Acta Chemica Scandinavica*, vol. 8, pp. 221–225, 1954.

[100] P. H. G. Thurner, "Oxidation of polycrystalline chromium between 30°C and 400°C," *Acta Physica Polonica A*, vol. 81, pp. 273–283, 1992.

[101] C. Palacio, H. J. Mathieu, and D. Landolt, "AES, XPS and EELS study of the initial oxidation of polycrystalline chromium," *Surface Science*, vol. 182, no. 1, pp. 41–55, 1987.

[102] L. H. Gaabour, "Influence of silica nanoparticles incorporated with chitosan/polyacrylamide polymer nanocomposites," *Journal of Materials Research and Technology*, vol. 8, no. 2, pp. 2157–2163, 2019.

[103] R. C. Williams and R. C. Backus, "The electron-micrographic structure of shadow-cast films and surfaces," *Journal of Applied Physics*, vol. 20, no. 1, pp. 98–106, 1949.

[104] P. B. Weaver and C., "The adhesion of evaporated metal films on glass," *Proceedings of the Royal Society of London. Series A, Mathematical and Physical Sciences*, vol. 261, no. 1307, pp. 516–531, 1961.

[105] P. Benjamin, C. Weaver, and N. F. Mott, "Measurement of adhesion of thin films," *Proceedings of the Royal Society of London. Series A. Mathematical and Physical Sciences*, vol. 254, no. 1277, pp. 163–176, 1960.

[106] P. H. Holloway, "Gold/chromium metallizations for electronic devices," *Gold Bulletin*, vol. 12, no. 3, pp. 99–106, 1979.

[107] S. C. Jain, A. H. Harker, and R. A. Cowley, "Misfit strain and misfit dislocations in lattice mismatched epitaxial layers and other systems," *Philosophical Magazine A*, vol. 75, no. 6, pp. 1461–1515, 1997.

[108] A. Chithambararaj, N. S. Sanjini, S. Velmathi, and A. C. Bose, "Preparation of h-MoO_3 and α-MoO_3 nanocrystals: comparative study on photocatalytic degradation of methylene blue under visible light irradiation," *Phys Chem Chem Phys*, vol. 15, no. 35, pp. 14761–9, 2013.

[109] K. Dewangan, N. N. Sinha, P. K. Sharma, A. C. Pandey, N. Munichandraiah, and N. S. Gajbhiye, "Synthesis and characterization of single-crystalline α-MoO_3 nanofibers for enhanced Li-ion intercalation applications," *CrystEngComm*, vol. 13, no. 3, pp. 927–933, 2011.

[110] R. K. Sharma and G. B. Reddy, "Synthesis and characterization of α-MoO_3 microspheres packed with nanoflakes," *Journal of Physics D: Applied Physics*, vol. 47, no. 6, 2014.

[111] S. Guimond, D. Göbke, J. M. Sturm, Y. Romanyshyn, H. Kuhlenbeck, M. Cavalleri, and H. J. Freund, "Well-ordered molybdenum oxide layers on Au(111): Preparation and properties," *The Journal of Physical Chemistry C*, vol. 117, no. 17, pp. 8746–8757, 2013.

[112] A. Michailovski, J.-D. Grunwaldt, A. Baiker, R. Kiebach, W. Bensch, and G. R. Patzke, "Studying the solvothermal formation of MoO_3 fibers by complementary in situ EXAFS/EDXRD techniques," *Angewandte Chemie International Edition*, vol. 44, no. 35, pp. 5643–5647, 2005.

[113] G. R. Patzke, F. Krumeich, and R. Nesper, "Oxidic nanotubes and nanorods - anisotropic modules for a future nanotechnology," *Angewandte Chemie-International Edition*, vol. 41, no. 14, pp. 2446–2461, 2002.

[114] Z. Peng, *Nanofibers- Production, Properties and Functional Applications "Preparation and Characterization and Reducing Properties of MoO_3 Nano-Fibers"*. IntechOpen, 2011.

[115] L. Jiwen, "Nano MoO_3 phase structural evolution during hydrothermal synthesis and its electrochemical properties," *International Journal of Electrochemical Science*, pp. 2429–2440, 2017.

[116] D. F. Alexandru Grumezescu, *Nanostructures for Novel Therapy*. Elsevier, 2017.

[117] A. Michailovski and G. R. Patzke, "Hydrothermal synthesis of molybdenum oxide based materials: strategy and structural chemistry," *Chemistry*, vol. 12, no. 36, pp. 9122–34, 2006.

[118] N. Li, Y. M. Li, W. J. Li, S. D. Ji, and P. Jin, "One-step hydrothermal synthesis of TiO_2@ MoO_3 core-shell nanomaterial: Microstructure, growth mechanism, and improved photochromic property," *Journal of Physical Chemistry C*, vol. 120, no. 6, pp. 3341–3349, 2016.

[119] S. Subbarayudu, V. Madhavi, and S. Uthanna, "Growth of MoO_3 films by RF magnetron sputtering: Studies on the structural, optical, and electrochromic properties," *ISRN Condensed Matter Physics*, vol. 2013, pp. 1–9, 2013.

[120] A. Borgschulte, O. Sambalova, R. Delmelle, S. Jenatsch, R. Hany, and F. Nuesch, "Hydrogen reduction of molybdenum oxide at room temperature," *Sci Rep*, vol. 7, p. 40761, 2017.

[121] D. J. Goyal, C. Agashe, M. G. Takwale, and V. G. Bhide, "X-ray diffraction studies of sprayed SnO_2:Sb films," *Journal of Crystal Growth*, vol. 130, no. 3, pp. 567–570, 1993.

[122] C. F. Holder and R. E. Schaak, "Tutorial on powder X-ray diffraction for characterizing nanoscale materials," *ACS Nano*, vol. 13, no. 7, pp. 7359–7365, 2019.

[123] A. A. Ramadan, A. A. Abd El-Mongy, A. M. El-Shabiny, A. T. Mater, S. H. Mostafa, E. A. El-Sheheedy, and H. M. Hashem, "Addressing difficulties in using XRD intensity for structural study of thin films," *Crystal Research and Technology*, vol. 44, no. 1, pp. 111–116, 2009.

[124] M. Fantini and I. Torriani, "The compositional and structural properties of sprayed SnO_2:F thin films," *Thin Solid Films*, vol. 138, no. 2, pp. 255–265, 1986.

[125] C. Agashe, M. G. Takwale, V. G. Bhide, S. Mahamuni, and S. K. Kulkarni, "Effect of Sn incorporation on the growth mechanism of sprayed SnO_2 films," *Journal of Applied Physics*, vol. 70, no. 12, pp. 7382–7386, 1991.

[126] P. Y. Z. Vitalij K. Pecharsky, *Fundamentals of Powder Diffraction and Structural Characterization of Materials*, book Fundamentals of diffraction. Springer, Boston, MA, 2009.

[127] M. Inoue and I. Hirasawa, "The relationship between crystal morphology and XRD peak intensity on $CaSO_4 \cdot {}_2H_2O$," *Journal of Crystal Growth*, vol. 380, pp. 169–175, 2013.

[128] S. A. Speakman, "XRPD general applications, methodology, and introductions, basics of X-ray diffraction." MIT MRSEC - Materials Reseach Science and Engineering Center, Website, 2014. Online available under `http://prism.mit.edu/xray/documents/1%20Basics%20of%20X-Ray%20Powder%20Diffraction.pdf`; accessed August 2020.

[129] Y. Guo and J. Robertson, "Origin of the high work function and high conductivity of MoO_3," *Applied Physics Letters*, vol. 105, no. 22, 2014.

[130] K. Inzani, M. Nematollahi, F. Vullum-Bruer, T. Grande, T. W. Reenaas, and S. M. Selbach, "Electronic properties of reduced molybdenum oxides," *Phys Chem Chem Phys*, vol. 19, no. 13, pp. 9232–9245, 2017.

[131] R. Tokarz-Sobieraj, K. Hermann, M. Witko, A. Blume, G. Mestl, and R. Schlögl, "Properties of oxygen sites at the MoO_3(010) surface: density functional theory cluster studies and photoemission experiments," *Surface Science*, vol. 489, no. 1, pp. 107–125, 2001.

[132] "Atomic radius of the elements." Mathematica's ElementData Wolfram Research, Inc., Website, 2007. Online available under `https://periodictable.com/Properties/A/AtomicRadius.v.html`; accessed August 2020.

[133] G. Pacchioni, "Oxygen vacancy: the invisible agent on oxide surfaces," *Chemphyschem*, vol. 4, no. 10, pp. 1041–7, 2003.

[134] R. Schaub, E. Wahlström, A. Rønnau, E. Lægsgaard, I. Stensgaard, and F. Besenbacher, "Oxygen-mediated diffusion of oxygen vacancies on the TiO_2(110) surface," *Science*, vol. 299, no. 5605, p. 377, 2003.

[135] T. . F. Group, "Electron paramagnetic resonance (EPR)," *Comments on Inorganic Chemistry*, vol. 3, no. 5, pp. 230–238, 1984.

[136] A. Varlec, D. Arčon, S. D. Škapin, and M. Remškar, "Oxygen deficiency in MoO_3 polycrystalline nanowires and nanotubes," *Materials Chemistry and Physics*, vol. 170, pp. 154–161, 2016.

[137] E. Serwicka, "ESR evidence for structural rearrangements occurring upon MoO_3 reduction," *Journal of solid state chemistry*, vol. 51, pp. 300–306, 1984.

[138] K. C. Radha, R. V. Anavekar, J. L. Rao, and R. P. S. Chakradhar, "EPR and optical studies of Mo^{5+} ions in lithium molybdoborate glasses," *Applied Magnetic Resonance*, vol. 35, no. 1, pp. 1–13, 2008.

[139] S. S. Sunu, E. Prabhu, V. Jayaraman, K. I. Gnanasekar, T. K. Seshagiri, and T. Gnanasekaran, "Electrical conductivity and gas sensing properties of MoO_3," *Sensors and Actuators B: Chemical*, vol. 101, no. 1-2, pp. 161–174, 2004.

[140] N. S. Kopachevska, A. K. Melnyk, I. V. Bacherikova, V. A. Zazhigalov, and K. Wieczorek-Ciurowa, "Determination of molybdenum oxidation state on the mechanochemically treated MoO_3," *Himia, Fizika ta Tehnologia Poverhni*, vol. 6, no. 4, pp. 474–480, 2015.

[141] E. S. E. Haber, "Surface structure and reactivity of MoO_3," *Polyhedrton*, vol. 2, pp. 107–109, 1986.

[142] J. Baltrusaitis, B. Mendoza-Sanchez, V. Fernandez, R. Veenstra, N. Dukstiene, A. Roberts, and N. Fairley, "Generalized molybdenum oxide surface chemical state XPS determination via informed amorphous sample model," *Applied Surface Science*, vol. 326, pp. 151–161, 2015.

[143] Y. Zhen, J. Wang, F. Fu, W. Fu, and Y. Liang, "The novel Z-scheme ternary-component Ag/AgI/α-MoO_3 catalyst with excellent visible-light photocatalytic oxidative desulfurization performance for model fuel," *Nanomaterials (Basel)*, vol. 9, no. 7, 2019.

[144] J.-C. Dupin, D. Gonbeau, P. Vinatier, and A. Levasseur, "Systematic XPS studies of metal oxides, hydroxides and peroxides," *Physical Chemistry Chemical Physics*, vol. 2, no. 6, pp. 1319–1324, 2000.

[145] T. G. G. Maffeis, M. W. Penny, A. Castaing, O. J. Guy, and S. P. Wilks, "XPS investigation of vacuum annealed vertically aligned ultralong ZnO nanowires," *Surface Science*, vol. 606, no. 1-2, pp. 99–103, 2012.

[146] "Nitrogen." Thermofischer Scientific, Website, 2013. Online available under `https://xpssimplified.com/elements/nitrogen.php`; accessed September 2020).

[147] G. A. N. William E. Vargas, "Applicability conditions of the Kubelka-Munk theory," *Applied optics*, vol. 36, no. 22, 1997.

[148] L. Yang and B. Kruse, "Revised Kubelka-Munk theory. I. theory and application," *Journal of the Optical Society of America A*, vol. 21, no. 10, pp. 1933–1941, 2004.

[149] F. M. Paul Kubelka, "An article on optics of paint layers," *Zeitschrift fur technische Physik*, vol. 12, pp. 593–601, 1931.

[150] J. A. N. T. Soares, *Practical Materials Characterization*, book Introduction to Optical Characterization of Materials, pp. 43–92. Springer, New York, NY, 2014.

[151] B. M. Weckhuysen and R. A. Schoonheydt, "Recent progress in diffuse reflectance spectroscopy of supported metal oxide catalysts," *Catalysis Today*, vol. 49, no. 4, pp. 441–451, 1999.

[152] B. S. F. Jahan, M.H. Islam, "Band gap and refractive index determination of Mo-black coatings using several techniques," *Solar Energy Materials and Solar Cells*, pp. 283–293, 1995.

[153] D. L. Dexter, *Theory of the Optical Properties of Imperfections in Nonmetals*, pp. 353–411. Solid State Physics, Academic Press, 1958.

[154] M. R. Tubbs, "MoO_3 layers – optical properties, colour centres, and holographic recording," *physica status solidi (a)*, vol. 21, no. 1, pp. 253–260, 1974.

[155] J. Singh, *Optical Properties of Condensed Matter and Applications*. John Wiley & Sons Ltd,, 2006.

[156] M. Nowak, B. Kauch, and P. Szperlich, "Determination of energy band gap of nanocrystalline sbsi using diffuse reflectance spectroscopy," *Rev Sci Instrum*, vol. 80, no. 4, p. 046107, 2009.

[157] K. Li and D. Xue, "Estimation of electronegativity values of elements in different valence states," *The Journal of Physical Chemistry A*, vol. 110, no. 39, pp. 11332–11337, 2006.

[158] J. Meyer, S. Hamwi, M. Kröger, W. Kowalsky, T. Riedl, and A. Kahn, "Transition metal oxides for organic electronics: Energetics, device physics and applications," *Advanced Materials*, vol. 24, no. 40, pp. 5408–5427, 2012.

[159] G. Campet, J. Portier, and M. A. Subramanian, "Electronegativity versus Fermi energy in oxides: the role of formal oxidation state," *Materials Letters*, vol. 58, no. 3-4, pp. 437–438, 2004.

[160] F.-C. Chiu, "A review on conduction mechanisms in dielectric films," *Advances in Materials Science and Engineering*, vol. 2014, pp. 1–18, 2014.

[161] K. D. Schierbaum, "Engineering of oxide surfaces and metal/oxide interfaces for chemical sensors - recent trends," *Sensors and Actuators B-Chemical*, vol. 24, no. 1-3, pp. 239–247, 1995.

[162] W. R. Wilcox and T. J. LaChapelle, "Mechanism of gold diffusion into silicon," *Journal of Applied Physics*, vol. 35, no. 1, pp. 240–246, 1964.

[163] U. Gösele, "Fast diffusion in semiconductor." Website, 1988. Online available under `https://www.tf.uni-kiel.de/matwis/amat/def_ge/artikel/facsimil/fast_dif.html`; accessed August 2020).

[164] A. Vezzoli, R. J. Brooke, N. Ferri, S. J. Higgins, W. Schwarzacher, and R. J. Nichols, "Single-molecule transport at a rectifying GaAs contact," *Nano Lett*, vol. 17, no. 2, pp. 1109–1115, 2017.

[165] "Coefficients of linear thermal expansion." Engineering ToolBox, Website, 2003. Online available under `https://www.engineeringtoolbox.com/linear-expansion-coefficients-d_95.html`; accessed August 2020.

[166] H. Negishi, S. Negishi, Y. Kuroiwa, N. Sato, and S. Aoyagi, "Anisotropic thermal expansion of layered MoO_3 crystals," *Physical Review B*, vol. 69, no. 6, p. 064111, 2004.

[167] A. Way, J. Luke, A. D. Evans, Z. Li, J.-S. Kim, J. R. Durrant, H. K. Hin Lee, and W. C. Tsoi, "Fluorine doped tin oxide as an alternative of indium tin oxide for bottom electrode of semi-transparent organic photovoltaic devices," *AIP Advances*, vol. 9, no. 8, p. 085220, 2019.

[168] C. Clausen, G. Skands, C. Bertelsen, and W. Svendsen, "Coplanar electrode layout optimized for increased sensitivity for electrical impedance spectroscopy," *Micromachines*, vol. 6, no. 1, pp. 110–120, 2014.

[169] M. J. Toohey, "Electrodes for nanodot-based gas sensors," *Sensors and Actuators B: Chemical*, vol. 105, no. 2, pp. 232–250, 2005.

[170] C. Julien, A. Khelfa, O. M. Hussain, and G. A. Nazri, "Synthesis and characterization of flash-evaporated MoO_3 thin films," *Journal of Crystal Growth*, vol. 156, no. 3, pp. 235–244, 1995.

[171] V. Nirupama, K. R. Gunasekhar, B. Sreedhar, and S. Uthanna, "Effect of oxygen partial pressure on the structural and optical properties of DC reactive magnetron sputtered molybdenum oxide films," *Current Applied Physics*, vol. 10, no. 1, pp. 272–278, 2010.

[172] C. Julien, A. Khelfa, O. M. Hussain, and G. A. Nazri, "Synthesis and characterization of flash-evaporated MoO_3 thin films," *Journal of Crystal Growth*, vol. 156, no. 3, pp. 235–244, 1995.

[173] R. K. Gupta, K. Ghosh, and P. K. Kahol, "Temperature dependence of current-voltage characteristics of gold-strontium titanate thin film schottky diode," *Physica E: Low-dimensional Systems and Nanostructures*, vol. 42, no. 5, pp. 1509–1512, 2010.

[174] H. M. Chenari, H. Sedghi, M. Talebian, M. M. Golzan, and A. Hassanzadeh, "Poole-Frenkel conduction in Cu/nano-SnO_2/Cu arrangement," *Journal of Nanomaterials*, vol. 2011, pp. 1–4, 2011.

[175] D. A. Neamen, *Semiconductor physics and devices: basic principles*. New York, NY: McGraw-Hill, 2012.

[176] R. Aigner, A. Pointner, T. Preindl, P. Parzer, and M. Haller, "Embroidered resistive pressure sensors: A novel approach for textile interfaces," in *Proceedings of the 2020 CHI Conference on Human Factors in Computing Systems*, (New York, NY, USA), pp. 1–13, Association for Computing Machinery, 2020.

[177] R. Nigon, T. M. Raeder, and P. Muralt, "Characterization methodology for lead zirconate titanate thin films with interdigitated electrode structures," *Journal of Applied Physics*, vol. 121, no. 20, p. 204101, 2017.

[178] I. G. Austin and N. F. Mott, "Polarons in crystalline and non-crystalline materials," *Advances in Physics*, vol. 18, no. 71, pp. 41–102, 1969.

[179] J. R. Yeargan and H. L. Taylor, "The Poole-Frenkel effect with compensation present," *Journal of Applied Physics*, vol. 39, no. 12, pp. 5600–5604, 1968.

[180] S. K. Deb, "Physical properties of a transition metal oxide - optical and photoelectric properties of single crystal and thin film molybdenum trioxide," *Proceedings of the Royal Society of London Series a-Mathematical and Physical Sciences*, vol. 304, no. 1477, pp. 211–, 1968.

[181] A. I. Ayesh, "Metal/metal-oxide nanoclusters for gas sensor applications," *Journal of Nanomaterials*, vol. 2016, pp. 1–17, 2016.

[182] L. Lin, D. Liu, Q. Chen, H. Zhou, and J. Wu, "A vertical tip-tip contact silicon nanowire array for gas sensing," *Nanoscale*, vol. 8, no. 41, pp. 17757–17764, 2016.

[183] L. Khandare, S. S. Terdale, and D. J. Late, "Ultra-fast α-MoO_3 nanorod-based humidity sensor," *Advanced Device Materials*, vol. 2, no. 2, pp. 15–22, 2016.

[184] N. Barsan and U. Weimar, "Conduction model of metal oxide gas sensors," *Journal of Electroceramics*, vol. 7, no. 3, pp. 143–167, 2001.

[185] C. Xu, J. Tamaki, N. Miura, and N. Yamazoe, "Grain size effects on gas sensitivity of porous SnO_2-based elements," *Sensors and Actuators B: Chemical*, vol. 3, no. 2, pp. 147–155, 1991.

[186] Y. F. Sun, S. B. Liu, F. L. Meng, J. Y. Liu, Z. Jin, L. T. Kong, and J. H. Liu, "Metal oxide nanostructures and their gas sensing properties: a review," *Sensors (Basel)*, vol. 12, no. 3, pp. 2610–31, 2012.

[187] S. P. Lee, "Electrodes for semiconductor gas sensors," *Sensors (Basel)*, vol. 17, no. 4, 2017.

[188] N. Barsan, D. Koziej, and U. Weimar, "Metal oxide-based gas sensor research: How to?," *Sensors and Actuators B: Chemical*, vol. 121, no. 1, pp. 18–35, 2007.

[189] J. Meyer, S. Hamwi, M. Kröger, W. Kowalsky, T. Riedl, and A. Kahn, "Transition metal oxides for organic electronics: Energetics, device physics and applications," *Advanced Materials*, vol. 24, no. 40, pp. 5408–5427, 2012.

[190] I. Irfan, A. J. Turinske, Z. Bao, and Y. Gao, "Work function recovery of air exposed molybdenum oxide thin films," *Applied Physics Letters*, vol. 101, no. 9, p. 093305, 2012.

[191] T. Nandy, J. Coutu, R. A., and C. Ababei, "Carbon monoxide sensing technologies for next-generation cyber-physical systems," *Sensors (Basel)*, vol. 18, no. 10, 2018.

[192] H. A. Tahini, X. Tan, S. N. Lou, J. Scott, R. Amal, Y. H. Ng, and S. C. Smith, "Mobile polaronic states in α-MoO_3: An ab initio investigation of the role of oxygen vacancies and alkali ions," *ACS Appl Mater Interfaces*, vol. 8, no. 17, pp. 10911–7, 2016.

[193] M. Rellan-Pineiro and N. Lopez, "One oxygen vacancy, two charge states: Characterization of reduced α-MoO_3(010) through theoretical methods," *J Phys Chem Lett*, vol. 9, no. 10, pp. 2568–2573, 2018.

[194] H. M. Martínez, J. Torres, M. E. Rodríguez-García, and L. D. López Carreño, "Gas sensing properties of nanostructured MoO_3 thin films prepared by spray pyrolysis," *Physica B: Condensed Matter*, vol. 407, no. 16, pp. 3199–3202, 2012.

[195] E. Comini, G. Faglia, G. Sberveglieri, C. Cantalini, M. Passacantando, S. Santucci, Y. Li, W. Wlodarski, and W. Qu, "Carbon monoxide response of molybdenum oxide thin films deposited by different techniques," *Sensors and Actuators B: Chemical*, vol. 68, no. 1, pp. 168–174, 2000.

[196] K. Ghosh and C. Y. Yue, "Development of 3D MoO_3/graphene aerogel and sandwich-type polyaniline decorated porous MnO_2-graphene hybrid film based high performance all-solid-state asymmetric supercapacitors," *Electrochimica Acta*, vol. 276, pp. 47–63, 2018.

[197] H. Wang, D. Tran, J. Qian, F. Ding, and D. Losic, "MoS_2/graphene composites as promising materials for energy storage and conversion applications," *Advanced Materials Interfaces*, vol. 6, no. 20, p. 1900915, 2019.

[198] H. Zhao, L. Liu, R. Vellacheri, and Y. Lei, "Recent advances in designing and fabricating self-supported nanoelectrodes for supercapacitors," *Adv Sci (Weinh)*, vol. 4, no. 10, p. 1700188, 2017.

[199] N. G. Prakash, M. Dhananjaya, A. L. Narayana, D. P. M. D. Shaik, P. Rosaiah, and O. M. Hussain, "High performance one dimensional α-MoO_3 nanorods for supercapacitor applications," *Ceramics International*, vol. 44, no. 8, pp. 9967–9975, 2018.

[200] V. Augustyn, P. Simon, and B. Dunn, "Pseudocapacitive oxide materials for high-rate electrochemical energy storage," *Energy & Environmental Science*, vol. 7, no. 5, pp. 1597–1614, 2014.

[201] S. Q. Wang, X. Cai, Y. Song, X. Q. Sun, and X. X. Liu, "VOx@ MoO_3 nanorod composite for high-performance supercapacitors," *Advanced Functional Materials*, vol. 28, no. 37, 2018.

[202] S. Sun, Y. Sun, J. Wen, B. Zhang, X. Liao, G. Yin, Z. Huang, and X. Pu, "MoO_{3-x}-deposited TiO_2 nanotubes for stable and high-capacitance supercapacitor electrodes," *RSC Advances*, vol. 8, no. 39, pp. 21823–21828, 2018.

[203] J. Ding, S. A. Abbas, C. Hanmandlu, L. Lin, C.-S. Lai, P.-C. Wang, L.-J. Li, C.-W. Chu, and C.-C. Chang, "Facile synthesis of carbon/ MoO_3 nanocomposites as stable battery anodes," *Journal of Power Sources*, vol. 348, pp. 270–280, 2017.

[204] A. Jain, R. Balasubramanian, and M. P. Srinivasan, "Hydrothermal conversion of biomass waste to activated carbon with high porosity: A review," *Chemical Engineering Journal*, vol. 283, pp. 789–805, 2016.

[205] J. Poerschmann, B. Weiner, R. Koehler, and F.-D. Kopinke, "Hydrothermal carbonization of glucose, fructose, and xylose – identification of organic products with medium molecular masses," *ACS Sustainable Chemistry & Engineering*, vol. 5, no. 8, pp. 6420–6428, 2017.

[206] C. He, C. Tang, C. Li, J. Yuan, K.-Q. Tran, Q.-V. Bach, R. Qiu, and Y. Yang, "Wet torrefaction of biomass for high quality solid fuel production: A review," *Renewable and Sustainable Energy Reviews*, vol. 91, pp. 259–271, 2018.

[207] X. Yang, H. Li, A.-Y. Lu, S. Min, Z. Idriss, M. N. Hedhili, K.-W. Huang, H. Idriss, and L.-J. Li, "Highly acid-durable carbon coated Co_3O_4 nanoarrays as efficient oxygen evolution electrocatalysts," *Nano Energy*, vol. 25, pp. 42–50, 2016.

[208] X. Yang, K. Xu, R. Zou, and J. Hu, "A hybrid electrode of Co_3O_4 @ PPy core/shell nanosheet arrays for high-performance supercapacitors," *Nano-Micro Letters*, vol. 8, no. 2, pp. 143–150, 2016.

[209] P. Si, S. Ding, X.-W. Lou, and D.-H. Kim, "An electrochemically formed three-dimensional structure of polypyrrole/graphene nanoplatelets for high-performance supercapacitors," *RSC Advances*, vol. 1, no. 7, pp. 1271–1278, 2011.

[210] S. Jiang, T. Shi, H. Long, Y. Sun, W. Zhou, and Z. Tang, "High-performance binder-free supercapacitor electrode by direct growth of cobalt-manganese composite oxide nansostructures on nickel foam," *Nanoscale Research Letters*, vol. 9, no. 1, p. 492, 2014.

[211] N. Shi, Q. Liu, X. He, G. Wang, N. Chen, J. Peng, and L. Ma, "Molecular structure and formation mechanism of hydrochar from hydrothermal carbonization of carbohydrates," *Energy & Fuels*, vol. 33, no. 10, pp. 9904–9915, 2019.

[212] R. Madhu, V. Veeramani, S.-M. Chen, A. Manikandan, A.-Y. Lo, and Y.-L. Chueh, "Honeycomb-like porous carbon-cobalt oxide nanocomposite for high-performance enzymeless glucose sensor and supercapacitor applications," *ACS Applied Materials & Interfaces*, vol. 7, no. 29, pp. 15812–15820, 2015.

[213] N. Raghavan, S. Thangavel, and G. Venugopal, "Enhanced photocatalytic degradation of methylene blue by reduced graphene-oxide/titanium dioxide/zinc oxide ternary nanocomposites," *Materials Science in Semiconductor Processing*, vol. 30, pp. 321–329, 2015.

[214] X. Leng, S. Wei, Z. Jiang, J. Lian, G. Wang, and Q. Jiang, "Carbon-encapsulated Co_3O_4 nanoparticles as anode materials with super lithium storage performance," *Scientific Reports*, vol. 5, no. 1, p. 16629, 2015.

[215] I. de Castro Silva, A. C. Reinaldo, F. A. Sigoli, and I. O. Mazali, "Raman spectroscopy-in situ characterization of reversibly intercalated oxygen vacancies in α-MoO_3," *RSC Advances*, vol. 10, no. 31, pp. 18512–18518, 2020.

[216] D. Geng, S. Yang, Y. Zhang, J. Yang, J. Liu, R. Li, T.-K. Sham, X. Sun, S. Ye, and S. Knights, "Nitrogen doping effects on the structure of graphene," *Applied Surface Science*, vol. 257, no. 21, pp. 9193–9198, 2011.

[217] B. K. Kim, S. Sy, A. Yu, and J. Zhang, *Handbook of Clean Energy Systems*, book section Electrochemical Supercapacitors for Energy Storage and Conversion, pp. 1–25. John Wiley and Sons, Ltd, 2015.

[218] M. Vangari, T. Pryor, and L. Jiang, "Supercapacitors: Review of materials and fabrication methods," *Journal of Energy Engineering*, vol. 139, no. 2, pp. 72–79, 2013.

[219] Y. Yang, H. Fei, G. Ruan, C. Xiang, and J. M. Tour, "Edge-oriented MoS_2 nanoporous films as flexible electrodes for hydrogen evolution reactions and supercapacitor devices," *Advanced Materials*, vol. 26, no. 48, pp. 8163–8168, 2014.

[220] D. Murugesan, S. Prakash, N. Ponpandian, P. Manisankar, and C. Viswanathan, "Two dimensional α-MoO_3 nanosheets decorated carbon cloth electrodes for high-performance supercapacitors," *Colloids and Surfaces A: Physicochemical and Engineering Aspects*, vol. 569, pp. 137–144, 2019.

[221] B. Mendoza-Sánchez, T. Brousse, C. Ramirez-Castro, V. Nicolosi, and P. S. Grant, "An investigation of nanostructured thin film α-MoO_3 based supercapacitor electrodes in an aqueous electrolyte," *Electrochimica Acta*, vol. 91, pp. 253–260, 2013.

[222] C. Ray and T. Pal, "Recent advances of metal-metal oxide nanocomposites and their tailored nanostructures in numerous catalytic applications," *Journal of Materials Chemistry A*, vol. 5, no. 20, pp. 9465–9487, 2017.

[223] F. Haque, T. Daeneke, K. Kalantar-zadeh, and J. Z. Ou, "Two-dimensional transition metal oxide and chalcogenide-based photocatalysts," *Nano-Micro Letters*, vol. 10, no. 2, 2017.

[224] J. Werner, J. Geissbuhler, A. Dabirian, S. Nicolay, M. Morales-Masis, S. D. Wolf, B. Niesen, and C. Ballif, "Parasitic absorption reduction in metal oxide-based transparent electrodes: Application in perovskite solar cells," *ACS Appl Mater Interfaces*, vol. 8, no. 27, pp. 17260–7, 2016.

[225] Y. Liu, Z. Hong, Q. Chen, W. Chang, H. Zhou, T.-B. Song, E. Young, Y. Yang, J. You, G. Li, and Y. Yang, "Integrated perovskite/bulk-heterojunction toward efficient solar cells," *Nano Letters*, vol. 15, no. 1, pp. 662–668, 2015.

[226] G. DeLuca, A. N. Jumabekov, Y. Hu, A. N. Simonov, J. Lu, B. Tan, G. W. P. Adhyaksa, E. C. Garnett, E. Reichmanis, A. S. R. Chesman, and U. Bach, "Transparent quasi-interdigitated electrodes for semitransparent perovskite back-contact solar cells," *ACS Applied Energy Materials*, vol. 1, no. 9, pp. 4473–4478, 2018.

Acknowledgment

I would like to start my acknowledgment with what I believe, " We raise in degrees whom we will, but over every possessor of knowledge is one more knowing".

I would like to thank the ministry of higher education and scientific research, General administration of missions, Egypt. As well, German academic exchange service (DAAD) for funding my research in the frame of " German Egyptian research long-term scholarship".

I'm grateful and highly appreciated to my supervisor Prof. Schmidt-Mende for his kind acceptance, patience, time and support to be able to conduct my PhD in his high prestigious research group. I wish to express my thanks and appreciation to Dr. Klaus Boldt for great always support, time, patient, and trust on me, really appreciated gained so much knowledge from you specially during writing first published manuscript under your supervision. Moreover, I am thankful to our colaaborator in India Dr. R. Ananthakumar, Dr. Balasubramaniam Saravanakumar and Ms. Ankita Mohanty for the valuable intensive discussion, learning and knowledge, I have gained from them. I am thankful to Prof. Drescher for the fast response to be able to utilize and operate my measurement proposal in his laboratories with the great support from Dr. Mykhailo Azarkh, who was introducing me to the EPR laboratory, precise explanation and giving me the feeling as we are one family and one group from day one in a very perfect professional way. Dr. Marina Krumova, Dr. Muhammed Sultan and Dr. Zongkun Chen for their real support, knowledge and discussions.

I sincerely acknowledge the great support and help by Mr. Hamidreza Riazi-Nejad, Dr. Ka Kan Wang, Mr. Louis Kukk, Ing. Simon Haus, Ing. Ekkehard Moser, Ing. Michael Weiland, Ing. Bruno Erne and Mr. Marcus Schwamberger for the supporting and excellent harmony teamwork to build the home-made workstation for my study. I would like to thank and express my great appreciation to Dr. Heinrich Hohl (Isartext GbR) for his great effort to revise and discuss my thesis work. Additionally, I would like to thank my current group members; Stefan Schupp, Carola Ebenhoch, Emilia Schütz, Dr. Stefan Kraner, Tobias Seewald, Timo Raap and Dr. Wei Wang for the kind support in thesis revision and Latex maintaining.

In addition to all other group members, I have met: Dr.Julian Kalb, Dr. Philipp Ehrenreich, Dr. Eugen Zimmermann, Dr. Susanne Birkhold, Dr. Yuyi Feng, Dr. Hau Ho, Dr. Azhar Fakhar Uddin, Sara Sand, Frank Strössner, Michael Seybold, Jeldrik Huster, Sebastian Vollmer, Rafael Glatthaar, Malak Amjad Hashim Sharif, Denisha Gounden, Samina Qamar, Kalsoom Fatima and Irfan Haider as well India working group of Dr. Ananthakumar, Arun, Nilima, Sahusarbani, Oshen and Nibideta. I would also thank the support by Matthias Hagner, particle analysis center, the international office and the welcome center. I would like to thank all my friends in the university of Konstanz Dr. Rola Ali AlSeidi, Christiane Harmsen, Dr. Martin Fleck, Dr. Sabina Haus, Doaa Al-Saafin, Mohammed Alhissi, Ehab Ramadan, Abdulaah Alzuabi, and all IRTG members.

Great thanks to my supervisors and professors in Solid state physics department, Physics deviation at National Research Centers (NRC), Egypt, Prof. Aziza Abu-El-Soad, Prof. Samia Gad,

Prof. Mostafa Boshta, Dr. Mohamed H. Sayed. I'm highly thankful to my supervisors and professors in physics department, Ain Shams University in Cairo, Prof M. M. El-Nahass, Prof. Gamal M Youssef, and Prof.M.Hassan Talaat.

Finally, I would like to thank my family, my husband, my supporting daughter (Khadeja) and my parents, my sisters, my brother, and all my friends for always holding me up and nice worm feelings, they gave me. I would like to finish my acknowledgment to say "Thank you for all support, believe and trust on me and at the end it is for you, papa"